Max Planck Institute for Solid State Research

Stuttgart Center for Electron Microscopy

Recovering Low Spatial Frequency Phase Information by Electron Holography: Challenges, Solutions and Application to Materials Science

Approved dissertation to obtain the academic degree of Dr. rer. nat

Technische Universität Darmstadt

by

Cigdem OZSOY KESKINBORA

Darmstadt, 2016 - D17

Max Planck Institut für Festkörperforschung

“Recovering Low Spatial Frequency Phase Information by Electron Holography: Challenges, Solutions and Application to Materials Science”

zur Erlangung des akademischen Grades eines Dr. rer. nat

vom Fachbereich Material- und Geowissenschaften

der Technischen Universität Darmstadt

genehmigte Dissertation,

vorgelegt von

Cigdem OZSOY KESKINBORA, M.Sc.
aus Eskisehir, Türkei

Tag der mündlichen Prüfung: 14 Dezember 2015

1. Referent: Prof. Dr. Peter van Aken
2. Referent: Prof. Dr. Hans-Joachim Kleebe

Tag der Einreichung: 3. November 2015

Tag der Prüfung: 14. Dezember 2015

Darmstadt, 2016 - D17

„to my dad

biricik babam

Sedat Sami Ozsoy'a"

Abstract

Bi_2Se_3 is a narrow band gap semiconductor, which has the peculiarity to host a single degenerate surface state consisting of a Dirac cone.[1] Since the discovery of its surface state using angle resolved photoemission spectroscopy (ARPES), Bi_2Se_3 has been considered as a simple model system for topological insulators (TIs). As expected for TIs, the Bi_2Se_3 surface state stays robust against adsorption of adatoms even after exposure to air. However, as a semiconductor, atomic or molecular adsorption creates an electrical potential, which induces bending of energy bands at the surface. ARPES measurements showed that exposing Bi_2Se_3 to air results in the appearance of new parabolic bands at the surface. These states are imputed to the presence of a two dimensional electron gas (2DEG), resulting from downward bending of the conduction band at the (110) surface.[2] However, ARPES experiments are carried out in reciprocal state, and so cannot "see" the 2DEG whereas it can be directly observed by electron holography in a transmission electron microscope (TEM).

Holography - originally developed for correcting spherical aberration in transmission electron microscopes[3] - is now used in a wide range of disciplines that involve the propagation of waves, including light optics,[4] electron microscopy,[5] acoustics[6] and seismology.[7] In electron microscopy, the two primary modes of holography are Gabor's original in-line setup and an off-axis approach that was developed subsequently. Electron holography is a powerful technique for characterizing electrostatic potentials,[8] charge order, electric[9] and magnetic[10] fields, strain distributions,[11,12] and semiconductor dopant distributions[13] with nm spatial resolution. One of the main electron holography methods, in-line electron holography, suffers from inefficient low spatial frequency recovery but has the advantage of high phase sensitivity at high spatial frequencies. In contrast, off-axis electron holography can cover the low spatial frequencies but cannot achieve currently the performance of in-line holography at high spatial frequencies. These two techniques are highly complementary, offering superior phase sensitivity at high and low spatial resolution, respectively. All previous investigations have focused on improving each method individually.

This dissertation summarizes two alternative approaches. The first approach focuses on the in-line electron holography method and shows the first examples of how gradient-flipping enhances the low spatial frequency recovery of the existing flux preserving non-linear wave reconstruction algorithm. The second approach, called hybrid electron holography, shows how the two methods can be combined in a synergetic fashion to provide phase information with excellent sensitivity across all spatial frequencies, low noise and an efficient use of electron dose. These principles are expected to be widely applicable also to holography in light optics, X-ray optics, acoustics, ultra-sound, terahertz imaging, etc.

High spatial resolution and high phase sensitivity are crucial for investigating low dimensional materials and challenging when the aim is full quantifiability. Therefore, gold nanoparticles and some preliminary result from Bi_2Se_3 are presented as an example, showcasing the suitability of hybrid electron holography for addressing such questions.

Zusammenfassung

Bi_2Se_3, ein Halbleiter mit kleiner Bandlücke, besitzt die Besonderheit, dass an seiner Oberfläche ein einzelner entarteter Elektronenzustand in Form eines Dirac-Kegels auftritt. Seit der Entdeckung dieses Zustandes mittels winkelaufgelöster Photoemissions-Spektrosopie (ARPES) gilt Bi_2Se_3 als einfaches Modellsystem eines topologischen Isolators. Der Oberflächenzustand wird nicht durch Adsorption von Gasen, z.B. an Luft, zerstört, was typisch für topologische Isolatoren ist. Wegen seiner Halbleitereigenschaft bildet sich durch Gasadsorption allerdings ein elektrisches Potential welches zur Bandverbiegung an der Oberfläche führt. ARPES-Messungen haben gezeigt, dass an Luft neue parabolische Bänder in Oberflächennähe auftreten. Diese Bänder werden einem 2-dimensionalen Elektronengas zugeschrieben welches entsteht, indem das Leitungsband an der (110)-Oberfläche nach unten gebogen wird. Das Problem von ARPES-Messungen ist, dass sie den reziproken Raum vermessen, d.h. ein 2-dimensionales Elektronengas kann so nicht direkt sichtbar gemacht werden. Dies ist mit der Elektronenholografie im Transmissions-Elektronenmikroskop (TEM) möglich.

Holografie, ursprünglich entwickelt um den Öffnungsfehler von Linsen im TEM zu korrigieren, wird inzwischen in vielen Bereichen angewandt in denen die Ausbreitung von Wellen eine Rolle spielt. Dazu gehören die Lichtoptik, die Elektronenmikroskopie, die Akustik und Seismologie. Im Bereich der Elektronenmikroskopie werden insbesondere die ursprünglich von Gabor entwickelte in-line-Holografie sowie die später entwickelte off-axis-Holografie angewandt. Die Elektronenholografie ist ein mächtiges Werkzeug für die Charakterisierung von elektrischen Potentialen, Ladungsordnung, Magnetfeldern, elastische Spannungen und Dotierverteilungen in Halbleitern, alles mit einer Ortsauflösung im Nanometerbereich. Die in-line-Holografie kann zwar niedrige Raumfrequenzen nur unzureichend detektieren, hat aber den Vorteil einer hohen Phasenempfindlichkeit bei hohen Raumfrequenzen. Im Gegensatz dazu kann die off-axis-Holografie niedrige Raumfrequenzen gut auflösen, ist aber bei hohen Raumfrequenzen der in-line-Holografie unterlegen. Dies zeigt, dass die zwei Methoden komplementär sind und in ihrem Zusammenspiel in der Lage sind, sowohl bei niedrigen als auch bei hohen Frequenzen hohe

Phasenempfindlichkeit zu erreichen. Bisher wurden beide Methoden separat optimiert, nicht aber gemeinsam.

In der vorliegenden Dissertation werden beide Methoden vorgestellt. Zunächst wird gezeigt wie in der in-line-Holografie im flusserhaltenden, nichtlinearen Wellenrekonstruktionsalgorithmus die Rekonstruktion niedriger Raumfrequenzen mittels Gradienten-Umkehr (gradient-flipping) verbessert wird. Anschließend wird gezeigt wie durch Kombination beider Holografiemethoden die Phasenempfindlichkeit über den gesamten Raumfrequenzbereich bei geringem Signalrauschen und idealer Ausnutzung der Elektronendosis erreicht werden kann. Dies wird als *hybride Elektronenholografie* bezeichnet von welcher wir breite Anwendungsmöglichkeiten im Bereich der Lichtoptik, Röntgenoptik, Ultraschall- und Terahertz-Abbildung erwarten.

Für die Untersuchung niedrigdimensionaler Materialien sind hohe Ortsauflösung und hohe Phasenempfindlichkeit entscheidend, insbesondere wenn diese Untersuchungen quantitativen Charakter haben sollen. Dies wird am Beispiel von Gold-Nanopartikeln und ansatzweise an Bi_2Se_3-Proben gezeigt und stellt einen Nachweis der Anwendbarkeit der hybriden Elektronenholografie dar.

Acknowledgments

The present work was performed at the Stuttgart Center for Electron Microscopy (StEM) which is headed by Prof. Dr. Peter van Aken in Max Planck Institute for Solid State Research. This long journey which started in 2011, is coming to an end with great and also, some sad memories. I want to thank many people due to their contributions during this important time period of my life, which I will not forget.

I want to start with my dear husband Kahraman Keskinbora who shares my life with continued support and kindness. Despite his own PhD studies he always helped me, encourage me, at times of despair.

I always feel lucky to be able to carry out my PhD study at the Max Planck Institute. So, first of all I would like to express my appreciation to Prof. Dr. Peter A. van Aken for giving me this opportunity, great freedom and support during my whole research. His offer lead to the realization of a dream, to meet and work with amazing people and in an amazing project.

I would like to thank Prof. Dr. Joachim Hans Kleebe for his guidance and accepting me as a PhD student in the Technical University of Darmstadt, the place where my Germany adventure started.

Prof. Dr. Christoph T. Koch, my daily supervisor, who will always be an example scientist and person for me, cannot be thanked enough. Even after he moved from Max Planck Institute after half a year into my PhD, he continued to supervise, support and encourage me.

Sometimes, people have problems to use in house equipments. As an outsider in Julich, I was able to use the microscopes in Ernst Ruska Center. I would like to thank Prof. Dr. Rafal Dunin-Borkowski due to his generous and always enthusiastic support to my study. Also Dr. Chris Boothroyd, my tutor in Julich, who taught me how to use the microscope in Julich and also helped with the off-axis electron holography. I am always grateful to collaborate with them and learn from them. Futhermore, I want to thank Wouter Van den Broek and Robert Pennington, for fruitfull discussions and their valuable comments.

I want to thank whole StEM group as it was a privilege to work with them, but especially, to Birgit Bussmann for kindness and for preparing the Bi_2Se_3 sample, to Ute Salzberger and Marion Kelsch for their helps not only on sample preparation but also with my daily

problems, Kersten Hann and Peter Kopold for teaching me to use the microscopes and keeping them ready for. I want to thank Nahid Talebi and Wilfrid Sigle for their fruitful discussions. Also many thanks to Ekin Simsek Sanli and Eren Suyolcu as my successors in the StEM group ☺. Special thanks go to "mom" Vesna Srot as her last child for especially emotional support. Off course to Caroline Heer, a lovely lady she was and always is there for us.

I would like to thank Hadj Benia who is responsible for me to start working on Bi_2Se_3. Even though I couldn't finalize the task on Bi_2Se_3 (yet!!!:), the problem which I faced during this study carried my work into the next level. So, I am very appreciating.

I am also grateful to John Bonevich for offering free public use of the HolograFREE off-axis electron holography reconstruction software which was used during this study besides FPWR which is written by Christoph T. Koch.

I would like to thank whole the Turkish Mafia who always kept up the friendly atmosphere.

I would like to thank ESTEEM2 for funding.

I thank my parents-in-law Dilek, Serdar and my sister Elif Keskinbora, supports and encouragement during hard and good days.

I want to thank my family for their un-interrupted support throughout my educational life and life in general. Without their encouragement and input I wouldn't make it so far. I cannot thank enough to my mom Ayse Ozsoy who also graduates alongside me and my brother Cem for his support for me in our difficult times. Finally, I express my deepest gratitude to my dear late father Sedat Sami Ozsoy, whom I have lost last year and whom always believed in me, was proud of me and supported me.

Cigdem OZSOY KESKINBORA,

Stuttgart 2015

Table of Content

1. Introduction

General Context

Is the electron a particle or a wave? The basis of this question was another question "is light a wave or a particle?" At the end of the 1800's light was widely accepted to be a wave. It could be completely explained with Maxwell's equations.[14] In 1900 Max Planck proposed that light can carry discrete energy values and this led to Albert Einstein's photoelectric effect study in which light was defined as a discrete wave packet,[15] a photon.[16] Light behaves either as a particle or as a wave under different conditions. In 1924, Louis de Broglie took the concept to a new level by discussing the duality for any matter. If a photon can show both particle and wave properties, how about other particles such as electrons? According to de Broglie matter can be associated with a wave with $\lambda = h/p$, where λ is Broglie wave length, h is Planck's constant and p is the momentum of matter. D e Broglie hypothesis is valid for any matter, as well as for electrons. Electrons show both particle and wave behavior which forms the fundamental interactions used in electron microscopy. Methods such as diffraction, holography, and high resolution imaging rely on the wave-like properties of electrons. Energy loss and X-ray spectroscopy, as well as secondary effects such as secondary electron imaging, backscattering and are caused by the particle-like nature of the electron.

For the first time in 1931, Knoll and Ruska obtained images using electrons[17,18] with a microscope that did not suffer from diffraction limit (d) related to the wavelength of visible light[19], $d = {}^{\lambda}/_{2NA}$ where NA is the numerical aperture. At least that was their first idea. Ernst Ruska mentioned in his Nobel lecture that he was disappointed when he first heard about de Broglie's hypothesis because the wavelength would become again a limit for their microscope. He was satisfied when they realized that the electron wave has an ~5 orders of magnitude shorter wavelength than visible light.[20] Today, still electron microscopes are far away from being able to reach the diffraction limit due to the imperfections in the electromagnetic lenses or electron sources.

In 1948, Dennis Gabor introduced a method called holography[3] to improve the resolution in electron microscopes by correcting aberrations of the imaging system using

the electron wave function. The main idea behind holography is obtaining the wave function of the investigated sample by creating a phase difference with a reference wave. In Gabor's first experiment the reference wave and object wave were in the same optic axis (in-line setup). However, it was not practically applicable for electron microscopy. Then, this idea was followed by creating interferences using a reference wave that was aligned in a different axis than the object wave with the help of a charged wire called the biprism.[21] This second method, called off-axis electron holography, provided a straightforward and accurate reconstruction, despite the necessity of extra hardware. In 1972 Gerchberg and Saxton proposed an iterative computational algorithm that used several wave front intensities recorded in the image and diffraction plane.[22] In this method the incident beam was the reference beam itself. Nowadays, these two set-ups, in-line and off-axis electron holography, are at the center of phase retrieval studies.

Motivation

Once the wave function is obtained, it is not only possible to remove the aberrations, but also to access information on the electrical and magnetic properties of the sample. This is the reason, even though today transmission electron microscopes have the correctors for some higher order aberrations, electron holography is still a widely used method. It gives the opportunity to map electric[9] and magnetic[10] fields, electrostatic potential,[23] strain[11,12] or charge distributions[13] and other characteristic properties.

Bi_2Se_3 has been widely studied due to its thermoelectric behavior since 1958[24]. It became popular again with the discovery of its interesting surface state in 2009[1]. The surface state appears as a result of high spin orbit coupling which creates a Dirac cone in its band structure just at the surface. Beside this, it shows extra band bending that causes the formation of a 2 dimensional electron gas (2DEG) at the Bi_2Se_3 surface. Although ARPES measurements had proved the existence of a 2DEG in Bi_2Se_3,[2] the method gives reciprocal space information. Therefore, the distribution of these charges in real space is not known. Electron holography is a serious candidate to determine the distributions of the 2DEG in Bi_2Se_3. So the preliminary purpose of the PhD work was the mapping of the 2DEG in Bi_2Se_3 in real space using in-line electron holography, due to its high phase sensitivity. The results of 2 years of study showed that the strong phase properties of Bi_2Se_3 and the condensation

of artifacts at the surface, due to missing low spatial frequencies make quantification impossible. It is also known that the other electron holography method, off-axis electron holography, does not have enough phase sensitivity yet to measure the very weak phase changes due to the 2DEG.

Because of certain drawbacks of in-line and off-axis electron holography for determination of mapping the 2DEG of Bi_2Se_3, the direction of this study was steered towards the enhancement of electron holography methods. In this manner, the hybrid electron holography method which combines off-axis and in-line electron holography in a synergetic way, and the gradient-flipping assisted flux preserving in-line electron holography method were introduced into the scope of this thesis.

I would like to summarize first the in-line electron holography investigation on Bi_2Se_3, which was carried out with the flux preserving in-line wave reconstruction algorithm introduced by Koch[25,26] and point out the challenges. Then I will present the first electron holography results achieved by using flux preserving non-linear wave reconstruction improved by applying a gradient flipping method. Later, I will introduce the method that synergistically combines in-line and off-axis electron holography for superior phase resolution and sensitivity which is fully quantitative.

Organization of the Thesis

In this dissertation all chapters have an introduction that describes each project in detail, mainly based on the publications given above, so that, each chapter can be considered independently.

The 1st chapter is a general introduction that summarizes the key points on electron holography, such as electron-matter interaction, the physical background, and the two major electron holography methods with their comparison.

The second chapter focuses on in-line electron holography studies. In the first part of the chapter, the investigations that are done on Bi_2Se_3 to observe the 2DEG with the flux preserving nonlinear in-line electron holography algorithm and existing problems are

described. Then, improvements by the addition of gradient flipping to the flux preserving wave algorithm are discussed.

Chapter 3 introduces the hybrid electron holography method, which is a synergetic combination of off-axis and in-line electron holography for the first time.

Chapter 4 gives some examples of the applications and capabilities of hybrid electron holography for material science problems.

Chapters 3 and 4 are the based on the papers,

"Hybridization approach to in-line and off-axis (electron) holography for superior resolution and phase sensitivity" C. Ozsoy-Keskinbora, C. B. Boothroyd, R. E. Dunin-Borkowski, P. A. van Aken & C. T. Koch published in Scientific Reports in 2014,Vol 4, 07020 and

"Mapping the Electrostatic Potential of Au Nanoparticles via Hybrid Electron Holography" C. Ozsoy-Keskinbora, C. B. Boothroyd, R. E. Dunin-Borkowski, P. A. van Aken & C. T. Koch, which published in Ultramicroscopy in 2016 Vol 165, Pages 8-14, respectively.

Furthermore, second half of the Chapter 2 is based on another paper which is in preparation with named as

"Improved low frequency recovery, high-contrast imaging of phase objects by gradient-flipping assisted flux preserving wave reconstruction" coauthored as Cigdem Ozsoy-Keskinbora, Wouter Van den Broek, Amin Parvizi, Xiaoming Jiang, Chris Boothroyd, Rafal E. Dunin-Borkowski, Peter A. van Aken, Christoph T. Koch.

Furthermore, as a side project, another paper is published in *ACS Nano*, 2016, 10 (7), 6988-6994 and.named as "Wadge Dyakonov Waves and Dyakonov Plasmons in Topological Insulator Bi_2Se_3 Probed by Electron Beams". coauthored as Nahid Talebi, Cigdem Ozsoy-Keskinbora, Hadj Mohamed Benia, Christoph T. Koch, Peter A. van Aken.

The final chapter summarizes the whole thesis and its contribution to the literature, with future perspectives.

1.1. Electron Matter Interaction

An electron ($^{-}$e) is an elementary particle with a negative charge. Due to its small mass it must often also be treated as a wave. The electron was discovered by J.J. Thomson in a 1897 experiment which demonstrated the deflection of cathode rays under an electric field. [27] Because of its charge an electron can be scattered by electrostatic forces and by other charged particles. This allows the electron to be focused or directed with electromagnetic lenses and to be used for imaging or spectroscopy, to characterize the results of interactions of incident electrons and a sample. This interaction (or scattering) can either be inelastic, such as in absorption or emission, or it can be elastic where the kinetic energy is conserved. Before focusing on individual scattering events, all scattering events used in electron microscopy are summarized as in Fig. 1.1.

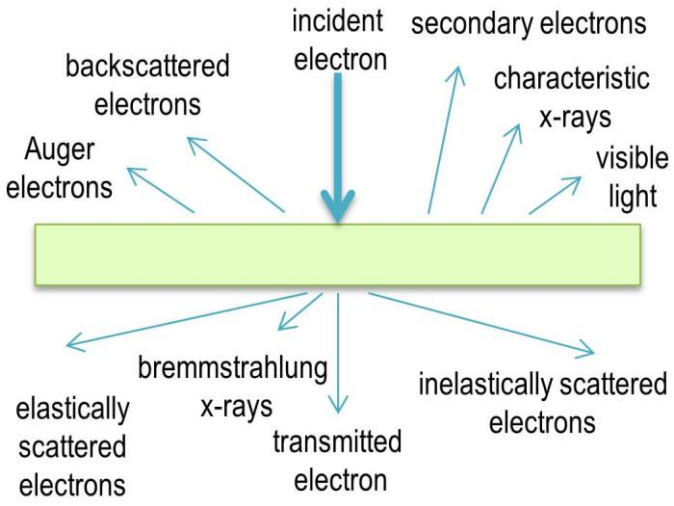

Figure 1. 1 Signals generated due to electron-specimen interactions[28].

1.1.1. Elastic and Inelastic Scattering

Elastic Scattering

The electrons with a kinetic energy E_k that encounter matter, scatter either without any energy exchange or transfer some of their energy to the specimen. They can be scattered by an isolated single atom or they can collectively scatter from an ensemble of atoms. In the case of a single isolated atom, the scattering happens as a result of Coulombic interactions between the incident electron and the electrostatic field of a nucleus or electron cloud. The scattering takes place with negligible energy transfer and it is called elastic scattering. When

an electron passes close enough to the nucleus of atom, it is drawn in by the nucleus. This event induces deflection of the electron at very high angles, it can even be backscattered. Many of the electrons travel through the specimen, as the interaction with a nucleus is limited by the fast-decaying electrostatic potential (obeying the inverse square law) of the nucleus which is also partially shielded by the core shell electrons. [29] (Fig. 1.2)

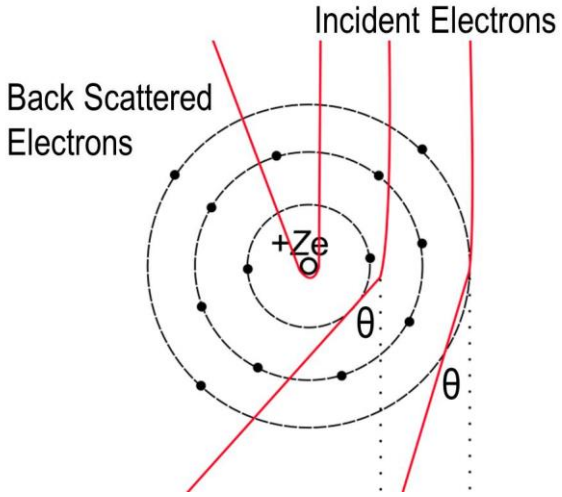

Figure 1. 2. Schematic of elastic scattering due to the interaction of an electron beam with an atom.

For Rutherford scattering, which neglects the effect of the scattering electrons, the probability p(θ) of an electron with incident energy E_0 being scattered though the angle θ is defined by.[30]

$$p(\theta) \propto \frac{1}{E_0^2 \sin^4\theta} \qquad \text{Eq. 1. 1}$$

As can be seen from the eq. 1.1 the probability of low angle scattering is higher than for high angles.

Inelastic Scattering

Another scattering event is inelastic scattering where detectable energy transfer occurs; the incident electron looses or gains energy. Again for the isolated atom case, when incident electrons interact with the nucleus and are decelerated by the Coulomb field, this causes continuous X-ray emission called Bremsstrahlung. Another type of interaction is when an inner shell electron is knocked out. Since the electrons are bond, this process needs a certain amount of energy[30] so the incident electron transfers part of its energy to the core-shell electron. This energy value is characteristic and is equal to the difference between the initial

and final stage of the core-shell electron, which was knocked out by the incident electron. In a later stage this excited electron can return to its ground state. During this process the excited electron loses its energy by emitting a characteristic X-ray, which is commonly used for spectroscopy. [28] Figure 1.3 summarizes this process for K and M shell electrons. With help of specific detectors, both X-rays and the incident electrons' energy loss can be detected *via* transmission electron microscopy. (See the details for X-ray spectroscopy [28] and electron energy loss spectroscopy[29]).

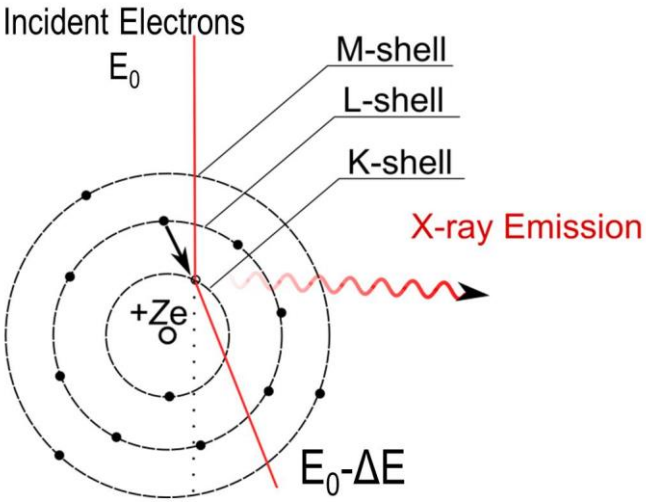

Figure 1. 3 Schematic of inelastic scattering due to the interaction of an electron beam with an atom.

Inner-shell interactions cover a small part of inelastic scattering phenomena. Auger electrons, secondary electrons, cathodoluminescence, etc. are all also results of inelastic scattering, but those signals do not commonly find practical applications in TEM (for details see[28]). The most common inelastic scattering phenomenon in TEM is generated by plasmons, which are collective oscillations of weakly bonded or free electrons.[29] Plasmon scattering has the highest scattering cross section of all inelastic scattering events.

Another relatively weak collective oscillations that causes inelastic scattering are phonons, where all the atoms in a crystal oscillate collectively as a result of energy transfer from an incident electron.

The scattering cross section and scattering angle determine the penetration length of the electron in the specimen, the mean free path (λ).

$$\lambda \approx \frac{Z}{\sigma N_A \rho} \qquad \text{Eq. 1. 2}$$

where N_A and ρ are Avogadro's number and density, respectively.[31]

1.1.2. Coherent and Incoherent Scattering

Categorization of scattering events as elastic or inelastic scattering is based on the particle behavior of the electron. The second way of classifying electron scattering is as coherent or incoherent scattering, which originate from the wave nature of electrons. With the developments in electron sources, especially the discovery of field emission guns, the temporal and especially the spatial coherence of the incident electrons have greatly improved. When the incident electron is scattered in the sample, and if the scattered electron still preserves a (constant) phase relation with its initial state, then this scattering event is categorized as coherent scattering. Different partial waves of the same electron constructively interfere with each other when phase maxima superimpose. If these maxima positions shift, the waves may cancel, i.e. interfere destructively. Therefore the total intensity can be constructed by adding the amplitudes of the scattered wavelets scattered from different locations (ψ_{r_j}) as in Eq. 1. 3 and 1.4.

$$\psi_{coh} = \sum_{r_j} \psi_{r_j} \qquad \text{Eq. 1. 3}$$

$$I_{coh} = \psi_{coh}\, \psi_{coh}^{*} = \left|\sum_{r_i} \psi_{r_j}\right|^2 \qquad \text{Eq. 1. 4}$$

ψ^* is the complex conjugate. However, in incoherent scattering the phase relation is broken. This destroys the destructive and constructive interference, which prevent the summation of the amplitudes of the scattered waves. This means the intensities must be individually summed[32] (Eq. 1.5).

$$I_{incoh} = \sum_{r_i} I_{r_j} = \sum_{r_i} \left|\psi_{r_j}\right|^2 \qquad \text{Eq. 1. 5}$$

Diffraction can be given as the most well-known example of coherent scattering in TEM.

1.2. Electron Holography

The wave-like properties of electrons, more specifically coherently scattered electrons form the basis of electron holography. When incident electrons pass though the specimen, the wavelength of the incident beam changes as a result of the interaction and at the end the incident wave (or the wave that pass through vacuum) and the object wave have

different phases.[33] The effect of the interaction on the phase is given by the following, [34] Eq. 1.6.

$$\phi(x) = C \int V(x,y)\, dz_E - \left(\frac{e}{\hbar}\right) \int B_\perp (x,y) dx dz \qquad \text{Eq. 1. 6}$$

where C_E is described by Eq.1.10, where E and E_0 are the kinetic and rest mass energies of the electron and λ is its wavelength.

$$C_E = \left(\frac{2\pi}{\lambda}\right) \left(\frac{E + E_0}{E\,(E+2E_0}\right) \qquad \text{Eq. 1. 7}$$

So the phase information gives information on the mean inner potential (V), magnetic field (B) and thickness (t) of the specimen.

Cowley summarizes different ways to create and measure this interference.[35] In this dissertation the two most common holography methods, in-line and off-axis electron holography, will be discussed with their advantages and disadvantages, and an alternative way, to solve the current problem with a combination of these two methods, will be described.

1.3. Off-Axis Electron Holography

As mentioned above, a positively charged wire, which is placed near the intermediate image plane (in most cases), is used in off-axis electron holography to produce an interference pattern between the object wave and a reference wave that comes from the vacuum. The main idea is to superimpose these two waves and to measure the phase difference[36]. The incident beam is defined as a plane wave.

$$\psi(\vec{r}, t) = A \exp(i(2\pi \vec{q}\, \vec{r} + \varphi - \omega t)) \qquad \text{Eq. 1. 8}$$

The interference of two waves (or the superposition of two waves) is the sum of these two waves ψ_1+ ψ_2. So that the intensity is

$$I(\vec{r}, t) := (\psi_1 + \psi_2)(\psi_1 + \psi_2)^* \qquad \text{Eq. 1. 9}$$

w $\vec{q}_c = \overrightarrow{q_1} = \overrightarrow{q_2}$;

$$I_{hol}(\vec{r}) = A_1^2 + A_2^2 + 2A_1 A_2 \cos(2\pi i q_c r + \Delta\varphi) \qquad \text{Eq. 1. 10}$$

Since the reference wave is the non-scattered electron, Eq. 1.7 can be simplified as

$$I_{hol}(\vec{r}) = 1 + A_O^2 + 2A_O \cos(2\pi i q_c r + \Delta\varphi) \qquad \text{Eq. 1. 11}$$

This contains the amplitudes and interference fringes that carry the phase information.[37]

The reconstruction of the hologram starts with the Fourier transform of the hologram.

$$\mathrm{FT}\{\mathrm{I_{hol}}(\vec{\mathrm{r}})\} = \begin{cases} \delta(\vec{\mathrm{q}}) + \mathrm{FT}\{1 + \mathrm{A}_0^2(\vec{\mathrm{r}})\} & \text{central band} \\ + \mu\mathrm{FT}\{\mathrm{A}_i(\vec{\mathrm{r}})\mathrm{e}^{\mathrm{i}\phi(\vec{\mathrm{r}})}\} \otimes \delta(\vec{\mathrm{q}} - \overrightarrow{\mathrm{q_c}}) & \text{sideband} + 1 \\ + \mu\mathrm{FT}\{\mathrm{A}_i(\vec{\mathrm{r}})\mathrm{e}^{\mathrm{i}\phi(\vec{\mathrm{r}})}\} \otimes \delta(\vec{\mathrm{q}} + \overrightarrow{\mathrm{q_c}}) & \text{sideband} - 1, \end{cases} \quad \text{Eq. 1. 12}$$

where $\boldsymbol{q}$ is the two-dimensional reciprocal space coordinate, $A(\boldsymbol{r})$ and $\phi(\boldsymbol{r})$ are the amplitude and phase of the object wavefunction and μ is the contrast of the holographic interference fringes.

The inverse Fourier transform of one of the side bands after applying a circular mask gives the complex wave function and the amplitude A is $\sqrt{Re^2 + Im^2}$ and the phase $\boldsymbol{\phi}$ is $tan^{-1}\left(\frac{Im}{Re}\right)$ of the complex image. The center band is the Fourier transform of the conventional image.[38]

1.4. In-line Electron Holography

In-line electron holography in the TEM, also known as focal series reconstruction, is similar to the scheme that was introduced by D. Gabor.[3] In Gabor's initial idea, a spherical wave was used for the reference wave. Fresnel fringes, which form as a result of the interference of the scattered and un-scattered electrons, can be used to reconstruct the phase information. In focal series reconstruction the interference patterns from several defocused images are used. The recorded image is a convolution of the object wave and the aberrations in the imaging system. So, if the effect of the imaging system is known, it is possible to back propagate the image wave and to obtain the object wave. Coherent wave propagation can be described in a straightforward way by Fresnel propagation. Algorithms based on the weak phase object approximation (WPOA),[39] the transport intensity equation (TIE),[40] the maximum likelihood (MAL)[41] principle, etc. are applied for the reconstruction. These methods can be classified in two categories, linear and non-linear imaging models, depending on whether the model considers the interference among the diffracted beams or not.[42] In the linear imaging approach only the interference between the transmitted beam and the diffracted beam is used to model the wave propagation, the paraboloid method[43] and a three dimensional Fourier filtering method (3D-FFM)[44] can be given as examples for

algorithms that use the linear imaging approximation. As an explanation of the linear imaging approximation, in WPOA the image exit wave is defined as $\psi_e(\vec{r}) = 1 + i\sigma t V_P(\vec{r})$, where V_P is the projected inner potential, σ is the interaction constant and t is sample thickness much less than 1.

Accordingly, the intensity of the image is introduced, as in Eq. 1.10, after the convolution of the exit wave function with the transfer function (T) of the microscope.

$$I(\vec{r}) \approx 1 + 2Re\{i\sigma t V_P(\vec{r}) \otimes T(\vec{r})\} + [i\sigma t V_P(\vec{r}) \otimes T(\vec{r})]^2 \qquad \text{Eq. 1. 13}$$

In this intensity definition, the quadratic term is neglected according to the weak scattering object, which leaves the term that carries the information derived from the diffracted beams interference in linear imaging theory.[45]

In many cases the diffracted electron has considerable intensity, which makes linear imaging not appropriate for such a specimen. This means that the interference between diffracted beams with each other is strong enough not to be neglected. For such cases, there should be another approach. The first example of the consideration of nonlinear contributions was proposed by Kirkland who proposed minimizing the least square function which that matches the phase to the measured intensity.[46]

Another approach, using the transport intensity equation (TIE), defines the intensity for a phase object in which amplitude fluctuations are negligible, as[47,48]

$$\psi(\vec{r}, \Delta f) \approx \sqrt{I(\vec{r}, \Delta f)} exp\{i\phi_{\Delta f}(\vec{r})\} exp\{ikr\} \qquad \text{Eq. 1. 14}$$

and expresses the wave propagation as

$$\frac{2\pi}{\lambda}\frac{\partial}{\partial z} I(\vec{r}, \Delta f) = -\nabla_{xy}\left(I(\vec{r}, \Delta f)\nabla_{xy}\phi_{\Delta f}(\vec{r})\right) \qquad \text{Eq. 1. 15}$$

It is possible to approximately solve the equation analytically, however a full solution can be evaluated numerically.[49]

The flux preserving non-linear wave reconstruction algorithm, which is the basis of the in-line reconstruction algorithm used in this thesis, will be discussed in detail in Chapter 2, together with the introduction of the implementation of the TIE to the algorithm.[25,26]

1.5. Comparison of In-line and Off-axis Electron Holography

Comparison of in-line and off-axis electron holography was done by Koch[50] and Latychevskaia[51] studying theoretical limits and the experimental point of view, respectively. This sub-section summarizes some of the key points of these two papers, which are highly relevant to the content of this thesis.

Table 1. 1 Summary of the different aspects by which were compared off-axis and in-line holography[50]

	Off-axis Holography	In-line Holography
Number of exposure	1	at least 2 or 3
Reconstruction	fast (linear)	slow (non-linear)
Coherence requirement	very high	low
Microscope alignment	need special and precise alignment	standard
Sample drift and mechanical stability sensitivity	High	low
Sample requirements	only possible near edge	no limitation
Experimental requirements	electrostatic biprism	energy filter
Quantitativeness	very quantitative	approximately quantitative
Phase sensitivity	moderated (depends on field of view)	high (depends on relative defocus)
Achievable resolution	limited	< information limit
Ideal for what bandwidth	low spatial frequencies	high spatial frequencies

The most obvious difference between these two techniques is the external hardware requirement of off-axis electron holography. In contrast to in-line electron holography, off-axis electron holography, requires a much simpler reconstruction scheme. However, an electron biprism (a very thin charged wire) has to be installed near an intermediate image plane of the microscope. Reconstruction can then be performed by linear Fourier filtering.[33]

This also affects the region of interest which has to be close enough to the vacuum and aligned properly with the biprisim orientation. For in-line electron holography, an energy

filter might be desired as extra hardware in the case that the inelastic scattering contribution is undesired. Off-axis electron holography proposes a fast and straightforward reconstruction, where in-line electron holography requires a long computation process. The resolution and phase sensitivity depend on the biprisim voltage for off-axis electron holography. Increasing the biprisim voltage enhances the resolution, but on the other hand the signal to noise ratio diminishes, which affects the phase sensitivity. Theoretically, the resolution limit is the information limit of the microscope for in-line electron holography. The high spatial frequency information transfer is very efficient at low defocus values, highest at $D_{Z_{Scherz}} = -1.2\sqrt{\frac{C_s}{k}}$.[52] However, in practice it is determined by the objective aperture that is used. The main advantage of off-axis electron holography is its quantifiability. For strong phase objects, in-line electron holography fails on quantification due to the missing low spatial frequencies, where off-axis electron holography recovers all spatial frequencies equally. Higher coherence increases the fringe contrast in off-axis electron holography. Intentionally making the illumination conditions astigmatic in one direction enhances the coherence in one direction. This is the reason for the common usage of elliptical illumination in off-axis electron holography. Of course, this requires sensitive alignment. On the contrary, coherence is less critical for in-line electron holography. So, it allows using a less coherent beam which increases the current density.

2. In-line Electron Holography with Flux Preserving Non-Linear Wave Reconstruction

Fresnel fringes, the oscillatory features that can be found in images that have been recorded under (partially) coherent illumination and out-of-focus conditions, contain information about the phase component of the complex wave of which the recorded image is the probability density. In the TEM Frisnel firinges can be used to detect material consisting of very light elements, or as a guide for focusing, since it is sensitive to very small relative optical path length differences experienced by the electrons as they pass through the sample. The phase of the wave function cannot be recorded directly. As mentioned before, the idea of recovering the wave-function in the TEM using interference between a reference wave and an object wave was first suggested and demonstrated by Gabor.[3] The Fresnel fringes form as a result of interference of the waves scattered by the sample with the unscattered wave which are visible out of focus conditions.

There are different reconstruction algorithms based on either the linear or non-linear imaging models, i.e. whether only the interference between the undiffracted and the diffracted waves, or also the interference between different diffracted waves, is taken into account. Although all of these algorithms have their strengths, none of them are able to recover the full spectrum of spatial frequencies of the phase.

In non-linear in-line electron holography, the object wavefunction is its own reference wave, avoiding the need for an electrostatic biprism. The wavefunction can then potentially be reconstructed at the full image resolution. This thesis employs an iterative flux-preserving in-line holography reconstruction algorithm,[25] [18] which minimizes the difference between defocused images (in-line holograms) simulated from the current estimate of the electron wavefunction at each iteration and the experimental measurement, taking into account incoherent aberrations (partial spatial and temporal coherence) and refining values of experimental parameters such as defocus Δf, the illumination convergence semi-angle α, image registration, and defocus-induced distortions, which are all only known approximately. The image intensity $I(\mathbf{r},\Delta f, \xi)$ of any member of the focal series at defocus Δf

and illumination ellipticity ξ, from which the wave function $\Psi(\boldsymbol{r})$ is to be reconstructed, is given by

$$I(\vec{r},\Delta f,\xi) = FT^{-1}\left[FT[I_\Delta(\vec{r},\Delta f)]\cdot E_{spat}(\vec{q},\Delta f,\xi)\cdot MTF(\vec{q})\right] \quad \text{Eq. 2. 1}$$

where,

$$I_\Delta(\vec{r},\Delta f) = \left|FT^{-1}\left[FT[\Psi(\vec{r})]\cdot CTF(\vec{q},\Delta f)\cdot E_{temp}(\vec{q})\cdot H(\vec{q})\right]\right|^2 \quad \text{Eq. 2. 2}$$

$$CTF(\vec{q},\Delta f) = exp(i\pi\lambda|\vec{q}|^2[\Delta f + 0.5\lambda^2 C_s|\vec{q}|^2]) \quad \text{Eq. 2. 3}$$

$$E_{temp}(\vec{q}) = exp\left(-\left[0.5\pi\lambda\Delta_f|\vec{q}|^2\right]^2\right) \quad \text{Eq. 2. 4}$$

$$H(\vec{q}) = \begin{cases} 1, & \lambda|\vec{q}| \le \theta_{max} \\ 0, & \lambda|\vec{q}| > \theta_{max} \end{cases} \quad \text{Eq. 2. 5}$$

$$E_{spat}(\vec{q},\Delta f,\xi) = exp\left(-\left[\pi\alpha\lambda\Delta f\left(q_x^2 + \xi q_y^2\right)\right]^2\right) \quad \text{Eq. 2. 6}$$

In Eq. 2.2, the flux-preserving approximation[25,18] has been adopted, which, in case of negligible the spherical aberration effects C_s on the spatial coherence envelope $E_{spat}(\boldsymbol{q})$ (Eq. 2.6), accounts more accurately for the intensity distribution in in-line holograms than the more widely used quasi-coherent approximation. In the above formulae, the coherent transfer function CTF($\boldsymbol{q}$) (Eq. 2.4) has (for readability reasons) been limited to include only the effect of defocus (Δf) and spherical aberration (C_s), but can easily be extended to include any other coherent aberration coefficient as well. The ellipticity ξ of the illumination is explicitly included in the envelope function accounting for partial spatial coherence $E_{spat}(\boldsymbol{q})$ which here assumes the direction of high spatial coherence (characterized by the semi-convergence angle α), i.e. the direction normal to the biprism in an off-axis holography experiment, to lie along the x-axis. Furthermore, an objective aperture H($\boldsymbol{q}$) (Eq. 2.5) admitting only scattering angles less than θ_{max} and a partial temporal coherence envelope $E_{temp}(\boldsymbol{q})$ (Eq. 2.5) depending on the focal spread Δ_f are used.

The reliability of the reconstruction was calculated by the M value (eq. 2.11) which is based on the statistical method called *cross validation.* It is used to measure the agreement between crystallographic model and the experimental x ray data as a crystallographic M factor.[21] Here, M value was used to measure the agreement between experimental and simulated data.

$$M = \frac{\sum|I_{sim} - I_{exp}|}{\sum I_{exp}} \quad \text{Eq. 2. 7}$$

2.1. Investigation on Bi_2Se_3

2.1.1. Introduction

Topological insulators belong to a very exciting class of materials due to their special electrical properties,[53] especially the fact that their conductivity is topologically confined to special surfaces only. Because of this strange behavior, they are considered a class of material different from conductors, insulators, semiconductors, or superconductors.[54,55] Currently, Bi_2Se_3 is probably the most studied prototype of this class of materials. Bi_2Se_3 has a rhombohedral crystal structure; its structure is composed of repetitive Se1-Bi-Se2-Bi-Se1 layers and the high anisotropy in the interface of two layers causes spin-orbit splitting even without any external magnetic field.[56,57] This spin-orbit splitting causes the formation of a Dirac cone on the surface, as detected by the quantum Hall effect. Beside this, there is also band bending near the surface, which can lead to the formation of a 2 dimensional electron gas (2DEG).[2] The observation of the electrostatic potential *V(r)* resulting from the charge density distribution at the surface of Bi_2Se_3 with sub-nanometer spatial resolution via in-line electron holography was the main focus of this study.

Elastic scattering of fast electrons in a transmission electron microscope (TEM) is determined by the distribution of electrostatic and magnetic fields the electron wave encounters on its path through the thin sample. In the absence of magnetic fields, and applying the phase object approximation (POA), i.e. neglecting the curvature of the Ewald sphere of the fast electron within the sample, the electrostatic field distribution shifts the phase $\phi(r)$ of the electron wave function (see, e.g.in Fig. 2.1b) according to Eq. 2.8 [58]

$$\phi(x,y) = C_E V(x,y)t \qquad \text{Eq. 2. 8}$$

This phase shift cannot be measured directly, but only the probability density (intensity) of the electron wave function, i.e. the square of its amplitude. The amplitude contrast observed in TEM images (e.g. Fig. 2.1a) is due to absorption of electrons, scattering outside the objective aperture or energy filter window, or their redistribution due to microscope aberrations, such as defocus, astigmatism, or spherical aberration. Since the so-called twin image problem in in-line holography, an artifact inherent in Gabor's original linear

reconstruction technique using an optical bench, can be overcome by recording more than just one in-line hologram and let computer programs solve the full non-linear set of equations (*see e.g.*[25]).

It has been shown that in-line holography can use the recorded signal more efficiently than its off-axis counterpart,[50] which is why this method was chosen for the current investigation.

Once the phase shift of the electron wave function has been reconstructed, the charge density is calculated by taking the Laplacian of the electrostatic potential according to the Poisson equation (eq. 2.9).[59] The electric field distribution (Eq.2.10) was calculated by taking the gradient of electrostatic potential [17] which was derived according to eq. 2.9.

$$-\Delta V(x,y) = \frac{\rho(x,y)}{\varepsilon_0 \varepsilon_r(x,y)} \qquad \text{Eq. 2. 9}$$

$$-\nabla V(x,y) = E(x,y) \qquad \text{Eq. 2. 10}$$

2.1.2. Method and Experimental Procedure

The Bi_2Se_3 single crystal which was prepared by the Vertical Bridgman Method,[60] was cut perpendicular to the basal plane (the quintupels' stacking direction is (110), via utramicrotomy. While cutting the sample a diamond knife, was used at a 35° angle, at high speed and without oscillation. Then, it was investigated with the 200 kV Sub-Electron-Volt-Sub-Angstrom- Microscope (SESAM)[61] (Carl Zeiss NTS, Germany). The in-column Mandoline filter was used for elimination of inelastically scattered electrons using an 8 eV energy slit and an illumination angle of 30 µrad.

For the in-line holography experiment a focal series with a non-linear defocus increments was acquired on a 2048 X 2048 pixel (Gatan UltraScan 1000, USA) CCD camera using the "FRWR tools" plug-in[62] for Digital Micrograph which fully automates the acquisition and also compensates for specimen drift during the acquisition. The nominal defocus values were set according to $\Delta f_n = 400\ nm*n^3$, n = … -2, -1, 1, 2 …, in order to efficiently sample phase information at both low and high spatial frequencies. Then, the exit surface wave function was reconstructed using a flux-preserving wave reconstruction algorithm.[25,26] This algorithm applies fully non-linear imaging theory, and assumes negligible

third or higher order aberrations, an assumption which holds very well for aberration-corrected microscopes or when using a small objective aperture (3.2 mrad) as used in the experiments. For the reconstruction, the MTF has not been taken into account.

To determine the mean thickness, which is necessary to calculate the electrostatic potential from the phase shift, a thickness map was recorded using the in-column Mandoline filter with an 8 eV slit width and 2 sec. exposure time at 1x1 binning.

Finally, using eq. 2.8 the electrostatic potential is obtained by dividing the phase image by the local thickness and C_E.

2.1.3. Results and Discussion

The reconstructed amplitude and phase images using the FPWR algorithm are shown in Figure 2.1. The M value, which is a measurement of mismatch between the simulated and the experimental images, calculated as 0.04 according to Eq. 2.7, which is <0.1, indicating a reliable reconstruction. Figure 2.2 shows both experimental and simulated images of the reconstructed wave function across a defocus value range of -10 / 10 µm. At each defocus, the consistency between experimental and simulated images is another sign of success of the reconstruction, in addition to theM value.

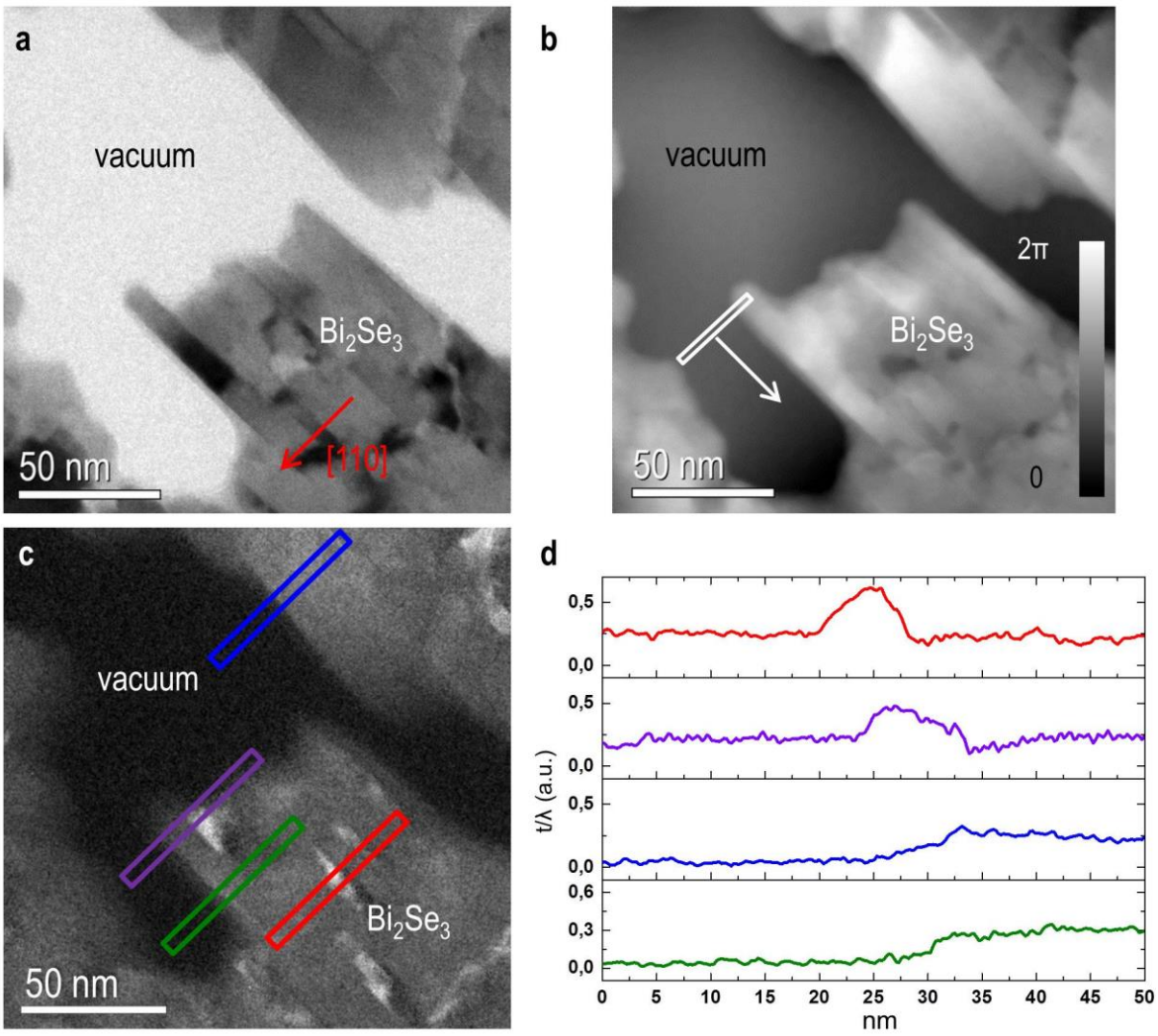

Figure 2. 1. Phase shift as a result of potential change: a) TEM bright field image of the Bi_2Se_3 in the vacuum. b) Phase difference map of the same area M = 0.044. c) Thickness variation map. d) The thickness profiles which are shown with boxes in c.

In order to calculate the mean inner potential, the phase map must be divided by the thickness and the energy dependent constant C_E=0.026 1/nmV (at an accelerating voltage of 200 kV), as given in eq. 2.8. For this purpose, the EFTEM thickness map, which is actually t/λ_{IMP} map (λ_{IMP} is the inelastic mean free path), shown in Figure 2.1c was recorded.

Unfortunately, an exact match between thickness and phase map is impossible, not only because of the differences in conditions, but also because the features at the edges in the thickness map, to increase nearly 20 %. One possible interpretation of this strong increase can be the excitation of surface plasmons, which locally increases the fraction of electrons

undergoing inelastic scattering, thus decreases λ_{IMP} and therefore increases t/λ_{IMP}, along the conducting surface of the sample.

Furthermore, the bright field image (Fig. 2.1a), apart from the bending contrast, looks homogeneous which indicates that the physical specimen thickness is indeed homogeneous around the sample edge, and there is no abrupt increase except at the edges. In the thickness map, there is high diffraction contrast in some regions (Fig. 2.1c-d) which were caused by bending of the sample. For this reason, the average thickness of the homogenous areas was used in division which netuarly increases the errors.

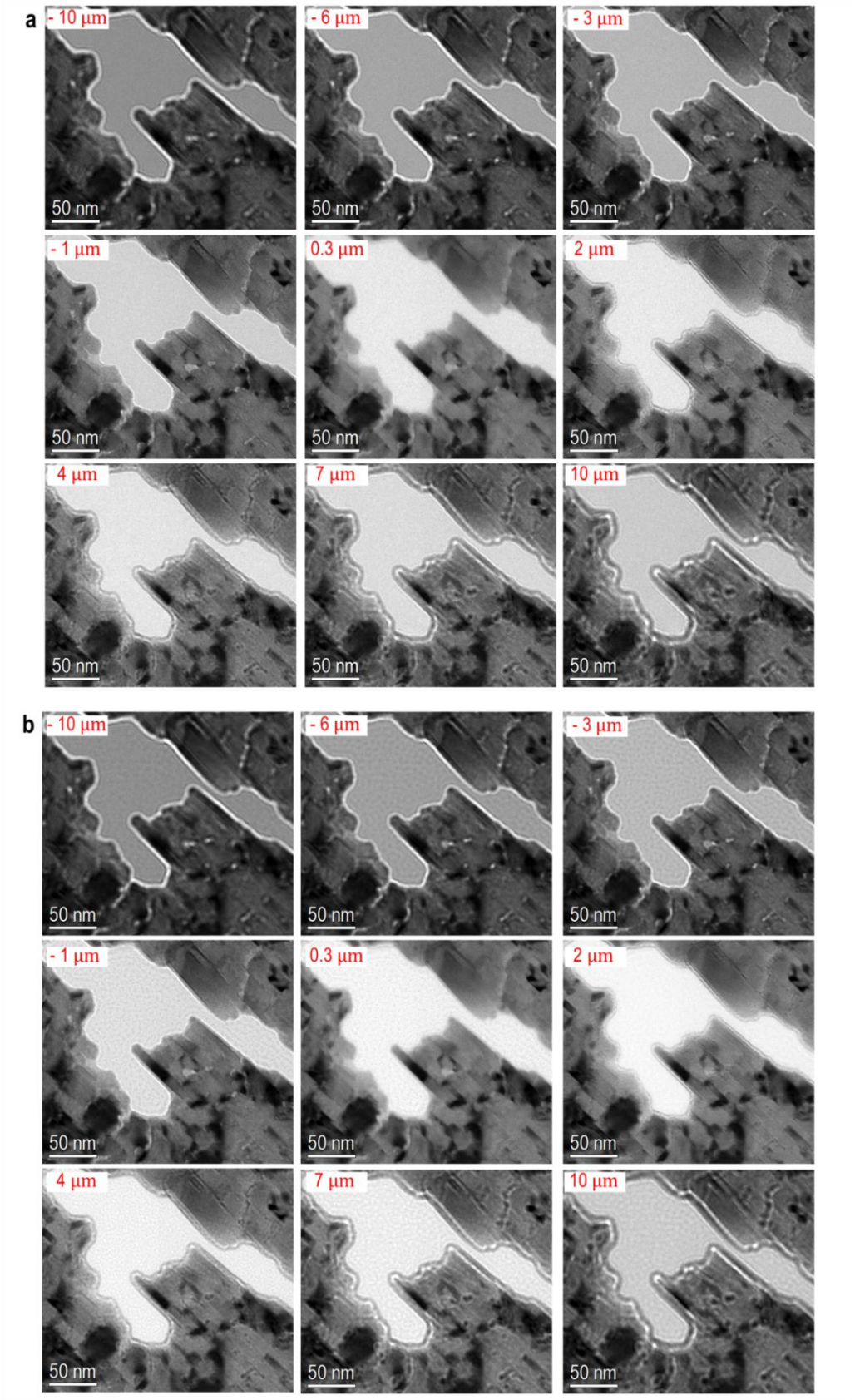

Figure 2. 2 a) Experimental images acquired in the focus range between -36.6 to 17µm. b) Simulated images using the reconstructed wave function. Final M value, the measure of mismatch between measured and calculated images, is 0.044 which is caused by the artifacts seen in simulated images.

The derived mean inner potential from the phase map was used for calculating the charge density distributions. As shown in eq. 2.9, the mean inner potential is a function of charge density and dielectric constant (function) of the materials. The Laplacian of the phase map and the profiles for basal and transverse plane are presented in Fig. 2.3. The charge distribution values in Table 2.1 were calculated from the profiles in Fig. 2.3, c and d under the assumption of fixed dielectric constants for the bulk and surface[63] and the thicknesses are also given in Fig. 2 c, d profiles. At the basal surface extra and unbalanced positive charges were observed in comparison to the distribution of the charges around the amorphous layer just outside of the Bi_2Se_3 edge and the transverse direction. The sum of the charges on both sides of the amorphous layer and the basal direction are zero. On the contrary, the (110) surface behaves differently, with more positive charges accumulating inside the material across a shorter range compared to the negative charges. This behavior of the (110) surface was observed several times in many samples which were prepared from different areas of the Bi_2Se_3 crystals. Eventually, from the Laplacian of mean inner potential, it was not possible to observe a 2DEG. However, it is known that in semiconductors, the free carrier concentration is low and this may cause a longer screening length.[22] Large screening lengths in a low carrier density system can be the explanation of this behavior. Furthermore, since charge neutrality has to be conserved in the material, there must be the same amount of positive and negative charges in the system which might prevent the direct detection of 2DEG.

Table 2. 1 Possible local charge distributions with different dielectric constants

	Relative Dielectric Constant[63]	Electron Charge Density (C/nm²)	Depth from the Surface (nm)
basal plane	113 (ε_0)	1.0505E-08	0.67
		3.6482E-09	1.57
		1.9706E-09	2.46
	29 (ε_∞)	2.6961E-09	0.67
		9.3627E-10	1.57
		5.0574E-10	2.46
transverse planes	113 (ε_0)	2.7780E-09	0.67
		2.5971E-09	2.46 (average)
	29 (ε_∞)	7.1293E-10	0.67
		6.6652E-10	2.46 (average)
noise	1	1.6628E-11	-

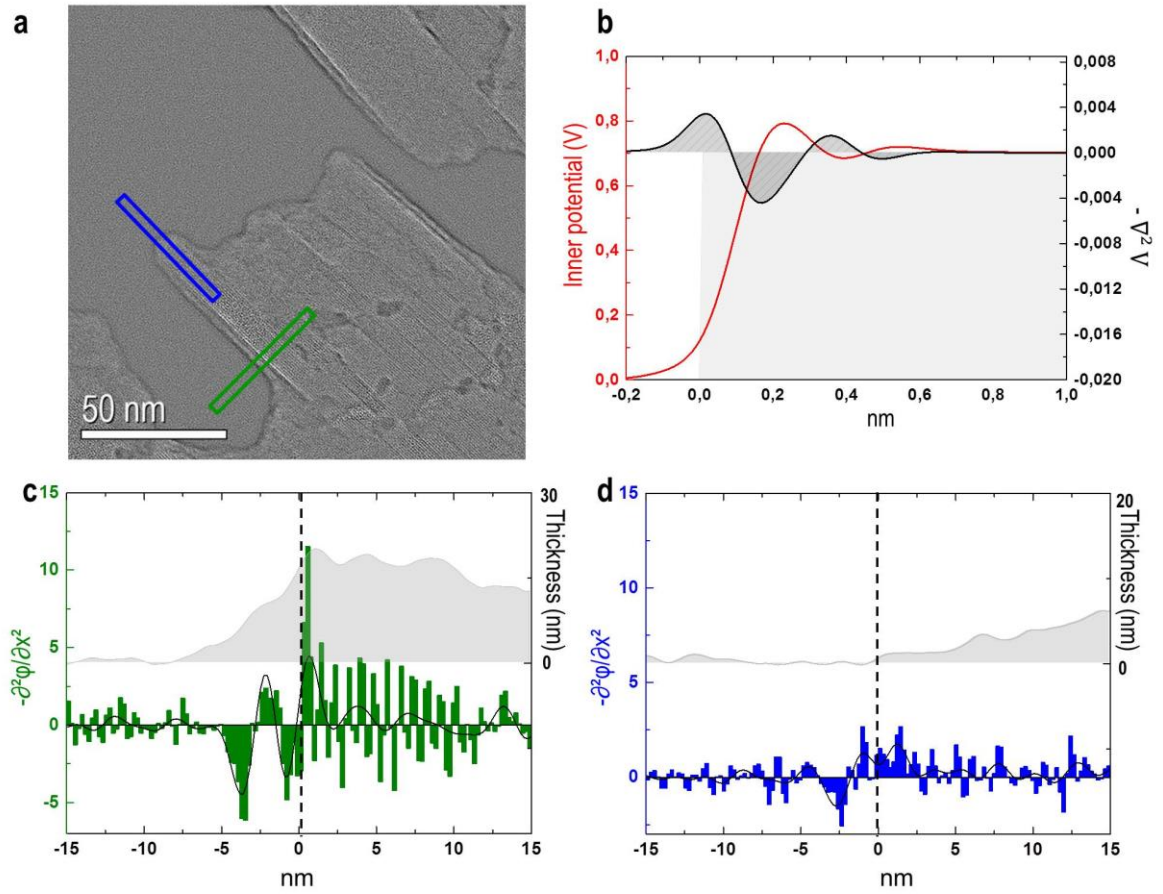

Figure 2. 3. Possible real space charge distribution of the 2DEG in Bi_2Se_3 a) Laplacian of the phase map. b) Schematic view of the Laplacian of mean inner potential (charge distribution). c) Thickness variation and Laplacian of mean inner potential in basal plane. d) Thickness variation and Laplacian of mean inner potential in transverse direction. The dashed line shows where the Bi_2Se_3 surface starts.

Although the charges couldn't be observed directly in the charge density map, they create an electric field and this electric field can help with understanding the charge distribution. For this purpose, the calculated mean inner potential from the phase map was used to derive the electrical field (Fig. 2.4) according to eq. 2.10. Fig. 2.4b shows an extreme increment of the field at the surface. This can be attributed to not only the change of the electric field but also the absence of low spatial frequencies which cannot be fully covered by in-line holography. This problem (abrupt thickness increase) can be solved by subtracting of a Gaussian function and also subtracting the electric field function. The Gaussian width was taken to be 1 nm by considering the objective aperture. However, this subtraction was still not enough to explain the behavior of the positive charges on (011) surface of Bi_2Se_3 because the electric field which was obtained is still the sum of the all charge effect. Based on the requirement of charge neutrality effect, the positive changes were tried to

deconvoluted from the electrical field. Then the potential was replotted starting from the Bi_2Se_3 edge, and ~ 2 nm to the inside the materials showed p type band bending (Fig. 2.4c).

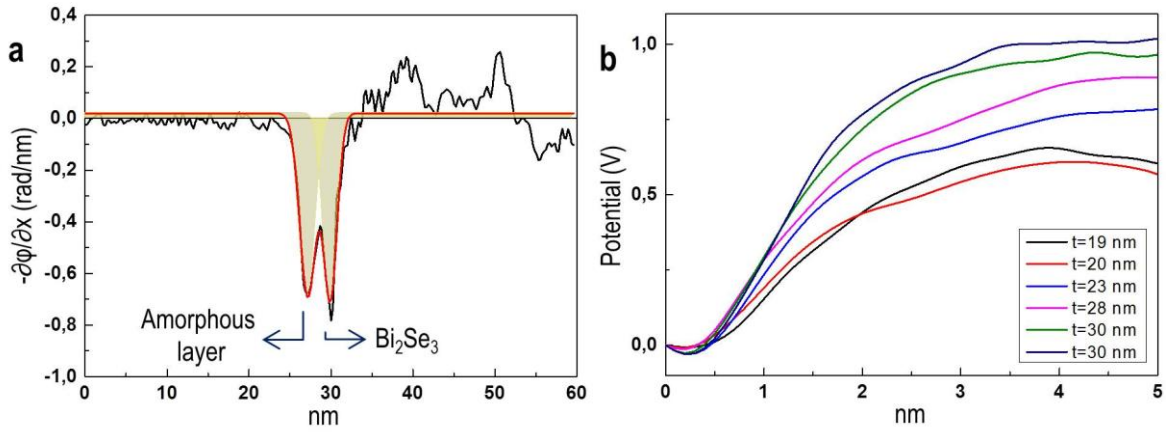

Figure 2. 4. Electric field variation: b) Electric field profile of the sample including thickness effects. c) Electric field profile of the sample after subtracting a Gaussian background. d) The potential difference of the regions. The white box in Fig. 1a) shows the starting point (0 nm) of the profiles and white arrows show the propagation direction.

According to Zhang[57] et. al. the number of quintuples, which is the unit cell includes five atomic layers (Se-Bi-Se-Bi-Se) alog the c –axis, affects the properties of Bi_2Se_3. To be able to see the effect of the quintuples amount on the mean inner potential, 10 quintuples layer Bi_2Se_3 shown in Figure 2.5 was investigated. Even though, some intensity increase on the Laplacian of the phase was observed in 10 quintuples system, this effect is almost 6 times lower than the sample shown in figure 2.3a where the amount of quintuples region is higher. Furthermore, Fig. 2.5 b also shows the how the Laplacian (mean inner potential dependent) at the first quintuple layers is affected by surface discontinuities.

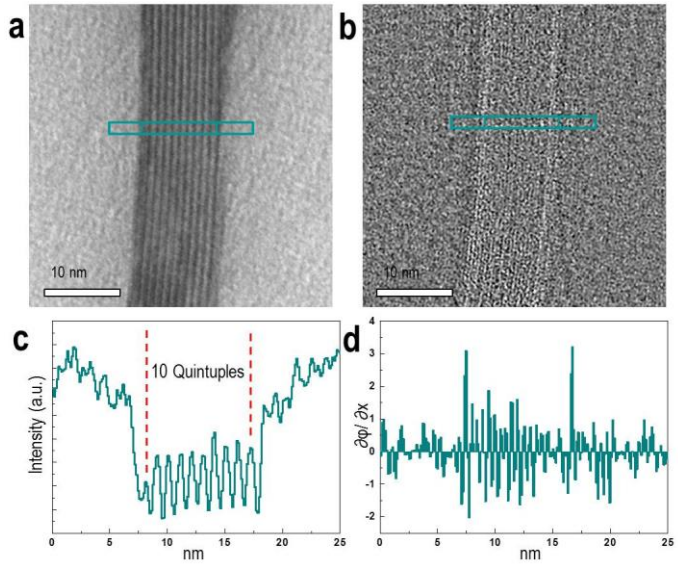

Figure 2. 5. Effect of number of quintuples on the formation of a 2DEG: a) TEM bright field (BF) image of a Bi_2Se_3 particle on top of a carbon film. b) Charge density distribution map calculated with ε_0=113[63] (reconstruction M factor is 0.048) c) BF image profile which shows the number of quintuples. d) Charge density distribution profile.

Due to both the electric field and the charge density distribution, the positive charge localization at the surface and the p-type band bending can be attributed to the existence of a 2DEG. However, missing low spatial frequencies make it impossible to prove its existence with certainty. Therefore, two approaches were utilized for the efficient recovery of the spatial frequencies with a wider bandwidth; firstly, a new Gradient-Flipping Assisted Flux-Preserving Wave Reconstruction (GF-FPWR) algorithm, developed by Prof. Christoph T. Koch, was applied for the first time within the scope of this work to recover low spatial frequencies more efficiently. Secondly, a new method was developed hybridizing the off-axis and in-line holography schemes for the recovery of the full range of spatial frequencies.

2.2. Full-Resolution High-Contrast Imaging of Phase Objects by Gradient-Flipping Assisted Flux-Preserving Wave Reconstruction

2.2.1. Introduction

In in-line electron holography a series of images is recorded at several focal planes above and below the plane where the specimen is in focus. If the defocus is small, the interference is very local, and the resulting fine Fresnel fringes carry information about high spatial frequencies of the phase. At large defocus, limited spatial coherence dampens the Fresnel fringe contrast, because the lateral coherence length imposes an upper limit on the distance across which interference can occur. Therefore, in-line electron holography is very efficient for recovering high spatial frequency phase information. Relative phase information across distances longer than the lateral coherence length can be obtained by non-interferometric reconstruction algorithms such as the. TIE[47] Combining both gives access to both high and low spatial frequencies of the phase simultaneously.[64] However, using the TIE requires knowledge of either the phase or its gradient at the boundary condition of the reconstructed area, or assuming that the boundary conditions are periodic. Iterative nonlinear reconstruction algorithms, such as those based on the work of Gerchberg and Saxton[22] require much more computing power than solving the TIE under periodic boundary conditions or the reconstruction of off-axis holograms.

The motivation for developing gradient flipping-assisted flux preserving wave reconstruction (GF-FPWR) is that in many TEM investigations of non-magnetic and non-charging specimens the phase in the vacuum areas within the field of view is constant, and the slab-geometry of many TEM samples causes the phase to be more or less flat also inside large parts of the specimen, at least at medium resolution. This means that the gradient of the phase is often quite sparse, especially when excluding the high spatial frequencies.

In its original application, the charge flipping algorithm was developed for solving crystal structures from X-ray diffraction data,[65] and is very effective in finding a sparse solution in the domain of the charge density by flipping the sign of small values and keeping values above a given threshold while enforcing consistency with the measured diffraction

intensities. This principle has been adapted to in-line electron holography by inserting a phase-modifying procedure every few iterations (e.g. every 3rd iteration) of an iterative reconstruction algorithm (the FPWR algorithm[25,26] was used for the examples presented below), flipping the sign of small values of each of the two components of the gradient of the phase and reducing its amplitude. This is implemented by simply multiplying these values by a scale factor β slightly larger than -1 e.g. β = -0.97. This operation is only performed within the field of view defined by the experimental data. The size of the array defining the reconstructed phase is larger than this field of view, in order to accommodate non-periodic boundary conditions. While the large array has periodic boundary conditions, the array corresponding to the field of view of the experimental data may have any boundary, because it lies within the typically 1.5 to 2 times larger array that is reconstructioned with periodic boundary conditions.[66] Once the small gradients have been flipped, the modified phase is obtained by 'inverting' the modified gradient $\vec{G}'(\vec{r})$ to obtain a new estimate of the phase $\phi'(\vec{r})$ which is then further refined by successive iterations of the applied non-linear reconstruction algorithm.

The Fourier transform of the modified phase $\phi'(\vec{q})$ is obtained from the modified gradient by the following operation:

$$\phi'(\vec{q}) = \phi(\vec{q})[1 - exp(-r_c^2 q^2)] + FT\left[\vec{\nabla}.\overrightarrow{G'}(\vec{r})\right]\frac{\exp(-r_c^2 q^2)}{q^2} \qquad \text{Eq. 2. 11}$$

where r_c defines the distance below which the flipping of the gradient will have no effect. Dividing by $-q^2$ effectively implements an inverse Laplace operator. At q=0 it simply multiply by 0 instead of dividing by it. This can easily be justified by the argument that the absolute phase is not a well-defined physical quantity. Multiplying by 0 at spatial frequency q=0 will cause the mean of the reconstructed phase to be set to 0. After the reconstruction an offset can be subtracted which corresponds to the mean of the phase in the vacuum. This has been done for the phase maps shown in the figures below.

The gradient flipping affects mostly those spatial frequencies of the phase which are significantly larger than r_c. Since most iterative focal series reconstruction algorithms reconstruct primarily the high spatial frequencies of the phase and typically require many iterations to affect the low spatial frequencies,[66] eq. 2.12 ensures that gradient flipping

minimaly affects the convergence of the iterative reconstruction algorithm. It may even help to speed up convergence, especially when large areas of the phase are flat, e.g. nanoparticles on a homogeneous support or if the field of view contains large areas of empty space.

2.2.2. Method and Experimental Procedure

In order to demonstrate the gradient-flipping assisted flux preserving wave reconstruction (GF-FPWR) algorithm, off-axis and in-line electron holography experiments were carried out for different samples: MgO cubes (Fig. 2.6a) a material commonly used for electron holography studies,[67,68] and core-shell nano-catalyst particles consisting of carbon nano-spheres with iron cores (Fig. 2.6b). The core-shell particles have fine features in the 0.5 and 0.8 nm range. This helps to test the applicability of the method for a wide range of spatial frequencies. The carbon layers are buckled, and display clear phase contrast.

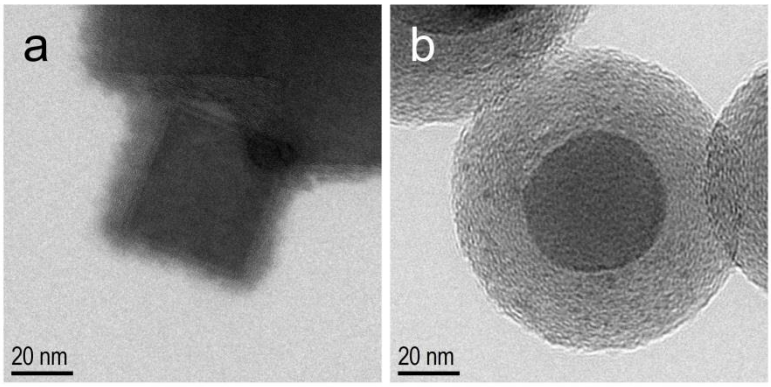

Figure 2. 6 Brigth field image of a) MgO cubes, b) Fe core C shell particles.

The off-axis holograms and focal series were acquired using an FEI Titan 80–300 TEM equipped with two electron biprisms and a Gatan imaging filter equipped with a 2048 × 2048 pixel CCD camera. The experiment was performed at an accelerating voltage of 300 kV.

When performing off-axis electron holography on the MgO nanocubes the biprism voltage was set to 80.5 V (0.45 nm fringe spacing) and for the C-Fe nanoparticles to 139 V (0.53 nm fringe spacing). The Holografree[69] software is used for the off-axis electron holography reconstructions. For both off-axis and in-line electron holography, a 10 eV energy selecting slit was inserted and centered on the zero-loss peak during the experiment, to reduce the contribution of inelastically scattered electrons.

The focal series was acquired from the same area using the FWRWtools[62] plugin for Digital Micrograph which fully automates the acquisition and also compensates for specimen drift during acquisition. The nominal defocus values were set according to the formula Δf_n = 400 nm ×|n|^{p}n/|n|, (where n=… -2, -1, 0, 1, 2 …). If p=2 or p=3 the phase information can be sampled very efficiently for both low and high spatial frequencies.[66] For the MgO cubes, the defocus values are between -260 and 330 nm, with 40 nm defocus steps at linear increments (p=1) and for the C-Fe nanoparticles the defocus values vary between -3.6 to 3.6 µm, again with linear increments (p=1) and a defocus step of 600 nm. As described above, the exit surface wave functions were reconstructed using the flux-preserving wave reconstruction algorithm[25,26] combined with gradient flipping (GF-FPWR).

2.2.3. Results and Discussion

Figure 2.7 displays the phase results obtained from the MgO cubes by the conventional in-line holography reconstruction algorithm (Fig. 2.7 a), the same algorithm combined with gradient-flipping (Fig. 2.7 b), and off-axis holography (Fig. 2.7 c). The phase obtained using the conventional in-line reconstruction algorithm varies between approximately -2 to 6 which is about 50 percent lower than the phase recovered by off-axis holography. Also a phase shift of -2π was observed (see phase profile shown in Fig. 2.7d) in the vacuum area just outside the specimen. This originates from missing low spatial frequencies in the phase information. Fig. 2.7b shows that gradient flipping prevents artifacts at the edges and gives a homogeneous background. Also, when comparing Figures 2.7b and 2.7c, the agreement is rather good. The remaining difference between the off-axis and GF-FPWR result of about 20% may be attributed to imperfect energy filtering during the acquisition of the focal series.

Another way to show the missing frequencies in the in-line reconstruction result is a power spectrum analysis. The most common way to perform a power spectrum analysis is by taking the radial average of the Fourier transform of an image. In this way, the amount of information transfer is obtained from the distrubiton of the signal as a function of frequency.

The power spectrum shown in Fig. 2.7e highlights the differences in information transfer of the three results. Although, the field of views are identical, the phase resolution

of the in-line electron holography reconstructions is 0.34 nm where the off-axis holography has 1.2 nm since a small reciprocal space mask had to be applied when reconstructing the exit wave from the off-axis data. Additionally, the power spectrum shows that the GF-FPWR algorithm recovers reliable information across distances of up to 80 nm, while the FPWR-reconstruction is only reliable across distances up to about 30 nm. Phase differences across distances larger than this could not be recovered by these in-line holography reconstruction algorithms.

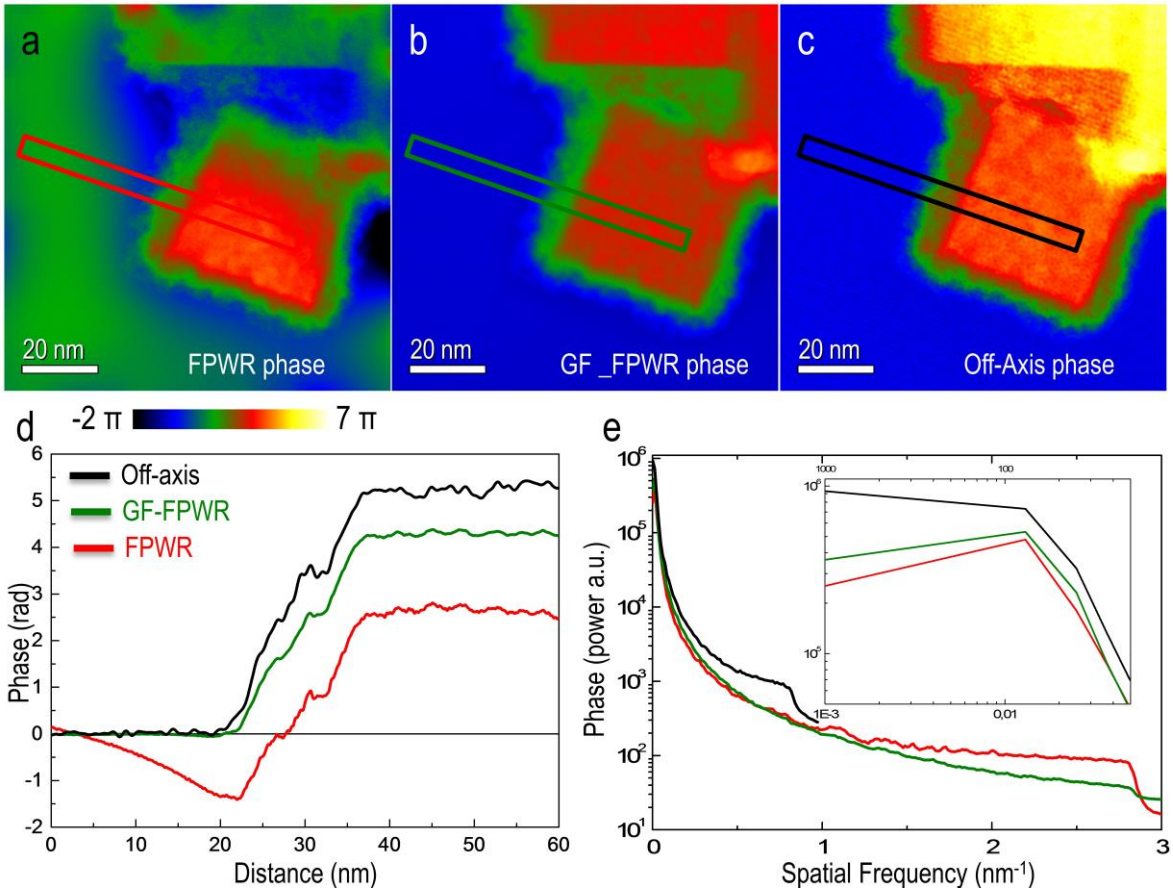

Figure 2. 7 Phase images of MgO cubes which are reconstructed by a) FPWR b) GF-FPWR and c) off-axis electron holography. d) Line profiles extracted from the 3 different phase reconstructions e) Radially averaged power spectra of the three phase maps.

Although the GF-FPWR reconstruction algorithm did not recover phase differences across very large distances, this example shows that the result of the conventional reconstruction algorithm could be improved, since the artifacts at the edges of the field of view have been reduced, and the reconstructed phase looks much closer to the result obtained by off-axis holography, while retaining superior spatial resolution. This may help to measure quantities like mean inner potentials and charge densities more reliably.

The second example, the Fe core C shell particles, leads to a similar conclusion similar to the MgO cube reconstruction. The reconstructed phase maps obtained using conventional in-line (FPWR) reconstruction, GF-FPWR, and off-axis electron holography are shown in Figs. 2.8a, b and c, respectively. The conventional FPWR algorithm recovers phase differences up to π, whereas according to the off-axis reconstruction the phase should span a range of ~4π. While the FPWR reconstruction recovers phase differences of only ~77% of the range obtained by off-axis holography, this discrepancy reduces to ~44% when applying the GF-FPWR technique. Again, artifacts at the edges, visible in the conventional FPWR reconstruction in Fig. 2.8d (red line), were reduced by gradient flipping. However, the profile taken from the GF-FPWR reconstruction shows an offset in the phase within the vacuum region on the two opposite sides of the core-shell particle. This problem arises because the two vacuum regions are not connected. In Fig. 2.8e, the power spectra of the three reconstruction schemes is shown, confirming that the low spatial frequency information obtained usinf the proposed GF-FPWR algorithm is much closer to that of off-axis holography than the FPWR result.

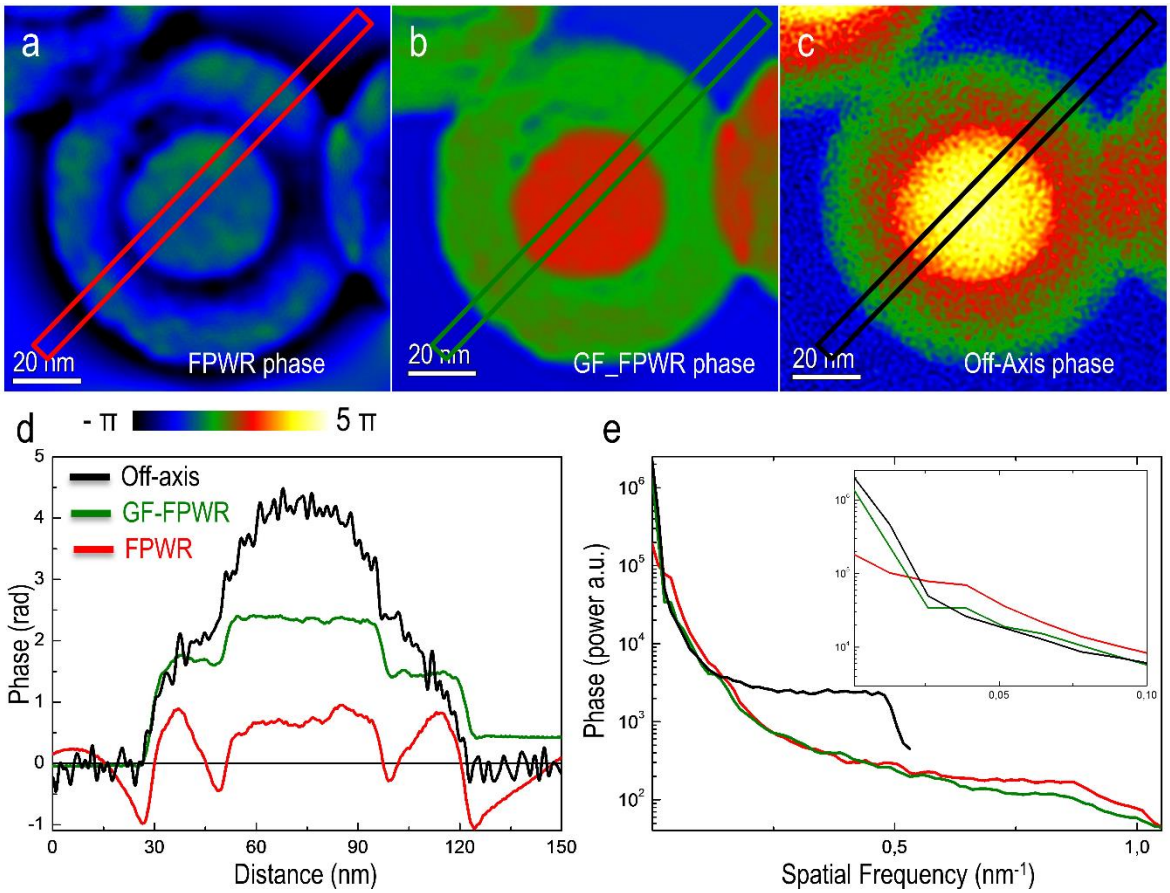

Figure 2. 8 Phase images of Fe shell C nanospheres which is reconstructed by a) FPWR b) GF-FPWR and c) off-axis electron holography d) Phase line profiles e) Power spectrum analysis.

As mentioned before, the r_c in equation 1, defines the spatial frequency above which the gradient flipping is active. Figure 4 summarizes the effect of r_c, by presenting phase images and profiles reconstructed with different r_c values from Fe-core C-shell particles. Initially, increasing r_c improved the contrast in phase proportionally. So, figures 4 a to d show that the lowest contrast recovery was obtained at r_c = 5 nm. The highest phase contrast was obtained when r_c was set to 25 nm (Fig. 2.9. g). Setting r_c too high does not improve the contrast anymore. On the contrary, this indicates the reconstruction proceeds as if no gradient flipping was applied. As an example, at low magnifications the main phase shift contribution comes from the thickness of the specimen, so if the r_c were set to a value much higher than the average specimen thickness, the algorithm proceeds as the conventional FPWR since the gradient flipping has been allowed only at very low spatial frequencies. This is why we start to observe dark features around the particle in Fig. 4f when very high threshold values were applied similar to Fig. 3a where reconstruction was carried out using conventional FPWR reconstruction. Moreover, the M value defined in equation 2.7, which measures the mismatch between experimental and simulated images during the

reconstruction, possesses the smallest value also at r_c = 25 nm. Figure 2.9h shows how the M values decrease with increasing *r*c until 25 nm then increase again. Minimum mismatch (M) is obtained also for the highest contrast case. Furthermore, the sample shown in Fig. 2.9 includes two different vacuum regions which are not connected to each other. Both sides of the particle should have the same phase shift in the region where the particle mean inner potential become zero. However, the phase profiles shown in figure 2.9i have different phase values on the two sides of the particle. Two separate vacuum regions create two different boundary conditions, causing different phase offsets. We observe minimum phase offset differences again in the case of the minimum M and the highest contrast was achieved when r_c is 25 nm.

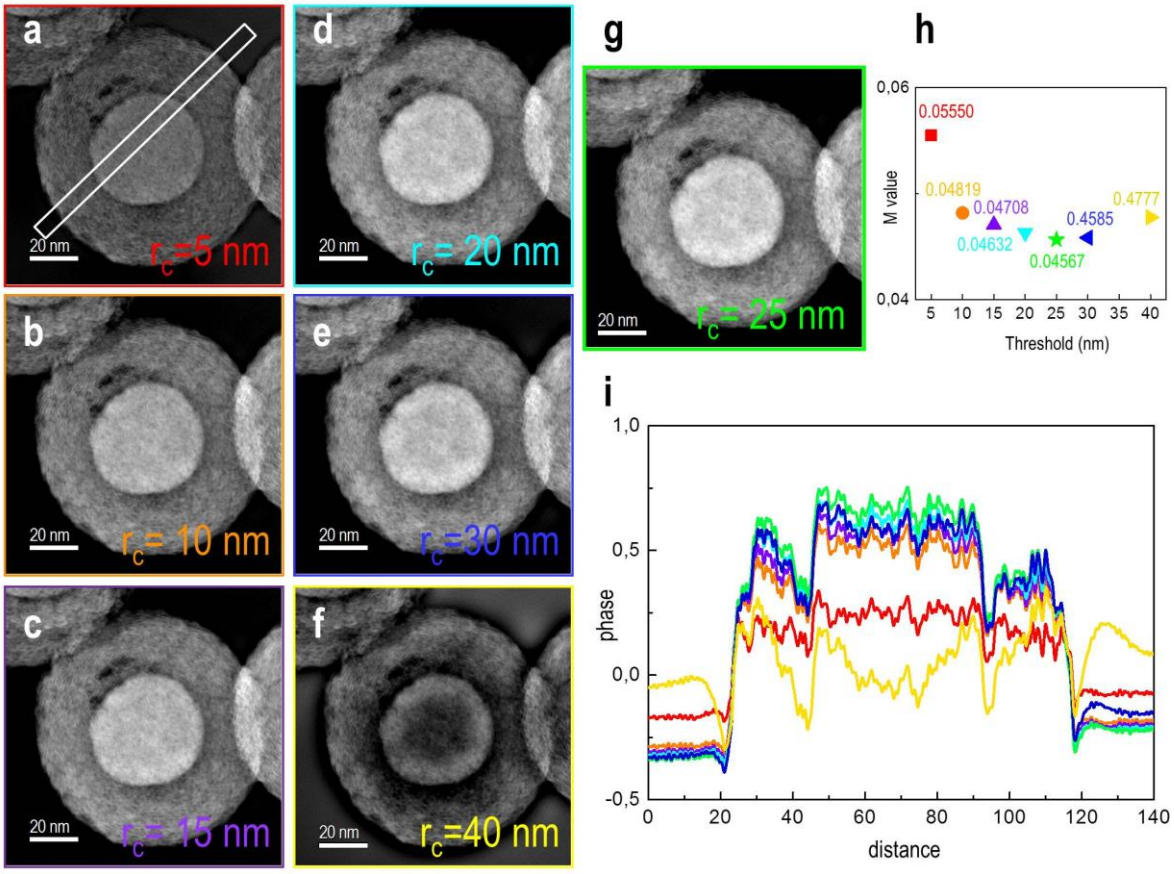

Figure 2. 9 Phase images of Fe shell C nanospheres which are reconstructed with a) 5 nm b) 10 nm c) 15 nm d) 20 nm e) 30 nm f) 40 nm g) 25 nm threshold values, h) threshold vs M value (the amount of mismatch between simulated and experimental images), i) line profiles of images a to g from the selected region shown in a).

3. Hybridization Approach to In-Line and Off-Axis (Electron) Holography for Superior Resolution and Phase Sensitivity

3.1. Introduction

Holography was proposed by Denis Gabor in 1948 "to offer a way around" the resolution-limiting spherical aberration of the TEM.[3] As a result of the development of the laser, the importance of holography as a technique for measuring both the amplitude and the phase of a wavefunction was soon realized and Denis Gabor was subsequently awarded the Nobel Prize in 1971.[70] In the TEM, holography is now used not only to correct microscope aberrations,[71] but also to characterize electrostatic potentials,[8] charge order,[72] electric and magnetic fields,[10] strain distributions,[11,12] semiconductor dopant distributions[13] and unstained biological specimens,[73] in each case with nanometer, sub-nanometer or even sub-Ångström spatial resolution. When examining biological or in general soft materials that contain primarily light elements, most structural information is carried in the phase of the elastically scattered wavefunction. However, such specimens are often beam-sensitive and require great care with regard to electron dose, as the ratio of inelastic (damaging) to elastic scattering events is high. It is therefore important to develop low-dose techniques for measuring the phase of electron wavefunctions quantitatively. Furthermore, investigating ordinary specimens over the full spatial frequency range with high resolution and high sensitivity is very challenging.

Holography, *i.e.*, coherent wavefront reconstruction, can be performed using a wide variety of experimental setups. For electron holography alone, Cowley identified 20 independent forms,[35] of which the two most widely used modes are off-axis and in-line electron holography. Off-axis electron holography was pioneered by Möllenstedt and Düker[21] and is based on the use of an electrostatic biprism, which usually takes the form of a charged wire placed in the electron beam path, as illustrated in Fig. 3.1a. The biprism is used to produce a fine interference fringe pattern, from which the complex wavefunction of the fast electron can be reconstructed using either linear algebra[74] or an optical bench.[75] In-line electron holography (see illustration in Fig. 3.1b),[3,76] which is also referred to as focal series reconstruction, works also at much lower degrees of spatial coherence than off-axis

holography, but requires the use of a computational algorithm to solve a non-linear[25,41,77] or, in some cases, approximated linear[39,78] set of equations. These equations relate the complex electron wavefunction $\Psi(\boldsymbol{r})$ to image intensities $I(\boldsymbol{r},\Delta f)$ that are usually recorded at multiple planes of focus each characterized by its defocus Δf from the reference focus, at which the wavefunction is to be recovered. Off-axis electron holography has good phase sensitivity at low spatial frequencies, whereas either a large defocus range,[26,79] or variable defocus steps (as recently published by Haigh et al[80]), or model-based approaches[81,82] must be used to approach faithful reconstruction of low spatial frequency phase information using in-line electron holography. At high spatial frequencies, both the spatial resolution and the phase sensitivity of in-line electron holography are higher than those of its off-axis counterpart for the same field of view and electron dose.[50,26]

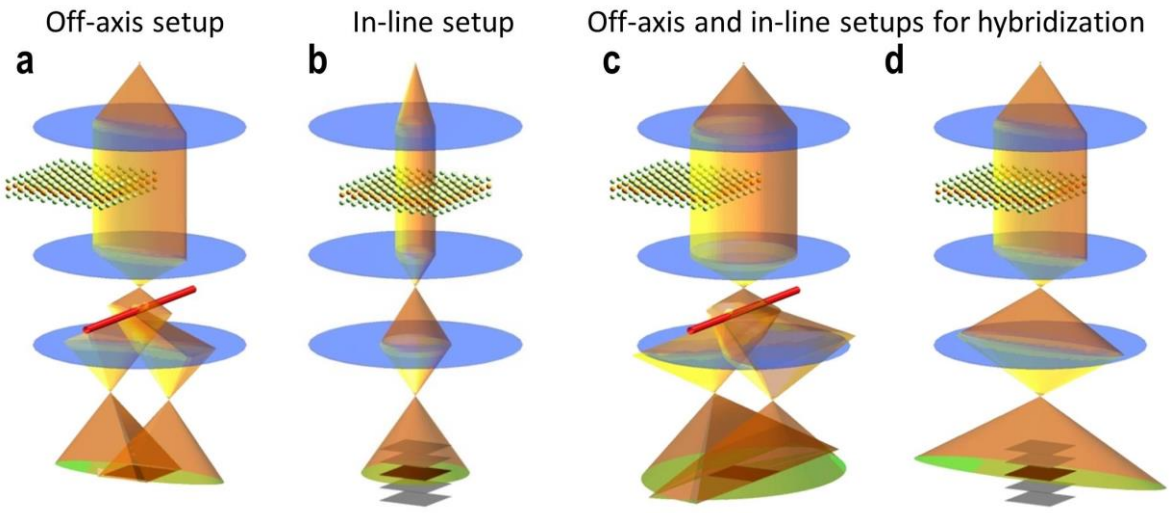

Figure 3. 1 Schematic view of microscope setups: (a) off-axis and (b) in-line holography. (c) Shows how the in-line data can be acquired immediately after switching off the biprism, in a fully automated fashion by simply shifting the image. (d) Shows how the data has been acquired for the present work: the biprism was retracted, and the sample was slightly shifted to allow investigation of identical specimen areas by both methods. Reprinted from Ozsoy-Keskinbora et. al. [83] with permission from Nature Publishing Group, copyright 2014.

Off-axis and in-line electron holography require very different optical setups for optimum performance and are highly complementary.[26,50,51,73] For maximum phase sensitivity, off-axis electron holography is typically performed with highly elliptical illumination (Fig. 3.1a) (ellipticity ratios of ξ=30 are common), whereas in-line electron holography is usually performed with isotropic spatial coherence (Fig. 3.1b). While high-frequency phase information is encoded very efficiently in in-line electron holograms,[50]

experiments that aim at the reconstruction of low spatial frequency phase information are much more reliable (and quantitative even when using a low electron dose) when carried out using off-axis electron holography. Because of its need for highly coherent illumination, electron dose rates in off-axis electron holography are typically low and exposure times are very similar to the total exposure time of a focal series acquired for in-line holography. These fundamental differences between the two methods result from how phase information is encoded. While the off-axis setup encodes all spatial frequencies equally strong (with a decrease in signal to noise ratio at higher frequencies), the phase sensitivity of in-line electron holograms is proportional to the spatial frequency squared ($\sim|\mathbf{q}|^2$), *i.e.*, it is low across long distances and higher for very fine details. For applications such as the measurement of magnetic fields, dopant distributions or concentrations of oxygen vacancies in oxides,[84] good phase sensitivity over the full range of spatial frequencies is required.

Here, an experimentally simple approach that combines in-line and off-axis electron holography and takes full advantage of their complementarity is presented, allowing a phase signal to be obtained with excellent signal-to-noise properties over all spatial frequencies. It also serves as a model for other holography applications at X-ray, microwave, radio, ultraviolet, visible optical wavelengths[85-91] etc., where shortcomings like the ones described above are observed due to the usage of either the in-line or the off-axis setup. The performance of the method is demonstrated by the investigation of iron-filled multi-walled carbon nano-onions. Off-axis and in-line electron holography experiments are carried out on the same region of the same sample with the same illumination conditions, allowing profiles of the projected electrostatic potential across individual particles to be determined quantitatively.

3.2. Methods and Experimental Procedure

In off-axis electron holography, the electrostatic biprism attracts the spatially coherent electron wave function on either side of it towards the optic axis of the microscope, thereby introducing a relative wavevector q_c between an object wave and a reference wave. The reference wave, which is usually part of the electron wavefunction that has not been scattered by the object, can often be regarded simply as a tilted plane wave. The Fourier

transform of the resulting interference pattern, which corresponds to the sum of an object wave $e^{2\pi i q_c . r} \times A(r).e^{i\phi(r)}$ and a reference wave $e^{-2\pi i q_c . r}$, is given by the Eq. 1.15.[74]

As shown in Fig. 3.1a, in order to achieve the necessarily very high spatial coherence perpendicular to the electrostatic biprism required for off-axis holography, the illumination is setup to be highly elliptical. The degree of ellipticity is defined by the number ξ, which is simply the ratio of the illumination convergence angles for the short and long axis of the ellipse. If the shear $\mathbf{q_c}$ is large enough, then the sidebands are separated from the central band in reciprocal space and a simple inverse Fourier transform of one of the sidebands yields the reconstructed wave function. Since only a relatively small part of the data is used for reconstruction, the resolution is at least 3-4 times lower than that of the recorded data set.

Nano-catalyst particles with a core-shell structure, consisting of carbon nano-spheres with iron cores, were selected as a test material to assess the limits of the method. The core-shell particles have fine feature sizes between 0.5 and 0.8 nm since the carbon phase is only partially crystalline. The carbon layers are buckled, and display clear phase contrast. This sample therefore works very well as a test object for assessing the spatial resolution of the method. In order to combine the two methods, an off-axis hologram and a focal series were recorded from the same area using an FEI Titan 80-300 TEM equipped with two electron biprisms and a Gatan imaging filter with a 2048×2048 pixel CCD camera. The experiment was carried out at an acceleration voltage of 300 kV. For this experiment both off-axis and in-line acquisitions were done using round illumination conditions having inserted a 30 µm objective aperture. First the off-axis electron hologram was acquired using a biprism voltage of 89.4 V (0.38 nm fringe spacing) to obtain an optimum field of view and resolution and a 20 s exposure time. Then, the biprism was turned off and retracted from the beam. The sample was shifted to bring the same area of interest back on the detector and a focal series was acquired from the same area using the "FWRWtools"[62] plugin, applying linear defocus increments with a 90 nm defocus step size. The illumination conditions were not changed between the off-axis and in-line holography data acquisitions (Fig. 3.1c). At each defocus, an image was acquired using a 3 s exposure time. The objective lens was used for changing the focus, following assumptions that are explained elsewhere.[18] For both off-axis and in-line

electron holography, zero-loss filtering, employing a 10 eV energy-selecting slit was used, in order to reduce the contribution of inelastically scattered electrons.

Reconstruction of the off-axis electron hologram was performed using the HolograFREE[69] software. For in-line and hybrid reconstruction, a flux preserving non-linear in-line holography reconstruction algorithm[25,26] was used. This method takes into account the modulation transfer function (MTF) of the CCD camera (whose effect is shown in Fig. 3.2), as well as partial spatial coherence and defocus-induced image distortions. The algorithm also refines experimental parameters such as defocus and the illumination convergence angle. In order to combine the two methods, the same region of interest that was selected for in-line electron holography was aligned with the amplitude images obtained from the off-axis reconstruction. Then, the in-line reconstruction algorithm was re-run, starting from the off-axis amplitude and (unwrapped) phase, refining the imaging parameters that were fitted during the first in-line reconstruction. Since the phase and amplitude that were obtained from the off-axis data were also used for an initial guess using the hybrid method, the same illumination conditions were assumed for the off-axis and in-line data. The thickness measurement required for determining the mean inner potential was obtained by energy filtered TEM (EFTEM) thickness mapping, with mean free paths calculated using David Mitchell's mean free path estimator script.[92] In the region at the center of the particle, where both iron (Fe) and carbon (C) are present, a mean free path of 183.3 nm was assumed. This value was calculated according to the volume ratio of Fe to C, for which the Fe core was assumed to be spherical with a radius of 7.5 nm and the particle radius was assumed to have a measured value of 22.5 nm. For the C shell region, a mean free path of 188.3 nm was used.

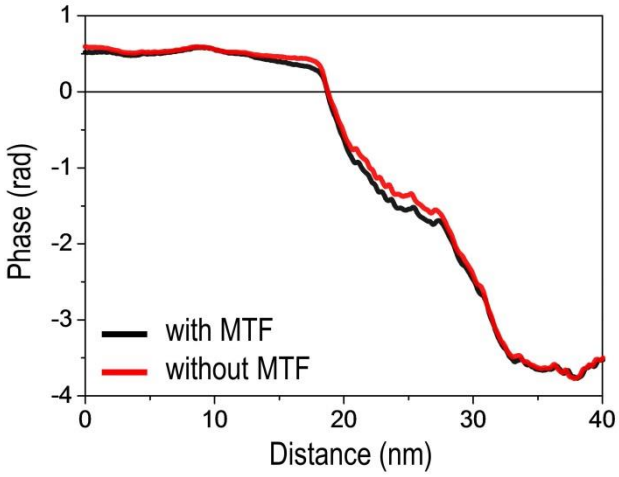

Figure 3. 2. Illustration of the effect on the phase profile of taking the MTF of the CCD camera into account. Reprinted from Ozsoy-Keskinbora et. al. [83] with permission from Nature Publishing Group, copyright 2014.

3.3. Results and Discussions

In order to allow experimental conditions optimized for off-axis holography to be applied also for the in-line holography experiment, several approaches are possible, two of which are illustrated in Figs. 3.1c and 3.1d. In Fig. 1c the electrostatic biprism is left within the path of the electron beam, but the image shift coils are used to shift the area of the sample that has previously been investigated by off-axis holography on the detector. Since the image shift required for this is directly proportional to the biprism voltage that has been applied for the off-axis experiment, this procedure can easily be implemented in a fully automated fashion. For the proof-of-principle experiments presented below first the biprism has been removed, and then mechanically shifted the specimen, so that the area of interest was again visible on the detector (Fig. 3.1d). Since our simulations have shown that the relative benefit of combining in-line and off-axis holography is independent of the illumination ellipticity (see Fig. 3.5i-k), ξ=1 was set in the experiments presented below.

Figure 3.3 shows an outline of the algorithm, illustrating the deterministic nature of linear off-axis electron holography reconstruction and the iterative nature of the refinement algorithm employed for in-line electron holography reconstruction. It is a general feature of most iterative in-line electron holography reconstruction algorithms that the very strongly encoded high-frequency details of the phase of the wavefunction are reconstructed first, before slowly varying features in the phase are recovered.[85] In the presence of noise and

residual inelastic scattering contributions to the experimental intensity measurements, the latter features may not be recovered at all. Fortunately, the refinement of experimental parameters and image registration is most sensitive to the accuracy with which high-frequency details have been estimated. It is therefore possible to first refine these details from a set of defocused images, using an empty phase map as a starting guess. During this process, the focal series can be aligned and the experimental parameters can be refined. The resulting estimate of the wavefunction can then simply be replaced with that recovered from an off-axis electron hologram and further refined by making it consistent with all in-line holograms. More specifically, the complete unwrapped phase and amplitude are imported separately, without applying any filtering for a specific frequency range. Since the iterative in-line reconstruction algorithm ensures that both the phase and the amplitude are consistent with the images in the focal series, the phase signal at low spatial frequencies is not affected significantly if only a few iterations are performed.[66] This procedure effectively extends the spatial resolution of the wavefunction obtained using off-axis electron holography, improves its signal to noise and removes the Fresnel fringes originating from the edges of the biprism.

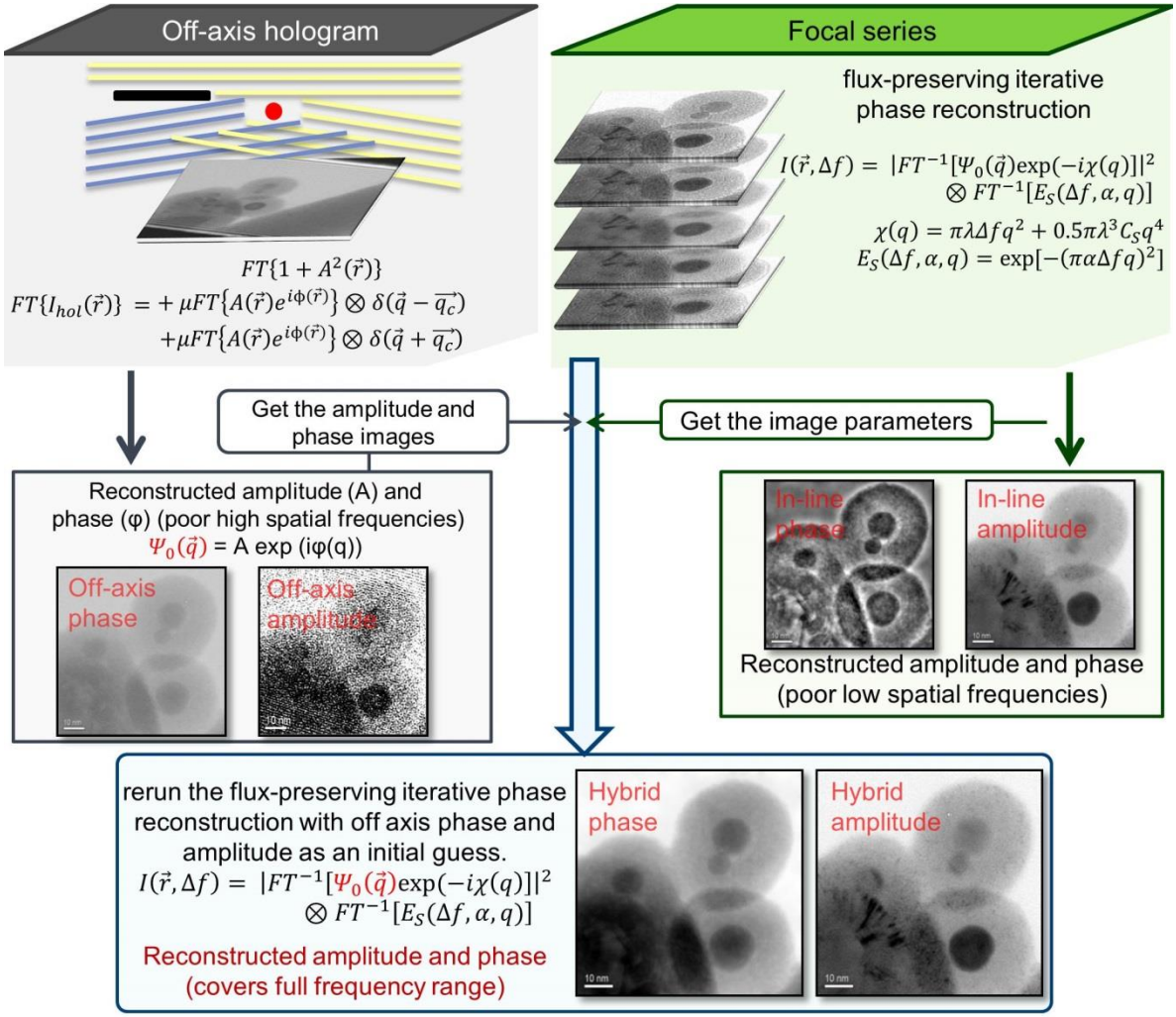

Figure 3. 3. Schematic outline of the wave reconstruction algorithm used in the present work. Reprinted from Ozsoy-Keskinbora et. al. [83] with permission from Nature Publishing Group, copyright 2014.

Figure 3.4 illustrates results obtained by applying both off-axis and in-line electron holography alone and the combined (hybrid) approach to a sample of iron-filled multi-walled carbon nano-onions.

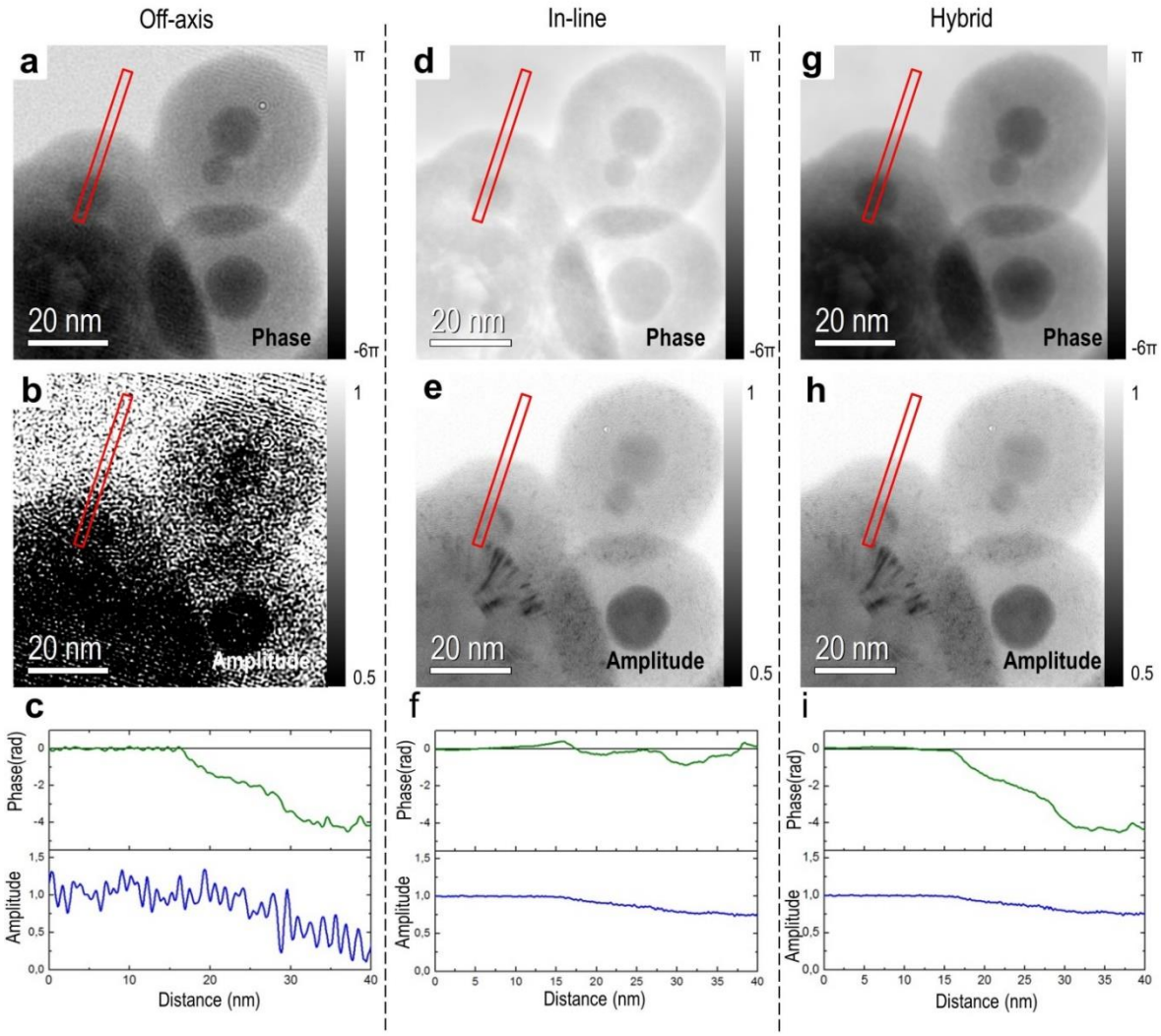

Figure 3. 4. Comparison of results obtained from a sample of iron-filled multi-walled carbon nano-onions using three methods: top row (a, d, g) amplitudes; middle row (b, e, h) phases; bottom row (c, f, i) amplitude and background-subtracted phase profiles; left column (a, b, c) off-axis holography method; middle column (d, e, f) in-line holography method; right column (g, h, i) hybrid holography method. Reprinted from Ozsoy-Keskinbora et. al. [83] with permission from Nature Publishing Group, copyright 2014.

The noise level in the wavefunction obtained using off-axis electron holography alone, which is much higher in both amplitude and phase (Figs. 3.4 a-c) than that obtained using either the in-line or the hybrid method, results in part from the fact that highly elliptical illumination (which is normally employed for off-axis electron holography but has only a very subtle effect on the signal-to-noise properties of in-line holograms) was not used in the present study. The application of in-line electron holography alone can be seen to reconstruct the amplitude well. However, ringing artifacts, which are not present in the off-axis reconstruction, are visible near sharp edges in the phase of the wavefunction

(Figs 3.4 d,f). The missing low spatial frequencies when using in-line electron holography can also be seen in a power spectrum generated from the reconstructed wavefunction (see below).[93,94] Figure 3.4 shows that, when the two methods are combined, the spatial frequencies that are missing from the in-line electron holography result are recovered, while the higher resolution of the in-line approach is retained. The amplitude image is also improved, including the elimination of biprism fringes inherent in the off-axis technique. These results are also supported by the reconstructions from simulated data shown in Figure 3.5. Due to the ability to directly compare the reconstructed phase images with the phase put into the simulations, the effectiveness of the hybrid approach can be verified in a very quantitative manner (see also Figs. 3.5i, 3.5k, and 3.5l). These simulations also allowed us to keep the electron dose exactly the same for all three techniques and easily test for the effect of changing the ellipticity of the illumination and verify that the hybrid approach presented here works very well at any (experimentally realizable) value of ξ. Moreover, it clearly shows that the signal-to-noise properties of the phase image recovered by the hybrid approach is superior to both off-axis and in-line holography, individually, assuming exactly the same electron dose in all three cases.

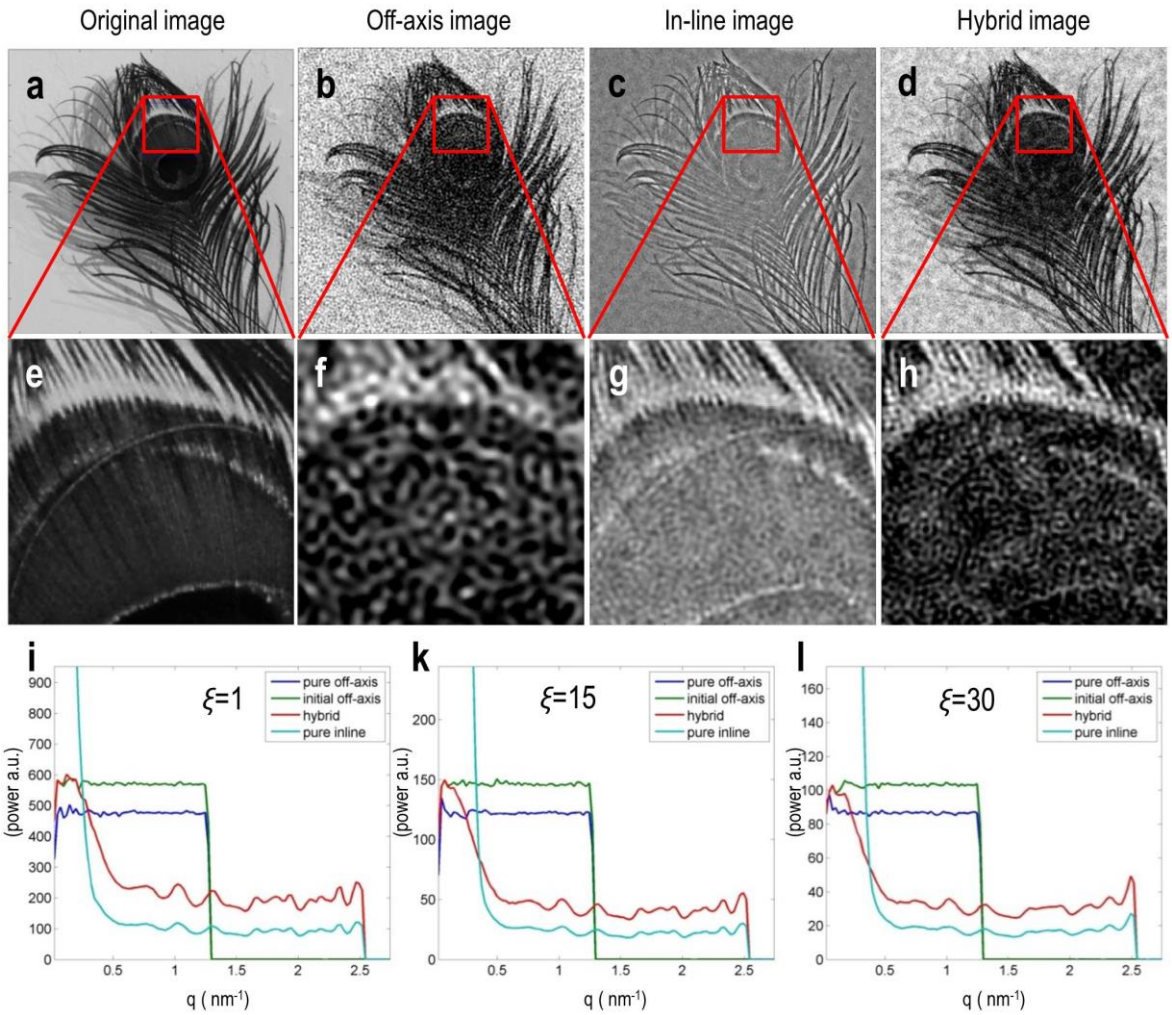

Figure 3. 5. Simulations: Comparison of noise and resolution of phase maps reconstructed from different simulated data sets with noise properties corresponding to equal total exposure times and electron doses. (a) The original, noise-free phase map ($0 \leq \phi(r) \leq 0.9$) used for simulating off-axis and in-line holograms. The red square indicates the area from which the figures (e) - (h) have been extracted, in each case from the phase map immediately above it. (b) Off-axis holography reconstruction for an exposure time of 0.4s, (c) In-line holography reconstruction from 7 equally long exposed images with a total exposure time of 0.4 s. (d) Hybrid (off-axis + in-line) reconstruction. Exposure time for the initial off-axis hologram: 0.1 s and for the complete focal series: 0.3 s. (i) Plot of the square root of the azimuthally averaged power spectrum of the difference between reconstruction and original, i.e. $\sqrt{\text{mean}\left(\left|\boldsymbol{FT}[\boldsymbol{\phi_{rec}} - \boldsymbol{\phi_{orig}}]\right|^2(\boldsymbol{q})\right)}$ for the cases (b), (c), and (d), as well as for the initial off-axis reconstruction used as a starting guess for the hybrid approach. The simulated data from which these reconstructions were done are shown in Fig. 3.6, along with a detailed description of the assumed acquisition parameters. (k) and (l), same as (i), but for elliptical illumination conditions**.** Reprinted from Ozsoy-Keskinbora et. al. [83] with permission from Nature Publishing Group, copyright 2014.*

* Simulation in Fig. 3.5 was carried out by Christoph T. Koch

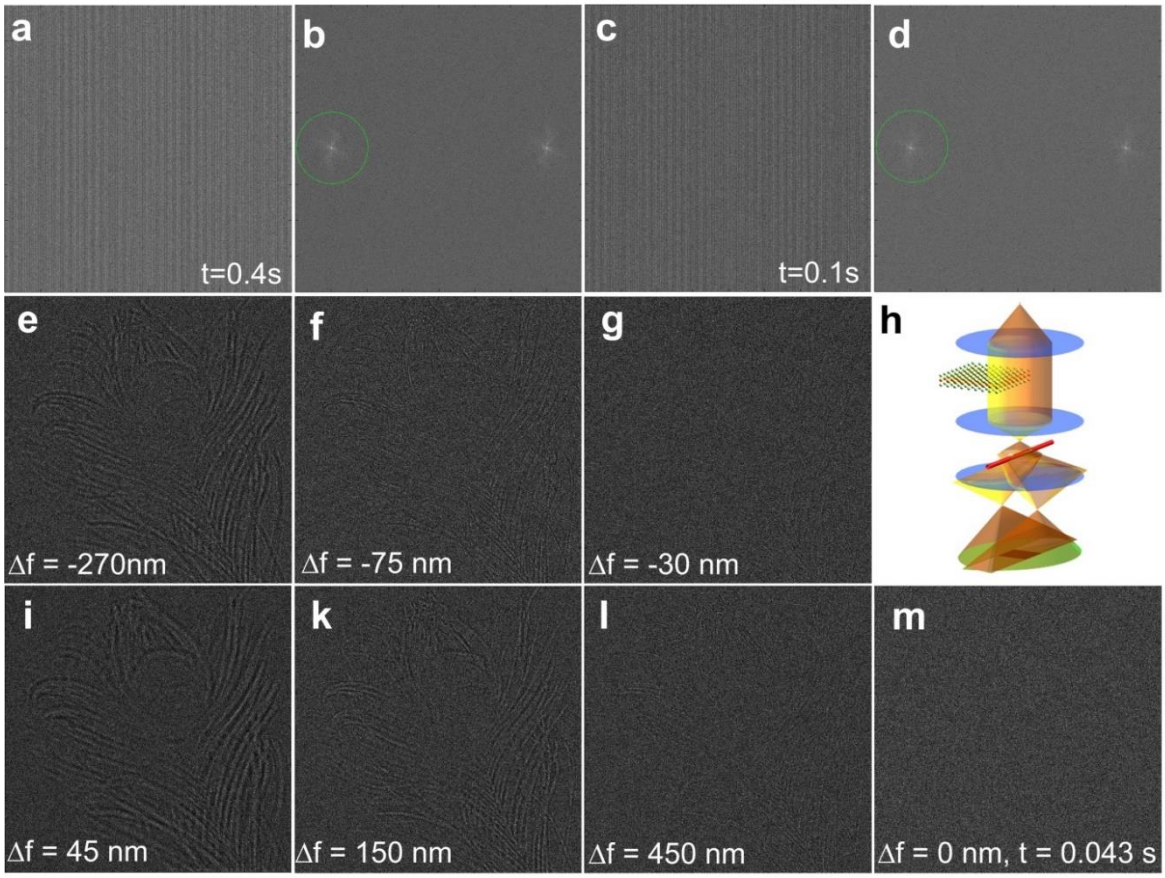

Figure 3. 6. The effect of exposure time: Simulated 80 kV off-axis and in-line holography data used to recover the phase images shown in Fig. 3.4. Poisson noise has been added in order to simulate the effect of finite exposure time. Round illumination (ξ=1), a source brightness of β = 2·108 $Acm^{-2}sr^{-1}$, a pixel size of 0.1 nm, and a field of view of 80 nm have been assumed. (a) Off-axis hologram simulated for an exposure time of 0.4 s. The shear distance x_{Shear} was equal to the field of view, and an optimized illumination semi-convergence angle of $\alpha = \lambda/(\sqrt{2}\,\pi x_{\mathrm{Shear}})$ = 11.7μrad was assumed [4]. Fresnel fringes due to the biprism have not been simulated. (b) Fourier transform of (a). (c) and (d) Off-axis hologram and fast Fourier transform (FFT) for an exposure time of 0.1 s. The green circles in (b) and (d) indicate the size and position of the numerical aperture used to reconstruct the wavefunction. (e), (f), (g), (i), (k), (l), and (m) show the in-line holograms simulated for the indicated planes of focus and exposure times of 0.043 s, adding up to a total of 0.3 s for the complete series. The illumination conditions were chosen identical to those used for the off-axis simulation. (h) Round illumination (ξ=1) and a high spatial coherence (the small ξ specified above) were assumed, in agreement with the experiment. Reprinted from Ozsoy-Keskinbora et. al. [83] with permission from Nature Publishing Group, copyright 2014.*

Moving now back to the experimental data, Figure 3.7 shows power spectra generated from the three sets of experimental results, which illustrate the deficiency in information transfer in the phase obtained using in-line electron holography (Fig. 3.7a) up to a spatial frequency of about 0.1 nm^{-1}. Figure 3.7b shows that the amplitudes reconstructed using the

* Simulation in Fig. 3.6 was carried out by Christoph T. Koch

in-line and hybrid methods are much less noisy than those reconstructed using off-axis electron holography (see also Fig. 3.8). The limited spatial resolution in the off-axis reconstruction is a result of an effective scattering angle limiting aperture applied during reconstruction. Using round, instead of elliptical illumination, the noise of the off-axis reconstruction is very high, despite an exposure time of 10 s. The experimental data confirms our simulations in that at lower spatial frequencies the reconstructed phase is much more reliable if it is obtained using off-axis electron holography, whereas at higher spatial frequencies in-line electron holography provides the same information but with much less noise. The power spectrum of the phase obtained using the hybrid method shows a good match to that from the off-axis reconstruction at lower spatial frequencies (up to ~ 0.2 nm^{-1}), while above this frequency it converges to the power spectrum obtained using in-line electron holography (Fig. 3.7 a,k).

Figure 3.7 (g-k) show how the low spatial frequency information that is missing in results obtained using in-line electron holography is recovered when using the hybrid approach. The horizontal and vertical lines in the power spectra are artifacts resulting from non-periodic boundaries of the images.

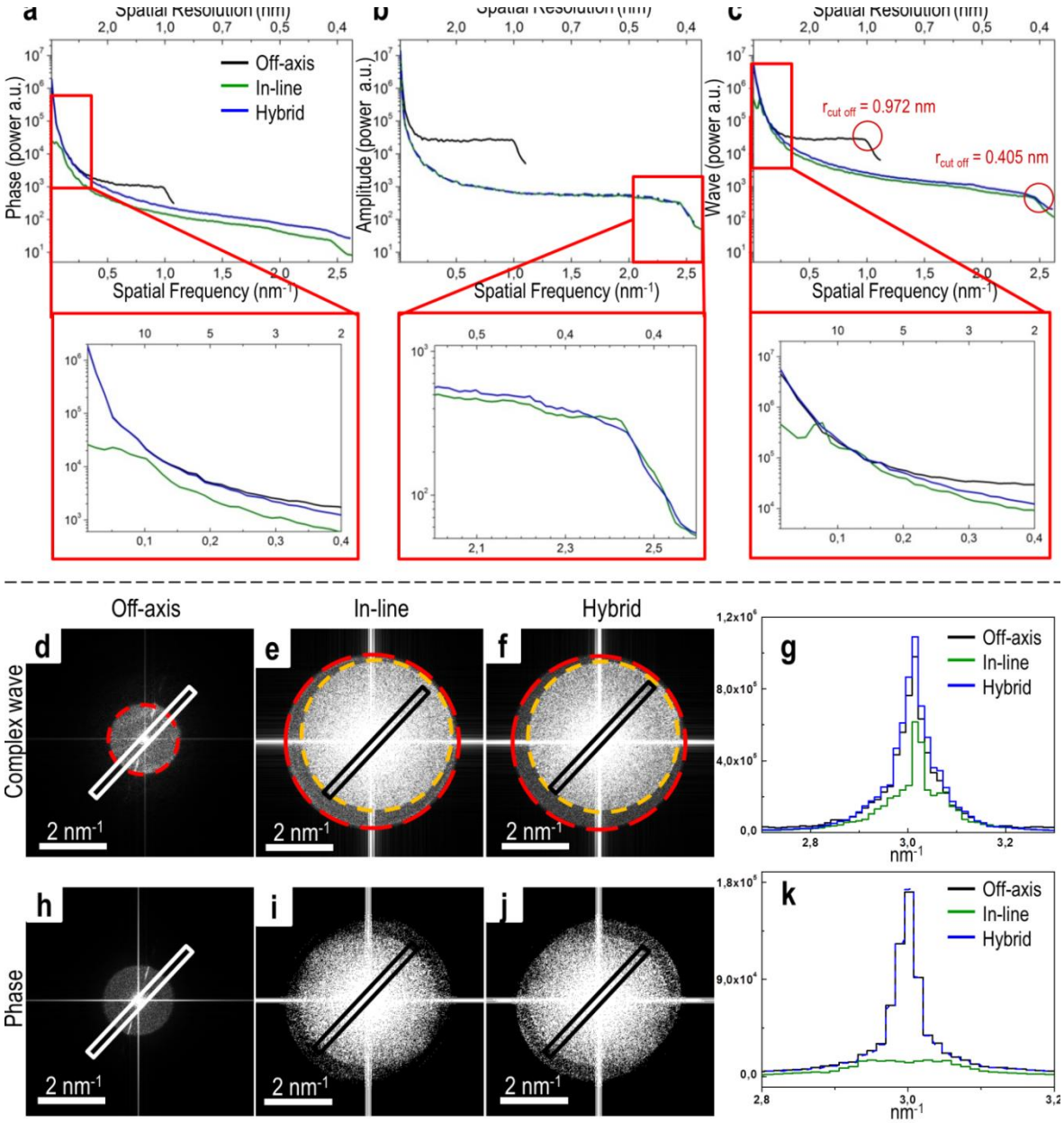

Figure 3. 7. Information transfer: The power spectrum of (a) phase, (b) amplitude and (c) complex wavefunction plotted as a function of spatial frequency for off-axis (black), in-line (green) and hybrid (blue) methods, with enlargements of selected regions shown below. The cut-off resolutions for the off-axis method (0.972 nm) and the in-line method (0.405 nm) are marked in (c). (d-f) show FFT of the complex wavefunction calculated for the (d) off-axis, (e) in-line and (f) hybrid methods. The shadow of the objective aperture used in the microscope is outlined in yellow in (e) and (f), while the red circle shows the cut-off frequency applied during reconstruction. (g) and (k) shows the intensity profile selected regions shown in (d-j). Reprinted from Ozsoy-Keskinbora et. al. [83] with permission from Nature Publishing Group, copyright 2014.

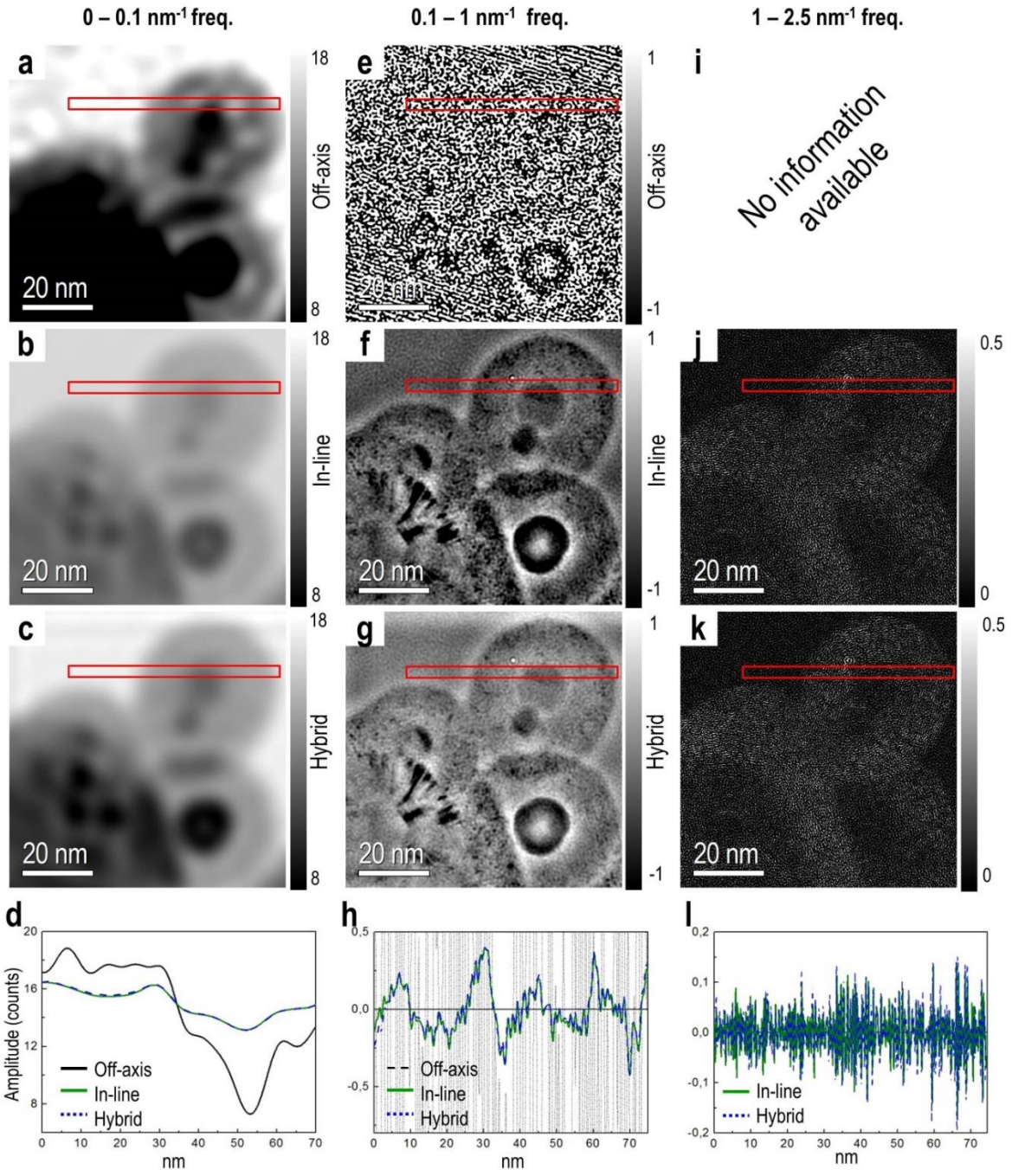

Figure 3. 8. Band-pass-filtered amplitude images for frequency ranges of (a, b, c) 0–0.1 nm^{-1}; (e, f, g) 0.1–1 nm^{-1}; (i, j, k) 1–2.5 nm^{-1}: Top row: off axis electron holography; middle row: in-line electron holography; bottom row: hybrid electron holography method. Line profiles generated from the boxes marked in red are shown in (d), (h) and (i). Reprinted from Ozsoy-Keskinbora et. al. [83] with permission from Nature Publishing Group, copyright 2014.

Power spectra generated from the complex wavefunction (Figs 3.7 d-f) demonstrate that, for the same field of view, the spatial resolution obtained using the in-line and hybrid methods is much better than that achieved using off-axis electron holography. In the

example shown here, the cut-off resolution (outlined by a dashed red circle) was set to 0.405 nm for the in-line and hybrid methods. This is slightly larger than the physical objective aperture, whose shadow (outlined by a dashed yellow circle) can be seen in Figures 3.7e and 3.7f. For the off-axis method, the resolution had to be limited to 0.972 nm by the numerical aperture size used during reconstruction. In addition to power spectrum analysis profiles extracted from the diffractogram also support the information loss in the in-line holography phase image, and how much of this has been recovered by the hybrid method (Figs. 3.7g and 3.7k). Although magnification and thus the absolute aperture sizes can be increased, this will also cause an increase in noise, and the resolution ratio of the two techniques will remain similar if the same number of detector pixels is used for both methods. There are two main advantages of combining the in-line and off-axis methods: an increase in spatial resolution and a decrease in noise over the full range of spatial frequencies. For off-axis holography, the interference fringe spacing limits the maximum numerical aperture size that can be chosen during reconstruction. For a given illumination ellipticity, source brightness and exposure time, the fringe spacing cannot be decreased without increasing the noise. For the in-line and hybrid methods, the physical objective aperture size can be increased up to the information limit. In Figure 3.9 and Table 3.1, a comparison of the reconstruction methods is presented for different frequency ranges of the phase images. A similar comparison is shown in Fig.3.8 for the amplitude images. In Figure 3.9, phase images filtered over three different spatial frequency ranges are shown for each of the three techniques, alongside profiles taken from areas marked by red boxes. The profiles illustrate the fact that the hybrid method matches the off-axis result at lower spatial frequencies (Figs 3.9 a-d) and the in-line result at higher spatial frequencies (Figs 3.9 e-h) and all show a good match in the intermediate frequency range (Figs 3.9 i-l). From Table 3.1, it is apparent that for full and medium spatial frequency ranges (0.1-1 nm^{-1}) the noise in the phase, estimated in the vacuum region where we expect the true phase to be flat, is approximately 4 times lower when using the hybrid method than for off-axis holography. The approximately 4 times lower noise in the phase presented in Table 3.1 confirms that the hybrid method has better noise properties than off-axis electron holography alone, promising an improvement in the reliability of quantitative holography-based experiments that are aimed at mapping electric and magnetic fields, charge distributions and strain.

Table 4. 1 Noise levels (standard deviations) of reconstructed phase and amplitude measured in the vacuum region. Reprinted from Ozsoy-Keskinbora et. al. [83] with permission from Nature Publishing Group, copyright 2014.

		Frequency range (nm^{-1})			
	Method	0-0.1	0.1-1	1-2.5	Full range
Phase (rad)	Off-axis	0.021	0.1	-	0.110
	In-line	0.006 (not reliable)	0.018	0.005	0.017 (not completely reliable)
	Hybrid	0.006	0.012	0.006	0.026
Amplitude	Off-axis	0.158	3.796	-	3.124
	In-line	0.008	0.069	0.096	0.114
	Hybrid	0.006	0.072	0.091	0.115

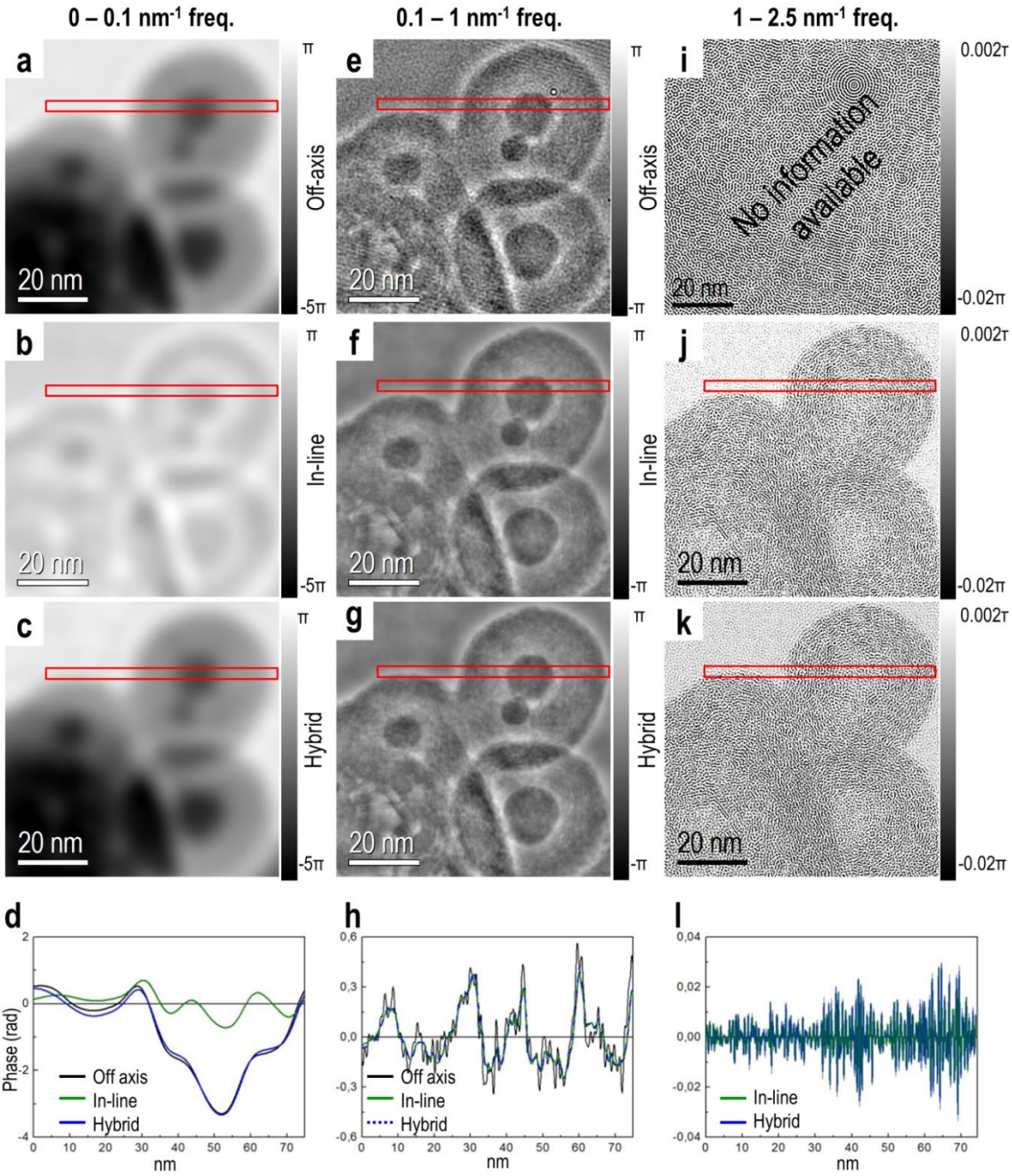

Figure 3. 9. Band-pass-filtered phase images determined for spatial frequency ranges of (a, b, c) 0–0.1 nm^{-1}, (e, f, g) 0.1–1 nm^{-1} and (i, j, k) 1–2.5 nm^{-1}: Top row: off-axis electron holography; middle row: in-line electron holography; bottom row: hybrid electron holography methods. Line profiles determined by projecting the intensity in the boxes marked in red are shown in (d), (h) and (i). Reprinted from Ozsoy-Keskinbora et. al. [83] with permission from Nature Publishing Group, copyright 2014.

In simulations, where the reconstruction can be directly compared with the expected result, this comparison is more straight forward, and the standard deviation of the power spectra of actual and reconstructed phases, as shown in Figs. 3.5i, 3.5k, and 3.5l can be also

quantified. The increase in spatial resolution and simultaneous decrease in noise, despite equal total exposure times becomes very obvious when comparing Figs. 3.5b (magnified in 3.5f) and 3.5d (magnified in 3.5h).

The mean inner potential of the specimen was obtained as a demonstration of the capability of the method by dividing the measured phase by the local specimen thickness (Fig. 3.10b), which was measured from an EFTEM thickness map, and by a wavelength-dependent electron-matter interaction constant. The mean inner potential at the edge of the specimen, which consists of carbon, is found to be close to the theoretical value found in the literature[95] [39]. The amplitude of the reconstructed wavefunction can also be used to obtain a thickness-independent[96] mean inner potential image, as shown in Fig. 3.11. The main error in determining the mean inner potential is the accuracy with which the local specimen thickness can be determined.

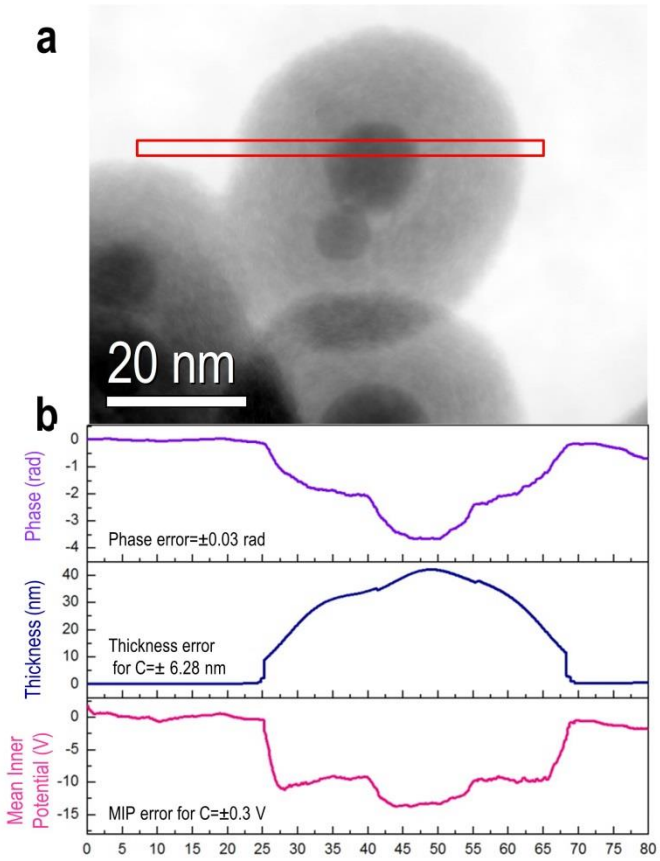

Figure 3. 10. Mean inner potential calculated from reconstructed phase image obtained using the hybrid method: (a) Original phase image; (b) phase, thickness and calculated mean inner potential profiles from the marked region shown in (a). Reprinted from Ozsoy-Keskinbora et. al. [83] with permission from Nature Publishing Group, copyright 2014.

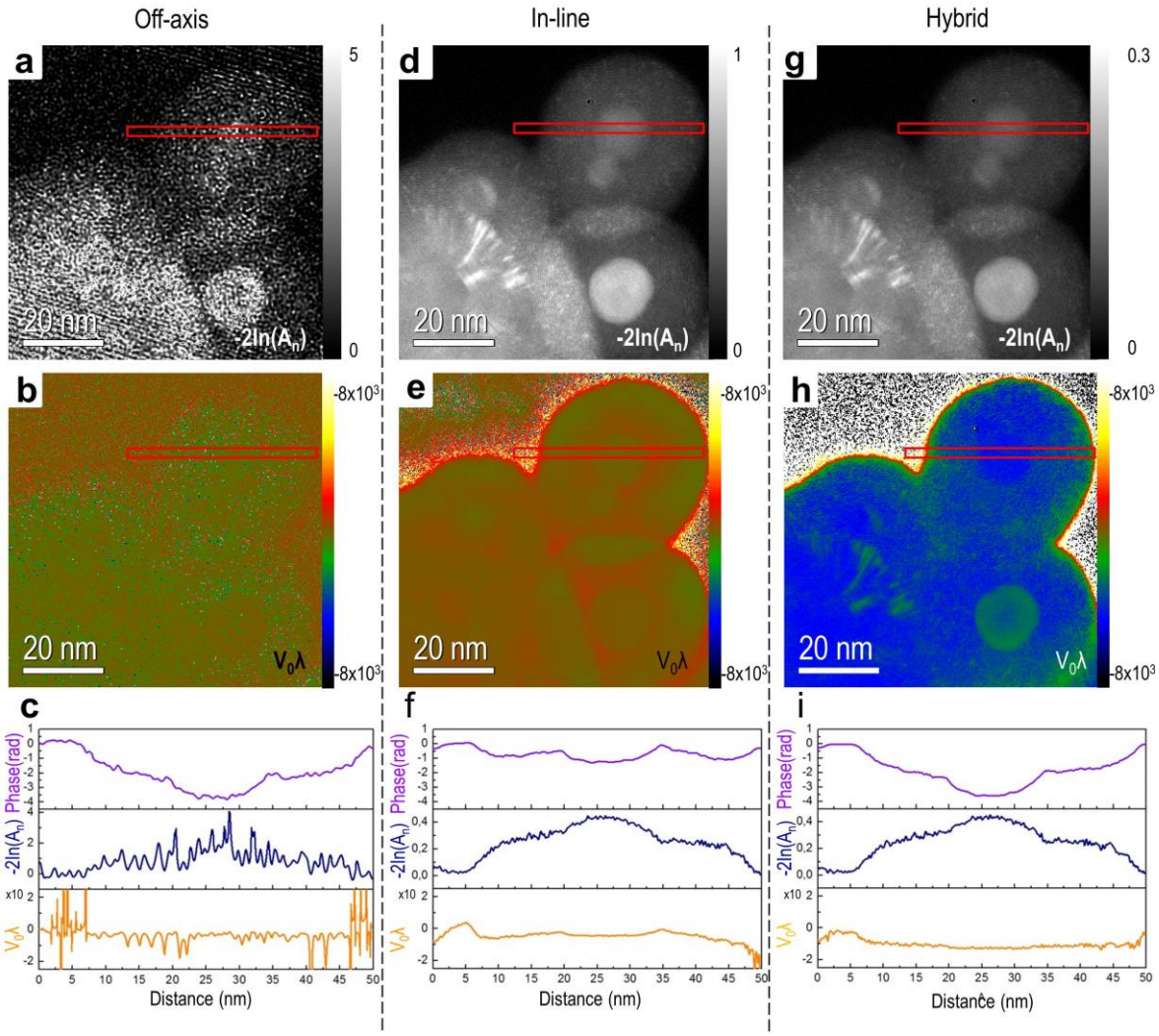

Figure 3. 11. Top row (a,d,g) -2ln(An)[96,97] calculated for the off-axis, in-line and hybrid methods. Middle raw (b,e,h): thickness-independent $V_0\lambda$[96,97]images calculated for the of off-axis, in-line and hybrid methods. Sections from the boxes marked in red are shown in (f). Reprinted from Ozsoy-Keskinbora et. al. [83] with permission from Nature Publishing Group, copyright 2014.

A further advantage of the hybrid method is its applicability to beam-sensitive specimens. Off-axis electron holography has high phase sensitivity at low spatial frequencies, requires a short exposure time and imparts a low total electron dose on the specimen since it is a single shot method. However, the exposure time needs to be increased to achieve high phase sensitivity at higher spatial resolution (Fig. 3.6 a-d). Focal series acquisition schemes can be optimized for electron-beam-sensitive samples by first acquiring images at small defocus values (for retrieving high spatial frequency information which suffers first from potential beam damage) and only then recording images with large defocus values[25,26] [22] (Fig.3.6 e-m). Partial spatial coherence of the illuminating electron beam results in strong

damping of the fine details of images recorded for large over- or under-focus, making these images comparatively insensitive to small structural changes produced by electron irradiation. In this way, the data ideally become increasingly insensitive to beam damage with increasing electron dose. In the hybrid method, both the off-axis exposure time and the number of images in the focal series can be decreased to reduce the electron dose. Although beam damage was not an issue in the present work, Fig. 3.12 shows that the hybrid method by including in-line holograms recorded at only 3 different planes of focus can recover the phase with very low noise and high spatial resolution. However, the recovery of the wavefunction from 13 images is better, as can be seen from the correct recovery of the shadow of the objective aperture in Figure 3.12f.

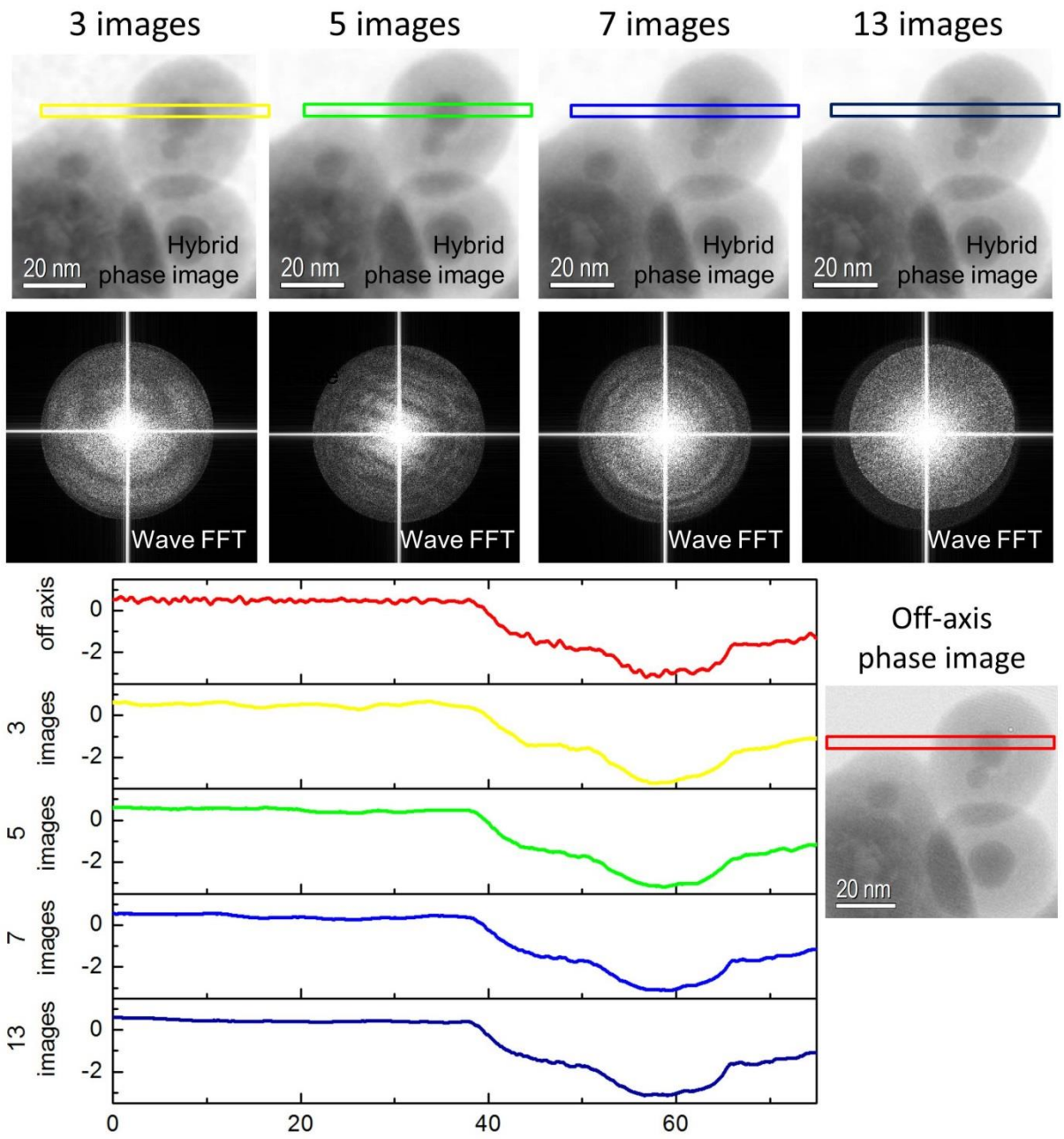

Figure 3. 12. Illustration of the effect of the number of defocus steps used for the reconstruction: Top row: phase images reconstructed using the different numbers of defocus images indicated. Middle row: Fourier transforms of the images in the top row. Bottom row: phase profiles obtained from the region marked in red in the off-axis phase image shown on the right. Reprinted from Ozsoy-Keskinbora et. al. [83] with permission from Nature Publishing Group, copyright 2014.

3.4. Conclusions

In summary, it has been demonstrated that the major weaknesses of in-line and off-axis electron holography can be overcome by combining the two techniques, resulting in a hybrid method that can be used to reconstruct a complex electron wavefunction with high spatial resolution and low noise over all of the spatial frequencies that are collected during the experiment, with relaxed experimental requirements for instrumental stability and interference fringe spacing. In the example presented here, a full spatial frequency range was achieved, providing an improvement over the absence of low spatial frequencies when using in-line holography alone. Even though the hybrid technique adds an additional step to the experimental procedure and may very slightly increase the noise at very low spatial frequencies when compared to off-axis electron holography alone, the total acquisition time uses the electron dose more efficiently to recover more of the wavefunction. The same overall phase sensitivity and noise level cannot be achieved using off-axis or in-line electron holography alone, given the same electron source brightness and exposure time. The efficient use of electron dose realized by the hybrid technique offers great potential for applications to biological materials and high-resolution studies.

4. Applications of Hybrid Electron Holography: High Resolution and Mean Inner Potential Measurements as an Example for Strong Phase Objects

4.1. Introduction

Colloidal metal nanoparticles have been used for millennia to color glass.[98,99] Different sizes of metal particles give rise to different surface plasmon resonances in the optical regime. Because of their unique properties and excellent stability,[100] gold nanoparticles (AuNPs) are among the most widely used and investigated metallic particles. Their noble-metal properties, high biocompatibility[101] and size and shape dependent electronic and optical properties[102] make AuNPs very good candidates for applications in catalysis,[103,104] transistor switches,[105] cancer research,[106,107] biosensing[108] and many other areas. In all of these applications, not only the sizes, shapes and structures of the nanoparticles, but also the presence of impurities and details of the electronic structure of both the bulk material and the nanoparticle surfaces are of high importance.

When investigating the atomic structures of nanoparticles, high-resolution TEM (HRTEM) is a widely applied method, in particular for the direct observation of surface structures, defects and interfaces,[109-111] for which methods such as X-ray and neutron diffraction lack spatial resolution and single atom sensitivity. Even though a single HRTEM image may already provide valuable information about the atomic arrangement in a given sample, the information that it contains is either missing the phase of the electron wave (in an aberration-corrected HRTEM image) or it contains delocalized information that is not directly interpretable (if the image is not aberration-corrected and/or defocused). In both cases, only part of the information about the electron wave that has passed through the specimen is measured and the available information is often difficult to interpret.[111] The imaging of an arrangement of atoms along a specific direction using electrons of a particular kinetic energy may produce many different images, depending on the aberrations of the imaging system. However, the complete complex-valued electron wave function at the exit face of the specimen is independent of the imaging conditions and may even contain information about the three-dimensional arrangement of the atoms that it has scattered

from.[112-114] Multiple images that have been recorded at different planes of focus in principle allow the exit wave function to be recovered.[115] The acquisition of a series of defocused images does not require any specialized equipment attached to an electron microscope. However, quantitative reconstruction requires a sophisticated computer algorithm to solve a large system of non-linear equations.

In off-axis electron holography, the attainable spatial resolution is limited by the fringe spacing, which is related to the biprism voltage and magnification. The fringe spacing should be no finer than ~ 3 times the pixel size of the detector. In-line and off-axis electron holography are highly complementary in their capabilities. While, on the one hand, off-axis electron holography can be used to recover all spatial frequencies with equal signal-to-noise properties, in-line electron holography is more efficient in recovering high spatial frequency components of the wave function, but is less sensitive to low spatial frequencies in the phase. Here, the applicability of hybrid electron holography approach,[83] which was introduced in Chapter 3, to atomic resolution electron holographic imaging is demonstrated. In addition to the very high spatial resolution and large field of view that are accessible using this technique, the hybrid electron holography scheme at intermediate resolution by varying the illumination direction with defocus slightly is extended. This approach results in excellent phase sensitivity at intermediate magnification for measuring the mean inner potential (MIP) of a AuNP, showing at the same time that this approach is also much less sensitive to dynamical diffraction effects than conventional off-axis electron holography.

4.2. Methods and Experimental Procedure

The in-line and off-axis electron holograms of Au nanoparticles suspended on a C grid using an FEI Titan 80-300 TEM equipped with two electron biprisms were collected. Round illumination was used for both in-line and off-axis electron holography, keeping the experimental setup as simple as possible. At intermediate magnification, an upper biprism voltage of 84.4 V was used for acquiring off-axis electron holograms. A focal series consisting of 13 images recorded at focal planes separated by 30 nm was acquired from the same area as the off-axis electron hologram. Along with the defocus, the beam tilt was changed in proportion to the defocus, spanning a tilt range of approximately 2 mrad between the first and the last image in the series. Both the off-axis and the in-line electron holograms were

energy-filtered using a 10 eV energy-selecting slit. For high-resolution off-axis electron holography, a bottom biprism voltage of 97.4 V was used and a 13-member focal series was acquired at 5 nm defocus steps. In contrast to the medium resolution experiment, high-resolution electron holography was carried out without using energy filtering and without introducing beam tilt. At magnifications allowing atomic resolution, the off-axis electron hologram were acquired using an exposure time of 3 s, while an exposure time of 1 s was used for each image in the focal series. At intermediate magnifications, off-axis electron holograms were acquired for 20 s while each image in the focal series was acquired using 1 s exposure time. All images were recorded on a 2048 x 2048 pixel CCD camera (Gatan, Inc.). For off-axis electron holography, the reference waves and line profiles of the interference fringe contrast are shown in Fig 4.1.

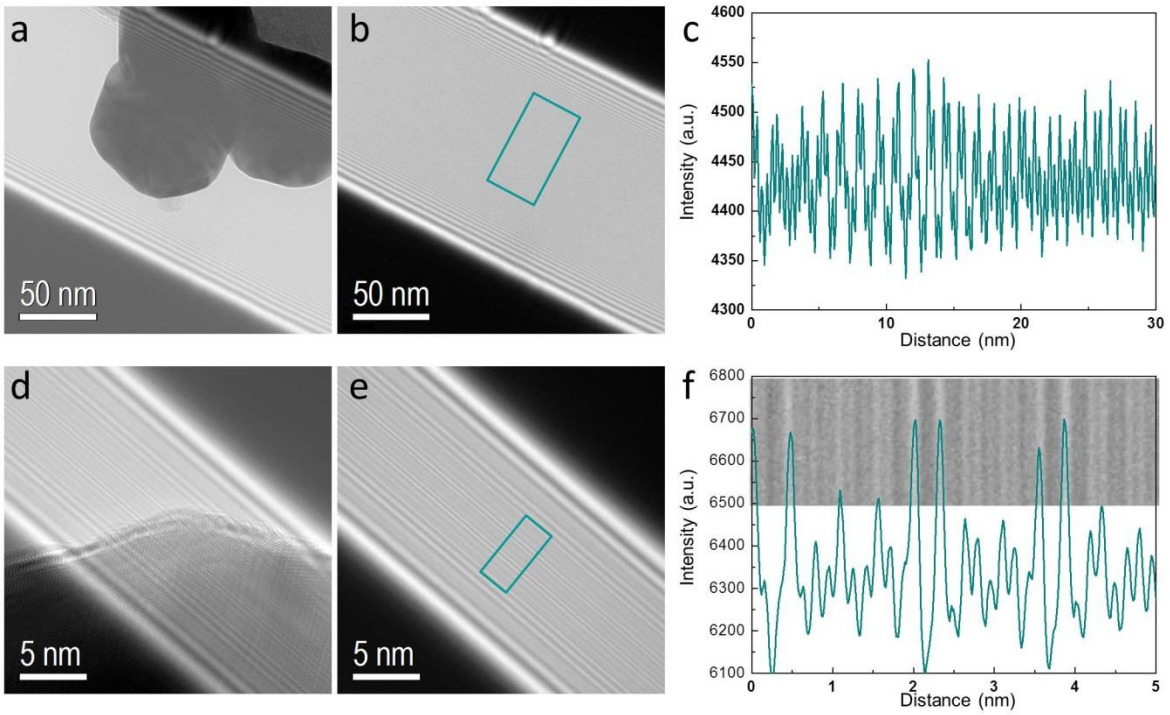

Figure 4. 1 1 a) Off-axis electron hologram; b) vacuum reference electron hologram; c) profile of fringe spacing at intermediate magnification; d) off-axis electron hologram; e) reference wave; f) profile of fringe spacing at atomic resolution. Reprinted from Ozsoy-Keskinbora et. al.[116] with permission from Elsevier, copyright 2016.

Reconstruction of in-line and hybrid electron holograms was performed using the flux-preserving wave reconstruction (FPWR),[25,26] which takes into account the modulation transfer function (MTF) of the CCD camera, partial spatial coherence and defocus-induced image distortions. Off-axis electron holograms were reconstructed using HolograFree[69]

software. The reconstructed phase and amplitude images were used for calculating the mean inner potential (MIP) according to the Eq. 2.7 and 2.8.[58] The value of C_E is 6.53 x 10^6 rad V^{-1} m^{-1} at an accelerating voltage of 300 kV.

The specimen thickness *t* was obtained from the reconstructed amplitude images using the expression[96]

$$t/\lambda_{in} = -2\ln A_o/A_r \qquad \text{Eq. 4. 1}$$

where A_o is the amplitude of the electron wave within the object and A_r is the mean amplitude within the vacuum area. The inelastic mean free path λ_{in} was calibrated (21.097 nm, for off-axis and 29.9 nm for hybrid electron holography, respectively) by ensuring that the inferred specimen thickness *t* was equal to the thickness reconstructed from a tomographic tilt series in the middle of the sample.

4.3. Results and Discussion

Reconstructed amplitude and phase images of the AuNPs, which were obtained at intermediate magnification using the three different electron holography methods (off-axis, in-line and hybrid electron holography), are shown in Fig. 4.2. Compared to the in-line electron holography phase image (Fig. 4.2b), which was reconstructed from 13 images, the hybrid electron holography approach, which combines information from both the off-axis electron hologram and the 13 defocused images, makes use of the low-spatial-frequency phase information in the off-axis electron hologram and thus recovers this contribution much better than in-line electron holography alone (Fig. 4.2c).

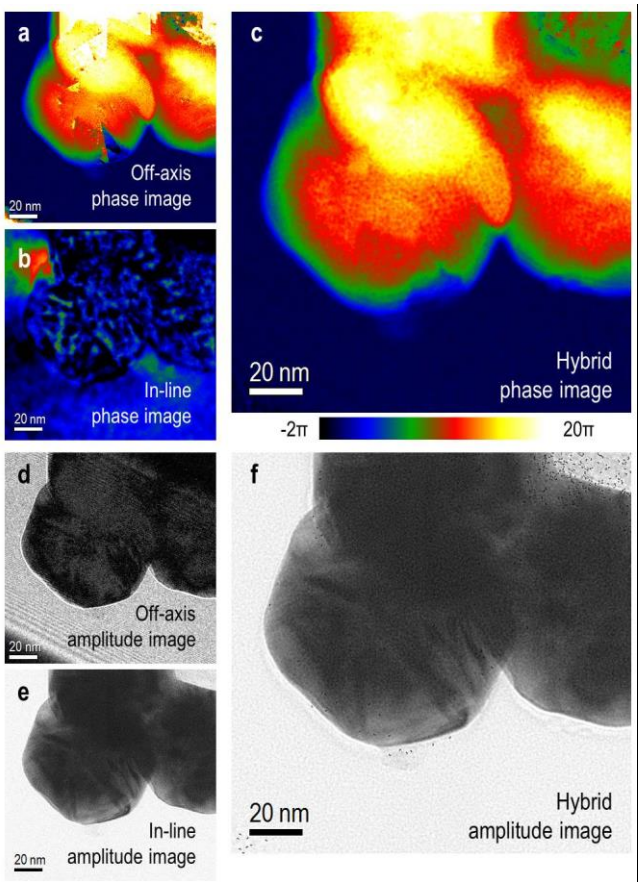

Figure 4. 2 (a, b, c) Phase and (d, e, f) amplitude of Au nanoparticles measured using off-axis, in-line and hybrid electron holography, respectively, at medium magnification. Reprinted from Ozsoy-Keskinbora et. al.[116] with permission from Elsevier, copyright 2016.

The noise levels in both the amplitude and the phase are also much lower in the hybrid electron holography reconstruction than in the reconstruction from the off-axis electron hologram. Moreover, the hybrid reconstruction does not contain biprism fringe and unwrapping artefacts which diminishes after the procedure presented in Fig 4.3), which are visible in the off-axis reconstruction (compare Figs 4.2 a, c, d, and f.).

Experimental measurements of the MIP of gold in the literature vary between 20 and 30 V,[117-119] while calculated values vary between ~ 25.0 and 35.9 V.[120,121] The MIP values that were obtained here are 23.16 ± 0.4 V from the off-axis electron hologram and 23.53 ± 0.12 V from hybrid electron holography when a sample thickness of 90 nm was assumed in the middle of the sample (see the selected are shown in Figs. 4.2 a and c). Figure 4.4b shows a line scan (the selected area shown in figure 4.4d of the MIP calculated from the reconstructed phase and amplitude images for both the hybrid and the off-axis approach, according to Eq. 2.7. Although the phase (Fig. 4.2 a) obtained using off-axis electron

holography agrees, on average, with that obtained using the hybrid electron holography, the amplitude recovered from the off-axis electron hologram alone shows a strong influence from dynamical diffraction. This leads to an apparent decrease in specimen thickness towards the center of the particle (see Fig. 4.4c). Each image in the focal series was acquired at a slightly different beam tilt (the total variation in beam tilt was ~2 mrad), yielding a slightly different dynamical diffraction condition. As the technique is designed to recover an electron wave function that best describes the intensity distribution in all of the images, the hybrid and in-line electron holography approaches effectively average over different dynamical diffraction conditions, reducing the influence of dynamical effects, resulting in more accurate amplitudes (Fig. 4.2 e,f) and thickness maps.

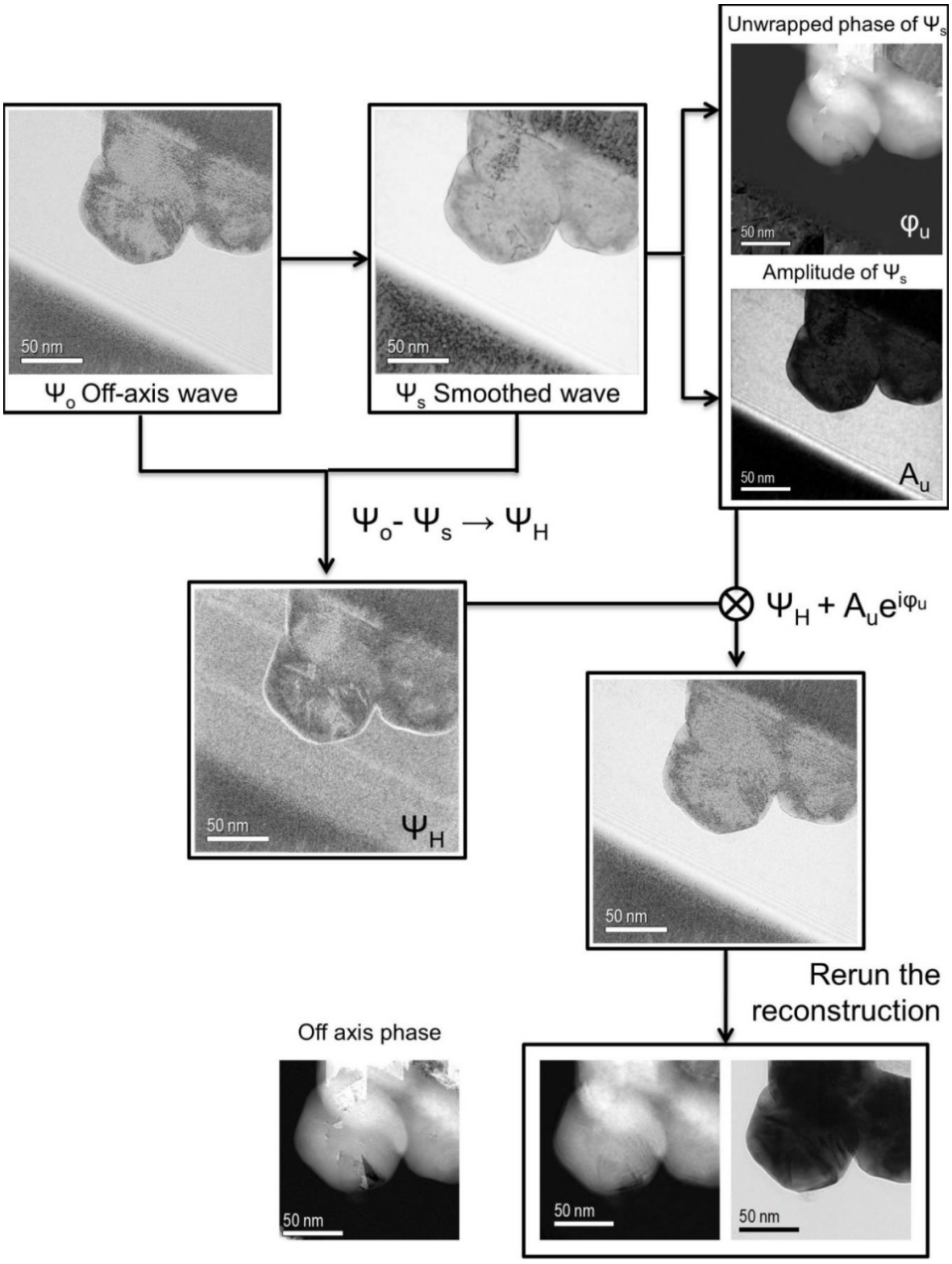

Figure 4. 3 Schematic view of the procedure used to reduce artifacts during phase unwrapping. First the wave function (ΨS) obtained by off-axis electron holography was smoothed using by changing the objective aperture with QSTEM.[122] Then, it was subtracted from the original wave image in order to obtain the high spatial frequency information (ΨH). Finally, (ΨS) and (ΨH) were summed and fed to the in-line/hybrid reconstruction algorithm. Reprinted from Ozsoy-Keskinbora et. al.[116] with permission from Elsevier, copyright 2016.

Figure 4.4b shows that the inferred variations in MIP are much greater from off-axis electron holography alone than using the hybrid approach. Apart from surface effects, the MIP recovered using hybrid electron holography is almost constant, as would be expected. Therefore, it is concluded that measuring the MIP of a strongly diffracting crystal using hybrid electron holography is more reliable than using off-axis electron holography alone.

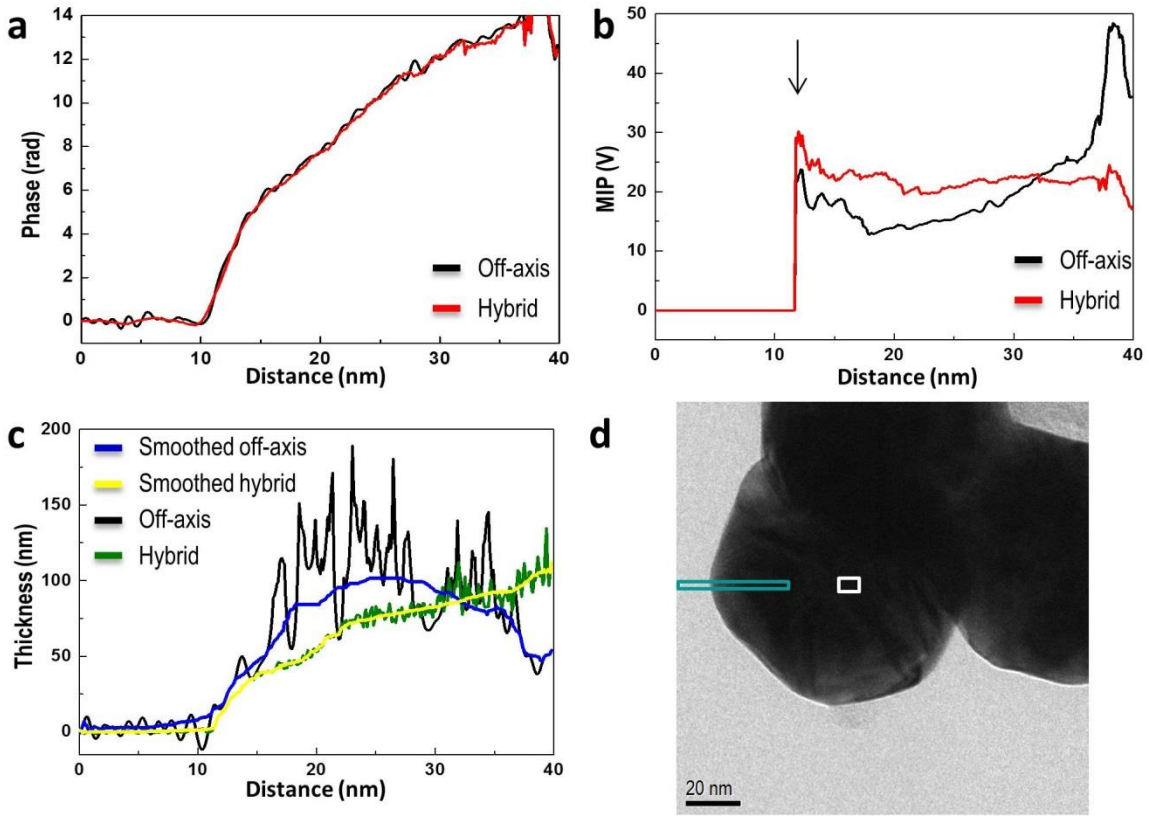

Figure 4. 4 a) Phase and b) MIP profiles obtained using off-axis and hybrid electron holography, respectively, from the region shown in d. The black arrow in b) indicates the edge of the specimen. To the left of the arrow there is vacuum. c) Specimen thickness profiles determined using the different techniques from the measured amplitude profiles. d) Bright-field image showing the areas from which the profiles were extracted. Reprinted from Ozsoy-Keskinbora et. al.[116] with permission from Elsevier, copyright 2016.

Figure 4.4b also shows an increase in the MIP within a range of ~ 5 nm from the particle surface. This increase was attributed to the surface tension.[117] One of the advantages of off-axis electron holography is that the reconstructed amplitude and phase represent exactly the wave function of elastically scattered electrons, i.e, all inelastically scattered electrons have been removed. It is therefore expected that the elimination of the inelastic signal causes the amplitude determined from the off-axis electron hologram to be lower than that determined using in-line electron holography.[123,124] Since in the in-line and hybrid electron

holography schemes inelastically scattered electrons can contribute to the recorded signal, their energy loss is lower than the cut-off energy loss defined by the energy-selecting slit.

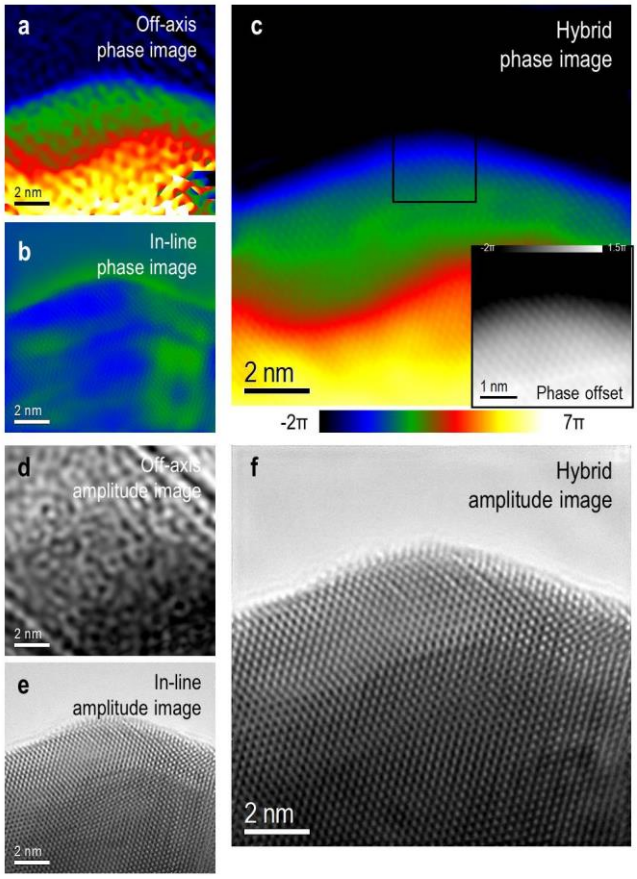

Figure 4. 5 (a, b, c) Phase and (d, e, f) amplitude measured using off-axis, in-line and hybrid electron holography, respectively, at atomic resolution. Reprinted from Ozsoy-Keskinbora et. al.[116] with permission from Elsevier, copyright 2016.

A significant advantage of hybrid electron holography over off-axis electron holography is its capability to record high-resolution electron holograms with a lower total electron dose and less stringent requirements on the experimental conditions, such as spatial coherence. The advantage of hybrid electron holography over pure in-line electron holography is that very low spatial frequencies in the phase are also recovered. Figure 4.5 demonstrates the capability of hybrid electron holography (see Fig 4.5 c, f) to recover both low and high spatial frequency information with atomic resolution by utilizing a focal series of 13 images, which can in principle be reduced to as few as 3 images (Fig. 4.6) for a reduced dose, although with less perfect results. The recording of exit wave functions at high spatial resolution using off-axis electron holography alone is a very challenging task for reasons that are discussed in

the literature,[38,125] mostly because of requirements for long exposure times, very high stability of the instrument and sensitivity of the experimental setup to vibrations and stray fields, requiring a superior microscope and working environment. The degree to which off-axis electron holography results are impacted by non-ideal experimental conditions can be seen in Fig. 4.5 a,d. In-line electron holography or focal series reconstruction is typically used when the main purpose of an experiment is to identify atomic positions, because accurate results at high spatial frequencies can be expected. However, variations in phase with characteristic spatial frequencies that are lower than the range of spatial frequencies that is reliably accessible using in-line electron holography cannot be quantified using this technique. This limitation in in-line electron holography becomes apparent in Figs. 4.2b and 3b, as the maximum phase shift expected from these materials is in the 10-15 π range for intermediate magnifications and 7π for atomicly resolved imaging when it is compared with more reliable off-axis values (Figs. 4.2a and 4.5a). However, the phase shift recovered from in-line electron holography is only ± 5π at intermediate magnifications and at atomic resolution only ± 1π. In contrast, the phase recovered using hybrid electron holography contains both low and high spatial frequencies. The atomic structure can then be correlated directly with long-range electromagnetic fields associated with it.

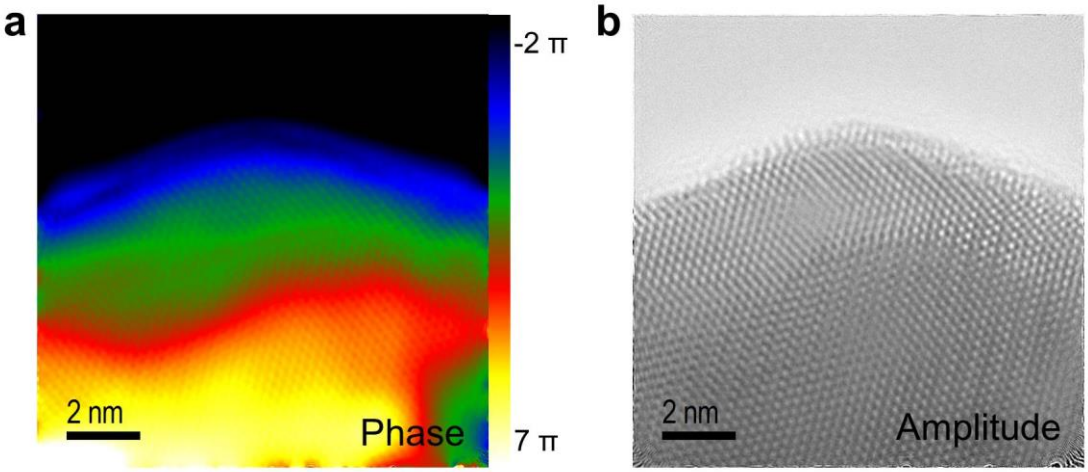

Figure 4. 6 a) Phase and b) amplitude images obtained using a hybrid electron holography reconstruction with 3 defocused images. Reprinted from Ozsoy-Keskinbora et. al.[116] with permission from Elsevier, copyright 2016.

4.4. Conclusions

The first application of hybrid electron holography at atomic resolution has been presented. The primary advantage of the combined approach, which was applied to Au nanoparticles, is the reliable reconstruction of the exit wave function with low noise across the complete range of spatial frequencies. Whereas atomic positions can be retrieved accurately from just the high spatial frequency components of the exit wave, the ability to record reliable measurements across the complete range of spatial frequencies becomes important for full quantification of, e.g., the relationship between structure and electrostatic or magnetic fields. This technique has also been applied at medium resolution, obtaining the mean inner potential of a Au nanoparticle and showing that varying the illumination direction with defocus reduces artifacts from dynamical scattering, in addition to yielding excellent signal-to-noise properties. Our measurements agree both with calculations[120,121] and with measurements reported using other techniques in the literature[117-119]. Both off-axis and hybrid electron holography show an increase in the measured MIP close to the edge of the specimen, as reported previously before by others.[117] It has been shown that feeding the in-line (focal series) reconstruction algorithm with off-axis data as an initial guess greatly enhances the result at low spatial frequencies, with only minimal noise added at high spatial frequencies when compared to a pure in-line holography reconstruction (Figs. 4.5 b,c,e,f).

5. Summary, Scientific Impact of the Present Study and Future Work

5.1. Summary

Focal series reconstruction or in-line electron holography is a common procedure in atomic resolution investigation for increased resolution, to eliminate the aberrations of the imaging system and to obtain quantitative information, especially because of the deficiencies of existing imaging systems. Although since 1990s higher order aberrations such as Cs, Cc, coma etc., [126,127] can be corrected, focal series reconstruction is still important, because aberration correction increases the information limit of microscopes, which in turn increases the achievable resolution with focal series reconstruction. Also, aberration correction or modifications proposes alternative possibilities to solve some problems in focal series reconstruction.[80]

In in-line electron holography the information transfer at high spatial frequencies is very efficient. As a matter of fact, it can reach the information limit of the microscope easily. However, the recovery of low spatial frequencies is limited, which becomes an even bigger problem at lower magnifications. Exploring alternative ways to recover the missing low spatial frequency information was the objective of this work. For this, two reconstruction approaches were developed.

Gradient-flipping assisted flux preserving in-inline reconstruction: The first method is the extension of the flux preserving algorithm with an applied modification that consists of flipping the gradient of the recovered phase where its absolute value is below a certain threshold, every few iterations. Such a procedure is known to favor solutions that are sparse in the domain where the flipping is applied. With the gradient-flipping assisted flux-preserving in-line reconstruction, the missing low spatial frequency information was decreased from 80 percent down to 40 - 50 percent. The main advantage was the disappearance of artifacts at the interfaces due to the missing frequencies.

Hybrid electron holography: The second approach was the hybridization of the two complementary electron holography approaches, off-axis and in-line electron holography. This method brings together the strong points of each method and provides better phase

sensitivity and resolution over the whole spatial frequency range compared to the individual methods. The off axis-electron holography provides very powerful working conditions at lower magnification for mapping electrical and magnetic fields, mean inner potentials, strain etc., while in-line electron holography struggles in recovering the low spatial frequencies. In contrast, in the high spatial frequency regime, the phase sensitivity performance of in-line electron holography is much more efficient due to a better signal to noise ratio and higher resolution capability.

The flux preserving non-linear in-line reconstruction algorithm is an iterative method that starts with a random phase guess. Using the off-axis electron holography phase as an initial guess provides the necessary low spatial frequency information and in the frequency regime where the signal to noise ratio performance of off-axis electron holography is lower, the information is provided by the in-line electron holography. By using the hybrid electron holography approach the off-axis phase resolution can be improved by ~ 60 % and the noise level decreased by ~ 75% in the phase. This value can reach even ~ 95 % for amplitude noise. Furthermore, in contrast to in-line electron, holography, hybrid electron holography recovers the whole frequency range with very similar precision, hence it makes quantitative analysis possible with a high level of accuracy.

5.2. Scientific Impact of the Present Study

The fully quantitative in-line electron holography reconstruction for strong phase objects, especially at lower magnifications, does not seem possible with the existing methods. However, even though gradient flipping assisted wave reconstruction couldn't deliver fully quantitative phase recovery, it is able to reconstruct the phase information without creating extra features (artifacts) at large phase change regions with subtracted phase information. This makes in-line electron holography a more useful method where quantification is not so critical, but where qualitatively reliable information is necessary. It is applicable in all kinds of field emission gun transmission electron microscopes also at low magnification investigations.

Hybrid electron holography promises better phase resolution, sensitivity and quantifiability than off-axis and in-line electron holography individually. So, this method can be used to answer demanding questions in low dimensional materials, which require very

high precision and accuracy. Also, it allows efficient use of dosage and this makes hybrid electron holography a good candidate for phase reconstruction of beam sensitive materials. Furthermore, hybridization of the two methods is not only limited to the electron imaging but is applicable also to other wave imaging methods, using for instance, photons from optical to X-ray energies. This method can find applications in X-ray microscopy, medical imaging using both X-rays and ultrasound etc.

5.3. Future Work

As a continuation of this thesis work, I would like to propose some examples including some preliminary result. As mentioned before, the initial objective of this dissertation was mapping the 2 DEG in Bi_2Se_3, but due to the limitations of existing characterization methods this purpose could not be achieved. To be able to overcome these limitations, the two alternative methods are proposed in the thesis.

Figure 6.1 shows the phase and amplitude images of Bi_2Se_3 by using the hybrid electron holography approach. The cut-off resolution of the images were calculated as ~ 0.5 nm. As can be seen from the figure, the sensitivity and resolution of the phase image, is high enough to resolve the localization on the phase shift of the c-lattice fringes, with lattice distances of 2.86 nm.

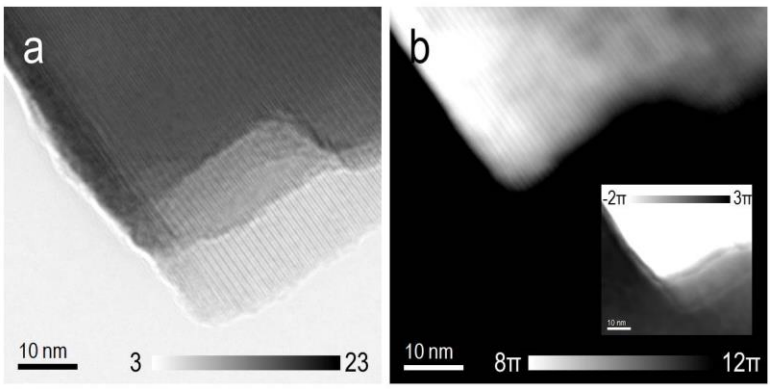

Figure 5. 1 a) Amplitude and b) phase image of Bi_2Se_3 using hybrid electron holography.

The two images represented in Fig. 6.1 b are identical images with different phase offsets, which are used to show the whole image phase range due to high phase differences.

When both amplitude and phase images in Fig. 6.1 are compared with the results of Fe-C core-shell particles shown in Fig. 3.4 g and h., Fig. 6.1 a and b are relatively blurred and have some artifacts at the edges. This causes problems in quantitative analysis for this sample system due to the possibility of the localization of 2DEG at the edge of the specimen.

The FEI Titan 80–300 TEM, equipped with a field emission gun, utilized for the hybrid electron holography of the Bi_2Se_3 specimens produces a beam of very high coherence. Therefore, layered structure of Bi_2Se_3 creates very strong Fresnel fringes at the edges, which in turn complicates the image registration processes. This problem is more convoluted with the fact that the Fresnel fringes are aligned parallel to the lattice fringes of the specimen. The reason of the blurriness and the artifact at the surface, where Fresnel and lattice fringes align parallel to each other, can be attributed to superposition of the lattice fringes with Fresnel fringes which affects the reconstruction.

In addition to Bi_2Se_3, LAO/STO which is an important materials system for high temperature super conductivity and quite challenging system for electron holography experiment was carried out. In both materials system the observation of 2DEG position in the materials, will give important information to answer fundamental questions.

Table of Figures

Chapter 1

Chapter 2

Chapter 3

Chapter 4

Chapter 5

Abbreviations

ARPES	Angle Resolved Photoemission Spectroscopy
AuNPs	Gold NanoParticles
BF	Bright Field
CCD	Charged Couple Device
CTF	Coherent Transfer Function
EFTEM	Energy Filtered Transmission Electron Microscopy
FPWR	Flux Preserving Wave Reconstruction
FFT	Fast Fourier Transform
GF-FPWR	Gradient-Flipping assisted Flux Preserving Wave Reconstruction
HRTEM	High Resolution Transmission Electron Microscopy
IMP	Inelastic Mean Free Path
MAL	Maximum Likelihood
MIP	Mean Inner Potential
MTF	Modulation Transfer Function
POA	Phase Object Approximation
SESAM	Sub Electron Volt Sub Angstrom Microscope
TF	Transfer Function
TEM	Transmission Electron Microscope
TIE	Transport Intensity Equation
Tis	Topological Insulators
WPOA	The weak phase object approximation
2DEG	Two Dimensional Electron Gas
3D-FFM	Three Dimensional Fourier Filtering Method

References

1. Xia, Y.; Qian, D.; Hsieh, D.; Wray, L.; Pal, A.; Lin, H.; Bansil, A.; Grauer, D.; Hor, Y. S.; Cava, R. J.; Hasan, M. Z. Observation of a large-gap topological-insulator class with a single Dirac cone on the surface. *Nature Physics* 2009, 5, 398-402.

2. Bianchi, M.; Guan, D.; Bao, S.; Mi, J.; Iversen, B. B.; King, P. D. C.; Hofmann, P. Coexistence of the topological state and a two-dimensional electron gas on the surface of Bi2Se3. *Nat Commun* 2010, 1.

3. Gabor, D. A New Microscopic Principle. *Nature* 1948, 161, 777-778.

4. Hariharan, P. Optical Holography: Principles, Techniques, and Applications. *Optical Engineering* 1997, 36, 1267-1267.

5. Midgley, P. A. An introduction to off-axis electron holography. *Micron* 2001, 32, 167-184.

6. Hayek, S. Nearfield Acoustical Holography. In *Handbook of Signal Processing in Acoustics*, Havelock, D.; Kuwano, S.; Vorländer, M., Eds. Springer New York: 2008; pp 1129-1139.

7. Charles, L.; Braun, D. C. Principles of Seismic Holography for Diagnostics of the Shallow Subphotosphere. *The Astrophysical Journal Supplement Series* 2004, 155, 209.

8. Rau, W. D.; Schwander, P.; Baumann, F. H.; Höppner, W.; Ourmazd, A. Two-Dimensional Mapping of the Electrostatic Potential in Transistors by Electron Holography. *Physical Review Letters* 1999, 82, 2614-2617.

9. Han, M.-G.; Marshall, M. S. J.; Wu, L.; Schofield, M. A.; Aoki, T.; Twesten, R.; Hoffman, J.; Walker, F. J.; Ahn, C. H.; Zhu, Y. Interface-induced nonswitchable domains in ferroelectric thin films. *Nat Commun* 2014, 5.

10. He, K.; Ma, F.-X.; Xu, C.-Y.; Cumings, J. Mapping magnetic fields of Fe3O4 nanosphere assemblies by electron holography. *Journal of Applied Physics* 2013, 113, 17B528-17B528-3.

11. Hÿtch, M.; Houdellier, F.; Hüe, F.; Snoeck, E. Nanoscale holographic interferometry for strain measurements in electronic devices. *Nature* 2008, 453, 1086-1089.

12. Koch, C. T.; Özdöl, V. B.; van Aken, P. A. An efficient, simple, and precise way to map strain with nanometer resolution in semiconductor devices. *Applied Physics Letters* 2010, 96, 091901-091901-3.

13. Twitchett-Harrison, A. C.; Yates, T. J. V.; Newcomb, S. B.; Dunin-Borkowski, R. E.; Midgley, P. A. High-Resolution Three-Dimensional Mapping of Semiconductor Dopant Potentials. *Nano Letters* 2007, 7, 2020-2023.

14. Maxwell, J. C. A Dynamical Theory of the Electromagnetic Field. *Philosophical Transactions of the Royal Society of London* 1865, 155, 459-512.

15. Einstein, A. Über einen die Erzeugung und Verwandlung des Lichtes betreffenden heuristischen Gesichtspunkt. *Annalen der Physik* 1905, 322, 132-148.

16. Lewis, G. N. The Conservation of Photons. *Nature* 1926 118, 874-875

17. Knoll, M.; Ruska, E. Beitrag zur geometrischen Elektronenoptik. I. *Annalen der Physik* 1932, 404, 607-640.

18. Knoll, M.; Ruska, E. Beitrag zur geometrischen Elektronenoptik. II. *Annalen der Physik* 1932, 404, 641-661.

19. Abbe, E. Beitrage zur Theorie des Mikroskops und der Mikroskopischen Wahrnehmung. *Arch. Mikrosk. Anat* 1873, 9, 413-468.

20. Ruska, E. The Development of the Electron Microscope and of Electron Microscopy (Nobel Lecture). *Angewandte Chemie International Edition in English* 1987, 26, 595-605.

21. Möllenstedt, G.; Düker, H. Fresnelscher Interferenzversuch mit einem Biprisma für Elektronenwellen. *Die Naturwissenschaften* 1955, 42, 41-41.

22. Gerchberg, R. W.; Saxton, O. A practical algorithm for the determination of the phase from image and diffraction plane pictures. *Optik* 1972, 35, 237-246.

23. Wanner, M.; Bach, D.; Gerthsen, D.; Werner, R.; Tesche, B. Electron holography of thin amorphous carbon films: measurement of the mean inner potential and a thickness-independent phase shift. *Ultramicroscopy* 2006, 106, 341-5.

24. Wright, D. A. Thermoelectric Properties of Bismuth Telluride and its Alloys. *Nature* 1958, 181, 834-834.

25. Koch, C. T. A flux-preserving non-linear inline holography reconstruction algorithm for partially coherent electrons. *Ultramicroscopy* 2008, 108, 141-50.

26. Koch, C. T. Towards full-resolution inline electron holography. *Micron*.

27. Thomson, J. J. XL. Cathode Rays. *Philosophical Magazine Series 5* 1897, 44, 293-316.

28. Williams, D. B.; Carter, C. B. *Transmission Electron Microscopy: A Textbook for Materials Science. Diffraction. II*. Springer: 1996.

29. Egerton, R. F. *Electron Energy-Loss Spectroscopy in the Electron Microscope*. Springer: 1996; p 506.

30. Goodhew, P. J.; Humphreys, J.; Beanland, R. *Electron Microscopy and Analysis, Third Edition*. Taylor & Francis: 2000.

31. Shindo, D.; Oikawa, T. *Analytical Electron Microscopy for Materials Science*. Springer Japan: 2013.

32. Fultz, B.; Howe, J. M. *Transmission Electron Microscopy and Diffractometry of Materials: With Numerous Exercises*. Springer: 2002.

33. Völkl, E.; Allard, L. F.; Joy, D. C. *Introduction to Electron Holography*. Kluwer Academic/Plenum Publishers: 1999.

34. Kirkland, A.; Hutchison, J.; Chemistry, R. S. o. *Nanocharacterisation*. RSC Publishing: 2007.

35. Cowley, J. M. Twenty forms of electron holography. *Ultramicroscopy* 1992, 41, 335-348.

36. McCartney, M. R.; Smith, D. J. Electron Holography: Phase Imaging with Nanometer Resolution. *Annual Review of Materials Research* 2007, 37, 729-767.

37. Lichte, H.; Lehmann, M. Electron holography—basics and applications. *Reports on Progress in Physics* 2008, 71, 016102.

38. Lichte, H.; Formanek, P.; Lenk, A.; Linck, M.; Matzeck, C.; Lehmann, M.; Simon, P. Electron Holography: Applications to Materials Questions. *Annual Review of Materials Research* 2007, 37, 539-588.

39. Reed Teague, M. Deterministic phase retrieval: a Green?s function solution. *Journal of the Optical Society of America* 1983, 73, 1434-1441.

40. Kirkland, J. *Advanced Computing in Electron Microscopy*. Springer US: 2013.

41. Coene, W. M. J.; Thust, A.; Op de Beeck, M.; Van Dyck, D. Maximum-likelihood method for focus-variation image reconstruction in high resolution transmission electron microscopy. *Ultramicroscopy* 1996, 64, 109-135.

42. Nomaguchi, T.; Kawasaki, T.; Kimura, Y.; Takai, Y. Separation of linear and non-linear imaging components in high-resolution transmission electron microscope images. *Journal of Electron Microscopy* 2004, 53, 403-406.

43. Op de Beeck, M.; Van Dyck, D.; Coene, W. Wave function reconstruction in HRTEM: the parabola method. *Ultramicroscopy* 1996, 64, 167-183.

44. Kawasaki, T.; Takai, Y.; Ikuta, T.; Shimizu, R. Wave field restoration using three-dimensional Fourier filtering method. *Ultramicroscopy* 2001, 90, 47-59.

45. Kübel, C.; Thust, A. TrueImage. In *Electron Crystallography*, Springer: 2006; pp 373-392.

46. Kirkland, E. J. Nonlinear high resolution image processing of conventional transmission electron micrographs: I. Theory. *Ultramicroscopy* 1982, 9, 45-64.

47. Teague, M. R. DETERMINISTIC PHASE RETRIEVAL: A GREEN'S FUNCTION SOLUTION. *Journal of the Optical Society of America* 1983, 73, 1434-1441.

48. Ishizuka, K.; Allman, B. Phase measurement of atomic resolution image using transport of intensity equation. *Journal of Electron Microscopy* 2005, 54, 191-197.

49. Bonevich, J. E.; Marks, L. D. Contrast transfer theory for non-linear imaging. *Ultramicroscopy* 1988, 26, 313-319.

50. Koch, C. T.; Lubk, A. Off-axis and inline electron holography: A quantitative comparison. *Ultramicroscopy* 2010, 110, 460-471.

51. Latychevskaia, T.; Formanek, P.; Koch, C. T.; Lubk, A. Off-axis and inline electron holography: Experimental comparison. *Ultramicroscopy* 2010, 110, 472-482.

52. Scherzer, O. The Theoretical Resolution Limit of the Electron Microscope. *Journal of Applied Physics* 1949, 20, 20-29.

53. Hasan, M. Z.; Kane, C. L. Colloquium: Topological insulators. *Reviews of Modern Physics* 2010, 82, 3045-3067.

54. Moore, J. Topological insulators: The next generation. *Nat Phys* 2009, 5, 378-380.

55. Moore, J. E. The birth of topological insulators. *Nature* 2010, 464, 194-198.

56. Zhang, H.; Liu, C.-X.; Qi, X.-L.; Dai, X.; Fang, Z.; Zhang, S.-C. Topological insulators in Bi2Se3, Bi2Te3 and Sb2Te3 with a single Dirac cone on the surface. *Nat Phys* 2009, 5, 438-442.

57. Zhang, Y.; He, K.; Chang, C.-Z.; Song, C.-L.; Wang, L.-L.; Chen, X.; Jia, J.-F.; Fang, Z.; Dai, X.; Shan, W.-Y.; Shen, S.-Q.; Niu, Q.; Qi, X.-L.; Zhang, S.-C.; Ma, X.-C.; Xue, Q.-K. Crossover of the three-dimensional topological insulator Bi2Se3 to the two-dimensional limit. *Nat Phys* 2010, 6, 584-588.

58. Spence, J. C. H. *Experimental High-Resolution Electron Microscopy*. 2 ed.; Oxford University Press, USA: 1988; p 448.

59. Introduction to Electrodynamics (3rd Edition): David J. Griffiths: 9780138053260: Amazon.com: Books. http://www.amazon.com/Introduction-Electrodynamics-Edition-David-Griffiths/dp/013805326X.

60. Duffar, T.; Sylla, L. Vertical Bridgman Technique and Dewetting. In *Crystal Growth Processes Based on Capillarity*, John Wiley & Sons, Ltd: 2010; pp 355-411.

61. Koch, C. T.; Sigle, W.; Höschen, R.; Rühle, M.; Essers, E.; Benner, G.; Matijevic, M. SESAM: Exploring the Frontiers of Electron Microscopy. *Microscopy and Microanalysis* 2006, 12.

62. Koch, C. T. FRWRtools plugin. http://www.christophtkoch.com/FRWR/index_tools.html.

63. Collaboration, A.; editors of the volumes, I. E. F. C. Bismuth selenide (Bi2Se3) optical properties, dielectric constants. In *Non-Tetrahedrally Bonded Elements and Binary Compounds I*, Madelung, O.; Rössler, U.; Schulz, M., Eds. Springer-Verlag: Berlin/Heidelberg, Vol. 41C, pp 1-12.

64. Gureyev, T. E. Composite techniques for phase retrieval in the Fresnel region. *Optics Communications* 2003, 220, 49-58.

65. Oszlanyi, G.; Suto, A. Ab initio structure solution by charge flipping. *Acta Crystallographica Section A* 2004, 60, 134-141.

66. Ophus, C.; Ewalds, T. Guidelines for quantitative reconstruction of complex exit waves in HRTEM. *Ultramicroscopy* 2012, 113, 88-95.

67. Lichte, H.; Geiger, D.; Linck, M. *Off-axis electron holography in an aberration-corrected transmission electron microscope*. 2009; Vol. 367, p 3773-3793.

68. Gatel, C.; Lubk, A.; Pozzi, G.; Snoeck, E.; Hÿtch, M. Counting Elementary Charges on Nanoparticles by Electron Holography. *Physical Review Letters* 2013, 111, 025501.

69. Bonevich, J. HolograFREE software. http://www.nist.gov/mml/msed/functional_nanostructure/electron_holography.cfm.

70. *Nobel Lectures in Physics 1971-1980*. World Scientific Pub Co Inc: 1991; p 603.

71. Orchowski, A.; Rau, W. D.; Lichte, H. Electron Holography Surmounts Resolution Limit of Electron Microscopy. *Physical Review Letters* 1995, 74, 399-402.

72. Loudon, J. C.; Mathur, N. D.; Midgley, P. A. Charge-ordered ferromagnetic phase in La0.5Ca0.5MnO3. *Nature* 2002, 420, 797-800.

73. Simon, P.; Lichte, H.; Formanek, P.; Lehmann, M.; Huhle, R.; Carrillo-Cabrera, W.; Harscher, A.; Ehrlich, H. Electron holography of biological samples. *Micron* 2008, 39, 229-256.

74. Lehmann, M.; Lichte, H. Tutorial on off-axis electron holography. *Microscopy and microanalysis: the official journal of Microscopy Society of America, Microbeam Analysis Society, Microscopical Society of Canada* 2002, 8, 447-466.

75. Möllenstedt, G.; Wahl, H. Elektronenholographie und Rekonstruktion mit Laserlicht. *Die Naturwissenschaften* 1968, 55, 340-341.

76. Haine, M. E.; Dyson, J. A Modification to Gabor's Proposed Diffraction Microscope. *Nature* 1950, 166, 315-316.

77. Kirkland, E. J. Improved high resolution image processing of bright field electron micrographs: I. Theory. *Ultramicroscopy* 1984, 15, 151-172.

78. Kirkland, A. I.; Saxton, W. O.; Chau, K. L.; Tsuno, K.; Kawasaki, M. Super-resolution by aperture synthesis: tilt series reconstruction in CTEM. *Ultramicroscopy* 1995, 57, 355-374.

79. Haigh, S. J.; Sawada, H.; Kirkland, A. I. Optimal tilt magnitude determination for aberration-corrected super resolution exit wave function reconstruction. *Philosophical Transactions of the Royal Society A: Mathematical, Physical and Engineering Sciences* 2009, 367, 3755-3771.

80. Haigh, S. J.; Jiang, B.; Alloyeau, D.; Kisielowski, C.; Kirkland, A. I. Recording low and high spatial frequencies in exit wave reconstructions. *Ultramicroscopy* 2013, 133, 26-34.

81. Dunin-Borkowski, R. E. The development of Fresnel contrast analysis, and the interpretation of mean inner potential profiles at interfaces. *Ultramicroscopy* 2000, 83, 193-216.

82. Twitchett, A. C.; Dunin-Borkowski, R. E.; Midgley, P. A. Comparison of off-axis and in-line electron holography as quantitative dopant-profiling techniques. *Philosophical Magazine* 2006, 86, 5805-5823.

83. Ozsoy-Keskinbora, C.; Boothroyd, C. B.; Dunin-Borkowski, R. E.; van Aken, P. A.; Koch, C. T. Hybridization approach to in-line and off-axis (electron) holography for superior resolution and phase sensitivity. *Sci. Rep.* 2014, 4.

84. Koch, C. T. Determination of grain boundary potentials in ceramics: Combining impedance spectroscopy and inline electron holography. *International Journal of Materials Research (formerly Zeitschrift fuer Metallkunde)* 2010, 101, 43-49.

85. Geilhufe, J.; Pfau, B.; Schneider, M.; Büttner, F.; Günther, C. M.; Werner, S.; Schaffert, S.; Guehrs, E.; Frömmel, S.; Kläui, M.; Eisebitt, S. Monolithic focused reference beam X-ray holography. *Nature Communications* 2014, 5.

86. Ruhlandt, A.; Krenkel, M.; Bartels, M.; Salditt, T. Three-dimensional phase retrieval in propagation-based phase-contrast imaging. *Physical Review A* 2014, 89.

87. Rosenhahn, A.; Barth, R.; Staier, F.; Simpson, T.; Mittler, S.; Eisebitt, S.; Grunze, M. Digital in-line soft x-ray holography with element contrast. *Journal of the Optical Society of America. A, Optics, image science, and vision* 2008, 25, 416-422.

88. Wachulak, P. W.; Bartels, R. A.; Marconi, M. C.; Menoni, C. S.; Rocca, J. J. In *Table Top Extreme Ultraviolet Holography*, Conference on Lasers and Electro-Optics/Quantum Electronics and Laser Science Conference and Photonic Applications Systems Technologies, 2007/05/06/; Optical Society of America: 2007.

89. Baars, J. W. M.; Lucas, R.; Mangum, J. G.; Lopez-Perez, J. A. Near-Field Radio Holography of Large Reflector Antennas. *arXiv:0710.4244 [astro-ph]* 2007.

90. Khare, K.; Ali, P. T. S.; Joseph, J. Single shot high resolution digital holography. *Optics Express* 2013, 21, 2581-2591.

91. Kemper, B.; Langehanenberg, P.; von Bally, G. Digital Holographic Microscopy. *Optik & Photonik* 2007, 2, 41-44.

92. Mitchell, D. *Mean Free Path Estimator*.

93. Joy, D. C. SMART – a program to measure SEM resolution and imaging performance. *Journal of Microscopy* 2002, 208, 24-34.

94. Yi, J.; Chu, Y. S.; Chen, Y.-T.; Chen, T.-Y.; Hwu, Y.; Margaritondo, G. High-resolution hard-x-ray microscopy using second-order zone-plate diffraction. *Journal of Physics D: Applied Physics* 2011, 44.

95. Schowalter, M.; Titantah, J. T.; Lamoen, D.; Kruse, P. Ab initio computation of the mean inner Coulomb potential of amorphous carbon structures. *Applied Physics Letters* 2005, 86.

96. McCartney, M. R.; Gajdardziska-Josifovska, M. Absolute measurement of normalized thickness, t/λi, from off-axis electron holography. *Ultramicroscopy* 1994, 53, 283-289.

97. Gajdardziska-Josifovska, M.; McCartney, M. R. Elimination of thickness dependence from medium resolution electron holograms. *Ultramicroscopy* 1994, 53, 291-296.

98. Museum, T. B. The Lycurgus Cup. http://www.britishmuseum.org/explore/highlights/highlight_objects/pe_mla/t/the_lycurgus_cup.aspx.

99. Freestone, I.; Meeks, N.; Sax, M.; Higgitt, C. The Lycurgus Cup — A Roman nanotechnology. *Gold Bulletin* 2007, 40, 270-277.

100. Daniel, M.-C.; Astruc, D. Gold Nanoparticles: Assembly, Supramolecular Chemistry, Quantum-Size-Related Properties, and Applications toward Biology, Catalysis, and Nanotechnology. *Chemical Reviews* 2003, 104, 293-346.

101. Saxena, U.; Goswami, P. Electrical and optical properties of gold nanoparticles: applications in gold nanoparticles-cholesterol oxidase integrated systems for cholesterol sensing. *Journal of Nanoparticle Research* 2012, 14, 1-11.

102. Jennings, T.; Strouse, G. Past, Present, and Future of Gold Nanoparticles. In *Bio-Applications of Nanoparticles*, Chan, W. W., Ed. Springer New York: 2007; Vol. 620, pp 34-47.

103. Hvolbæk, B.; Janssens, T. V. W.; Clausen, B. S.; Falsig, H.; Christensen, C. H.; Nørskov, J. K. Catalytic activity of Au nanoparticles. *Nano Today* 2007, 2, 14-18.

104. Ichikawa, S.; Okazaki, K.; Akita, T.; Okumura, M.; Tanaka, K.; Kohyama, M. Atomic and Electronic Structures of Nano-Interface In Au/TiO2 Catalyst - Electron Microscopic Approach. *MRS Online Proceedings Library* 2002, 738, null-null.

105. Yamamoto, M.; Terui, T.; Ueda, R.; Imazu, K.; Tamada, K.; Sakano, T.; Matsuda, K.; Ishii, H.; Noguchi, Y. Photoinduced conductance switching in a dye-doped gold nanoparticle transistor. *Applied Physics Letters* 2012, 101, -.

106. Cai, W.; Gao, T.; Hong, H.; Sun, J. Applications of gold nanoparticles in cancer nanotechnology. *Nanotechnology, Science and Applications* 2008, 2008, 17-32.

107. Conde, J.; Tian, F.; Hernández, Y.; Bao, C.; Cui, D.; Janssen, K.-P.; Ibarra, M. R.; Baptista, P. V.; Stoeger, T.; de la Fuente, J. M. In vivo tumor targeting via nanoparticle-mediated therapeutic siRNA coupled to inflammatory response in lung cancer mouse models. *Biomaterials* 2013, 34, 7744-7753.

108. Guo, S.; Dong, S. Biomolecule-nanoparticle hybrids for electrochemical biosensors. *TrAC Trends in Analytical Chemistry* 2009, 28, 96-109.

109. Cowley, J. M. High Resolution Electron Microscopy. *Annual Review of Physical Chemistry* 1987, 38, 57-88.

110. Liu, J. High-Resolution Scanning Electron Microscopy. In *Handbook of Microscopy for Nanotechnology*, Yao, N.; Wang, Z., Eds. Springer US: 2005; pp 325-359.

111. Kirkland, A. I.; Meyer, R.; uuml; R., d. “Indirect” High-Resolution Transmission Electron Microscopy: Aberration Measurement and Wavefunction Reconstruction. *Microscopy and Microanalysis* 2004, 10, 401-413.

112. Koch, C. T. Using dynamically scattered electrons for three-dimensional potential reconstruction. *Acta Crystallographica Section A* 2009, 65, 364-370.

113. Van den Broek, W.; Koch, C. T. Method for Retrieval of the Three-Dimensional Object Potential by Inversion of Dynamical Electron Scattering. *Physical Review Letters* 2012, 109, 245502.

114. Van Dyck, D.; Chen, F.-R. /`Big Bang/' tomography as a new route to atomic-resolution electron tomography. *Nature* 2012, 486, 243-246.

115. Allen, L. J.; McBride, W.; O'Leary, N. L.; Oxley, M. P. Exit wave reconstruction at atomic resolution. *Ultramicroscopy* 2004, 100, 91-104.

116. Ozsoy-Keskinbora, C.; Boothroyd, C. B.; Dunin-Borkowski, R. E.; van Aken, P. A.; Koch, C. T. Mapping the electrostatic potential of Au nanoparticles using hybrid electron holography. *Ultramicroscopy* 2016, 165, 8-14.

117. Popescu, R.; Müller, E.; Wanner, M.; Gerthsen, D.; Schowalter, M.; Rosenauer, A.; Böttcher, A.; Löffler, D.; Weis, P. Increase of the mean inner Coulomb potential in Au clusters induced by surface tension and its implication for electron scattering. *Physical Review B* 2007, 76, 235411.

118. Goswami, A.; Lisgarten, N. D. The measurement of inner potentials for copper, silver and gold. *Journal of Physics C: Solid State Physics* 1982, 15, 4217.

119. Ichikawa, S.; Akita, T.; Okumura, M.; Haruta, M.; Tanaka, K.; Kohyama, M. Electron holographic 3-D nano-analysis of Au/TiO2 catalyst at interface. *Journal of Electron Microscopy* 2003, 52, 21-26.

120. Schowalter, M.; Rosenauer, A.; Lamoen, D.; Kruse, P.; Gerthsen, D. Ab initio computation of the mean inner Coulomb potential of wurtzite-type semiconductors and gold. *Applied Physics Letters* 2006, 88, 232108.

121. Sanchez, A.; Ochando, M. A. Calculation of the mean inner potential. *Journal of Physics C: Solid State Physics* 1985, 18, 33.

122. Koch, C. T. Quantitative TEM/STEM Simulations (QSTEM). http://qstem.org/.

123. Lubk, A.; Wolf, D.; Lichte, H. The effect of dynamical scattering in off-axis holographic mean inner potential and inelastic mean free path measurements. *Ultramicroscopy* 2010, 110, 438-446.

124. Boothroyd, C. B.; Dunin-Borkowski, R. E. The contribution of phonon scattering to high-resolution images measured by off-axis electron holography. *Ultramicroscopy* 2004, 98, 115-133.

125. Linck, M.; Freitag, B.; Kujawa, S.; Lehmann, M.; Niermann, T. State of the art in atomic resolution off-axis electron holography. *Ultramicroscopy* 2012, 116, 13-23.

126. Haider, M.; Rose, H.; Uhlemann, S.; Schwan, E.; Kabius, B.; Urban, K. A spherical-aberration-corrected 200 kV transmission electron microscope. *Ultramicroscopy* 1998, 75, 53-60.

127. Haider, M.; Uhlemann, S.; Zach, J. Upper limits for the residual aberrations of a high-resolution aberration-corrected STEM. *Ultramicroscopy* 2000, 81, 163-175.

Curriculum Vitae

Personal

Name: Cigdem Ozsoy Keskinbora

Address: Baerenseestr 27, 70569 Stuttgart, Germany

Email: c.ozsoy@fkf.mpg.de – ozsoycigdem@gmail.com

Nationality: Turkish Date of Birth: 26.07.1984 Gender: Female

Education

2002 – 2007	B. Sc. in Materials Science and Engineering Anadolu University, Eskisehir, Turkey "Magnetic Tunnel Juctions in Spin Valve Systems"
2007 – 2010	M. Sc. in Nanotechnology Anadolu University, Eskisehir, Turkey "Transmission Electron Microscopy Investigation of Lead Free KNN Ceramics"
2011 – 2015	Ph.D. at Max-Planck-Institute for Solid State Research and TU Darmstadt "Recovering Low Spatial Frequency Phase Information by Electron Holography: Challenges, Solutions and Application to Materials Science"

Publications and Conference Proceedings:

- Ozsoy-Keskinbora, C.; Boothroyd, C. B.; Dunin-Borkowski, R. E.; van Aken, P. A.; Koch, C. T., Hybridization approach to in-line and off-axis (electron) holography for superior resolution and phase sensitivity. *Sci. Rep.* 2014, **4**, 07020.

- Ozsoy-Keskinbora, C.; Boothroyd, C. B.; Dunin-Borkowski, R. E.; van Aken, P. A.; Koch, C. T., Mapping the Electrostatic Potential of Au Nanoparticles via Hybrid Electron Holography. *Ultramicroscopy*, 2016, **165**,8-14.

- Ozsoy-Keskinbora, C.; Van den Broek, W.; Parvizi, A.;Boothroyd, C. B.; Dunin-Borkowski, R. E.; van Aken, P. A.; Koch, C. T., Full-resolution high-contrast imaging of phase objects by gradient-flipping-assisted focal series reconstruction. *In preparation.*

- Talebi, N.; Ozsoy-Keskinbora, C.; Benia,H.M.; Koch, C. T.; van Aken,P. A.; Wadge Dyakonov Waves and Dyakonov Plasmons in Topological Insulator Bi_2Se_3 Probed by Electron Beams. *ACS Nano*, 2016, **10 (7)**, 6988-6994.

- Ozsoy-Keskinbora, C.; Boothroyd, C. B.; Dunin-Borkowski, R. E.; van Aken, P. A.; Koch, C. T., Hybridization of Off-Axis and In-line High-Resolution Electron Holography. Microscopy and Microanalysis,2014, 20 (S3), 272-273

- Ozsoy-Keskinbora, C.; Boothroyd, C. B.; Dunin-Borkowski, R. E.; van Aken, P. A.; Koch, C. T., Hybrid Electron Holography, Microscopy and Microanalysis, 2015, 21 (S3), 2311-2312

- Ozsoy-Keskinbora, C.; Talebi, N.; Benia, M. H.; Koch, C. T.; van Aken, P. A., Unconventional Surface Plasmon Excitations in Bi_2Se_3. Microscopy and Microanalysis, 2015, 21 (S3), 2057-2058

- Talebi, N.; Ozsoy-Keskinbora, C.; van Aken, P.A.; Optical Modes in Topological Insulator Bi_2Se_3 Probed by Relativistic Electrons, European Quantum Electronic Conference, 2015, EH_2_2

Professional, Research Experience and Awards

M&M 2014 best poster award

MPI- Intelligent Systems, Grassroots

Collaboration with Ernst Ruska-Centre under project number ER-C B-013.

Project engineer at Ceramic Processing Group, Dept. of Mat. Sci. & Eng., Anadolu University, Turkey, from 9/2007 till 12/2010

Instructor – Characterization Lab., 2008-10 Dep. of Mat. Sci. & Eng., Anadolu University,

Erasmus/Socrates Scholarship - Fachbereich Materialwissenschaften – TU Darmstadt

Scientific activities

Poster/Oral Presentations:

Microscopy and Microanalysis Meeting, Portland, USA, 2015.

PICO 2013, Kasteel Vaalsbroek, The Netherland, 2015

Microscopy and Microanalysis Meeting, Hartford, USA, 2014.

ESTEEM2 Electron Crystallography Workshop, Cambridge, UK, 2014.

PICO 2013, Kasteel Vaalsbroek, The Netherland, 2013.

Microscopy Conference, Regensburg, Germany, 2013.

Quantitative Electron Microscopy (QEM), Saint Aygulf, France 2013.

Microscopy and Microanalysis Meeting, Portland, USA, 2010.

EMAG 2009, Sheffield, England, 2009.

Scientific Interests & Skills:

Electron Holography, Large Angle Rocking Beam Diffraction, Energy Filtering Transmission Electron Microscoy, Electron Energy Loss Spectroscopy.

Transmission Electron Microscopes (JEOL 2100F – SESAM – JEOL 4000FX – Zeiss 912, FEI-Titan, JEOL- ARM200F)

Scanning Electron Microscopes (Zeiss SUPRA 50 VP, Zeiss EVO 50 EP)

Atomic Force Microscope (Veeco, Multimode Nanoscope IV)

Erklärung zur Dissertation

Hiermit versichere ich, die vorliegende Dissertation ohne Hilfe Dritter nur mit den angegebenen Quellen und Hilfsmitteln angefertigt zu haben. Alle Stellen, die aus Quellen entnommen wurden, sind als solche kenntlich gemacht. Diese Arbeit hat in gleicher oder ähnlicher Form noch keiner Prüfungsbehörde vorgelegen.

Darmstadt, im November 2015

_____

(Cigdem OZSOY KESKINBORA)